ZnO nanowires: surface functionalization with colloidal CdSe quantum dots and excitation-intensity-dependent photoluminescence properties

Vom Fachbereich für Physik und Elektrotechnik
der Universität Bremen

zur Erlangung des akademischen Grades eines

Doktor der Naturwissenschaften
– Dr. rer. nat. –

genehmigte Dissertation

von

Dongchao Hou
aus Heze, China

1. Gutachter:	PD Dr. Tobias Voss, Universtät Bremen
2. Gutachter:	Prof. Dr. Andreas Rosenauer, Universtät Bremen
Eingereicht am:	03.09.2012
Tag des Promotionskolloquiums:	29.10.2012

Abstract

Contemporary nanotechnology has great interest in the assembly and study of hybrid structures composed of different materials that can offer enhanced properties or achieve new functions through the interaction between different constituents. ZnO nanowires, with the wide direct band gap and large exciton binding energy of the material, have attracted intense research interests for their potential optoelectronic applications in the near ultraviolet spectral region. They have also been studied for use in energy conversion and storage. They are promising candidates as photoanodes in nanostructured photovoltaic devices. Their high electron mobility favors a quick collection of the photogenerated charge carriers. Semiconductor quantum dots represent another research focus due to their striking size-tunable band gap, which provides a convenient approach to tune the spectral region of absorption and emission of the materials.

In this work, a hybrid nanostructure is built by surface functionalization of ZnO nanowire arrays with colloidal CdSe quantum dots (QDs), which has potential applications in photovoltaics and sensing applications. The QDs are synthesized by a wet-chemical method and stabilized with bifunctional 3-mercaptopropionic acid (MPA) molecules. The growth kinetics and optical properties of the QDs are studied. The average QD size can be tuned in the range of 1.4–2.5 nm by adjusting the growth time. The photoluminescence of the dry QD powder is found to be very sensitive to the ambient environment, which is attributed to oxygen-related surface effects. Adsorption of oxygen molecules can passivate the surface defects of the QDs which otherwise act as trap centers during photo-excitation and induce nonradiative and fast Auger recombination processes in the QDs.

The attachment of the CdSe QDs on the ZnO nanowire surface is achieved by using the stabilizers of the QDs as molecular linkers, which further favors the charge transfer between these two systems. The photoconductivity of the nanowire/quantum-dot hybrid structure is studied under selective photoexcitation of the QDs. An enhancement of of the photoconductivity up to 10 times is observed in air. The dynamics is further found to strongly depend on the gas environment. Desorption of surface oxygen from the ZnO nanowires, activated by charge tunnelling between the nanowires and the QDs, is found to be the dominating process for the photoconductivity enhancement. The gas environment influences the charge relaxation in the QDs through oxygen-related surface passivation, which impacts the charge tunnelling between the nanowires and the QDs and, hence, the photoconductivity dynamics.

Defects in ZnO materials can significantly influence their physical properties such as the electrical conductivity and luminescence spectra. Photoluminescence spectroscopy is a convenient, non-destructive technique for studying the crystal quality and defect states of semiconductors. ZnO generally shows an ultraviolet emission band due to the near-band-edge recombination processes and several defect-related emission bands in the visible spectral region. The dependence of the photoluminescence properties on the excitation intensity of ZnO nanowires and bulk wafers is studied. It is found that the relative strength of the band-edge emission and the defect-related emission dramatically varies with the excitation intensity. The increase of these two emission bands with excitation intensity further exhibits sample-specific behaviors, which depends on the defect species and concentrations and the microscopic origins of the defect-related emission processes. Low-temperature measurements further reveal that biexcitons or even an electron-hole plasma (EHP) may be formed in ZnO nanowires for excitation intensities $> 10^3$ W/cm^2, which causes the broadening of the donor-bound exciton emission peak and the superlinear increase of the band-edge emission with excitation intensity.

Contents

Chapter 1

Introduction

Semiconductor nanomaterials have attracted wide interest from fundamental research to technical applications. They are interesting building blocks for functional devices to achieve miniaturization and high sensitivity. They can further exhibit novel physical properties due to the enhanced interactions between charge carriers and the strong confinement effect on their motion. Modern nanotechnology has great interest in the assembly and study of hybrid structures. Through the interactions between different constituents, they can achieve enhanced properties or new functions [1–3]. Benefitting from the size effect and the small volume, nanostructured devices can obtain improved performance compared to their conventional bulk counterparts [1, 4, 5].

Semiconductor nanowires are among the most investigated nanomaterials. Their quasi-one-dimensional structures make them ideal as transport channels for charge carriers, electromagnetic fields, acoustic waves, and thermal energy, which are crucial building blocks in nanodevices for linking and communicating between different functional components [6–8]. Due to their lager surface-to-volume ratio, the electrical and optical properties can be strongly modified by surface effects. Thus, semiconductor nanowires have been explored intensely as ultrasensitive gas sensing devices [9]. They have also been studied for applications such as short-wavelength nanolasers [10], field-effect transistors [11], and nanoresonators [12].

Zinc oxide (ZnO) is a II-VI compound semiconductor with a wide direct band gap of ~ 3.37 eV at room temperature, making it an attractive material for optoelectronic applications working in the ultraviolet (UV) spectral region. One important consequence of its wide gap is the transparency of ZnO to visible light, which promotes its applications as transparent conducting electrodes in light emitting and photovoltaic devices. ZnO exhibits high resistance to radiation, which makes it a suitable material for space applications. In addition to its wide direct gap, the attraction of ZnO can be mainly attributed to its large exciton binding energy of ~ 60 meV, which implies that excitons can be stable at room temperature or even higher temperatures. This might pave the way for efficient room-temperature exciton-based lasing with low threshold current.

The research of ZnO goes back to many decades ago. The renewed interest from the mid 1990s is fuelled by the availability of high-quality nanostructures and potential new p-type doping techniques. ZnO nanowires can now be synthesized in large quantities through both gas phase and solution phase methods. A variety of growth techniques such as metal-organic chemical vapor deposition (MOCVD), molecular beam epitaxy (MBE), pulsed laser deposition

(PLD), and the widely used vapor transport methods have been developed. ZnO nanowires can also be grown from low-temperature solution based techniques. The nanowires are prepared with smooth surfaces and well-defined end facets. About ten years ago, nanolasers based on vapor transport grown ZnO nanowires were demonstrated [10]. The well-faceted side and end faces of the nanowires form a natural resonance cavity for lasing. Due to its non-centrosymmetric hexagonal crystal structure, ZnO possesses a highly piezoelectric nature. Based on this property, ZnO nano-piezogenerators have been fabricated by depositing ZnO nanowire arrays on flexible substrates [13]. A shape change in the substrate can induce the deformation of the nanowires, which acts as the driving force for electrical energy generation.

ZnO nanowires have also been explored for applications in energy conversion and storage. They were tested as photoanode in nanostructured photovoltaic devices to support photosensitizers like dye molecules. Compared to the bulk counterparts, nanostructured solar cells can provide a larger effective surface area for adsorbing sensitizers. In addition, ZnO nanowire arrays can provide direct electrical pathways to achieve quick collection of the photogenerated charge carriers due to their high electron mobility of $\sim 200\ \mathrm{cm^2V^{-1}s^{-1}}$ [14, 15].

Due to the quantum size effect in nanomaterials, their fundamental properties can be significantly modified. One representative example are the semiconductor quantum dots (QDs). They represent so-called zero dimensional semiconductor nanocrystals with sizes less than $\sim$ 10 nm, in which the motion of charge carriers is confined in all three dimensions. The most striking property of QDs is their size-tunable band gap. As the QD size decreases, the energy gap significantly broadens. One direct consequence of this effect is the blueshift of the emission wavelength.

Semiconductor QDs have been prepared by a variety of physical and chemical methods. Some examples of the physical techniques include the top-down (e.g. lithography [16]) and bottom-up (e.g. epitaxially self-assembly [17] methods. Another kind of QDs, synthesized from solution phase by wet-chemical methods, referred to as colloidal semiconductor QDs, have inspired wide research interest in the last two decades. Such QDs are capped with a layer of organic molecules, called ligands which provide electronic and chemical passivation of the QD surface. They are free-standing in solutions with the solubility defined by their ligands. This allows convenient conjugation of the QDs with other nanomaterials to build hybrid functional devices.

Colloidal semiconductor QDs now can be synthesized with high crystalline quality and good control of the particle size and size distribution. The size-tunable band gap makes them interesting for applications like light emitting devices and photosensitizers in solar cells. For the most investigated CdSe QDs, when the particle size decreases to 1 nm, the band gap energy will increase from the bulk value of 1.74 eV to $\sim$ 3.5 eV. Together with QDs made of other semiconductor materials, the optoelectronic applications can cover the full visible spectral region. Full-color QD-based displays have been realized recently using differently sized semiconductor QDs working as luminescence media for the red, green, and blue emitting pixels [18].

Semiconductor QDs have also been studied as photosensitizers in solar cells. It is convenient to tune their absorption to cover the solar spectrum by changing the QD size. In addition, QDs possess high extinction coefficients and the potential to generate multiple electron-hole pairs by single photon absorption, which is of great interest to further improvement of the light-to-energy conversion efficiencies.

However, there are till many open questions present in the research and technical applications of ZnO nanowires and semiconductor QDs. The photoluminescence properties of ZnO, especially its defect luminescence, is not completely understood yet. The assignments of the defect-related emission bands still have wide controversy [19]. In addition, many research works have been carried out on the photovoltaic devices based on semiconductor-QD-functionalized ZnO nanowires to combine the merits of these two material systems [15,20,21]. Despite possessing the above-mentioned advantages, the energy conversion efficiencies of such devices are still much lower than that of the conventional silicon-based solar cells. Some practical problems, such as the low coverage of the nanowires with QDs as well as the limited understanding of the charge-transfer mechanisms between the constituents, still hinder the breakthrough in the performance [2, 15, 22].

In this dissertation, the fundamental properties of ZnO and semiconductor QDs are first presented in chapter 2. The crystal and energy band structures of ZnO and its elementary optical excitations are introduced. The size-dependent energy level structure and the wet chemical synthesis of colloidal semiconductor QDs are described. In chapter 3, an overview of the state of research on the optical properties of ZnO, the synthesis and applications of semiconductor QDs, and the nanowire/quantum-dot hybrid structures are presented. Chapter 4 describes the preparation of the ZnO nanowire samples, the experimental techniques and setups used in this work. In chapter 5, the synthesis of CdSe QDs by a wet-chemical method is presented. The photoluminescence quenching of the QDs in oxygen-deficient environments is investigated and the chemical stability of the QDs is examined. Hybrid structures built from surface functionalization of ZnO nanowires with CdSe QDs is presented in chapter 6. The electron transfer mechanism in the hybrid structure is studied through photoconductivity measurements, and the influence of gas environment is investigated. In chapter 7, the excitation intensity dependence of the photoluminescence properties of ZnO nanowires and bulk wafers is investigated. A theoretical model is proposed and discussed for simulation of the recombination processes in ZnO. The generation of biexcitons at high excitation intensity is analyzed. Finally, a summary of the results obtained in this work and an outlook are presented in chapter 8.

Chapter 2

Fundamentals of Zinc Oxide and Semiconductor Quantum Dots

In this chapter, an overview of the fundamental properties of zinc oxide (ZnO) and colloidal semiconductor quantum dots is presented as a background for the discussion of the experimental results in the later chapters. The first section describes the crystal structure and the energy band structure of ZnO as well as its fundamental optical properties. The second section gives a short introduction of the energy band structures for low-dimensional semiconductor materials. After that, colloidal semiconductor quantum dots and their size-tunable band gaps are introduced. The next large section presents the fundamental properties of colloidal cadmium selenide (CdSe) quantum dots, including the crystal and the energy level structures, and the fundamental optical properties. The last section describes the wet-chemical synthesis methods of colloidal semiconductor quantum dots.

2.1 Properties of zinc oxide

2.1.1 Crystal structure

Zinc oxide (ZnO) is a group II-VI compound semiconductor which almost exclusively crystallizes in the hexagonal wurtzite structure [23]. The cubic zinc-blende structure of ZnO can be obtained only in epitaxial growth ZnO films on zinc-blende type substrates [24], while the rocksalt structure is stable only under pressure (> 9 GPa) [25].

The ZnO wurtzite structure is schematically shown in Fig. 2.1 and has a hexagonal unit cell with two lattice constants a = 0.325 nm and c = 0.520 nm [26]. It belongs to the space group C_{6v}^4 in the Schoenflies notation and $P6_{3mc}$ in the Hermann-Mauguin notation. The structure is composed of two inter-penetrating hexagonal close packed (hcp) sublattices, each of which consists of one type of atoms displaced with respect to the other along the c-axis by 0.195 nm. One zinc atom is surrounded tetrahedrally by four oxygen atoms, and vice versa. This tetrahedrally coordinated structure is characteristic for crystals with sp^3 hybridized chemical bondings. The bonding in ZnO is largely ionic with the bond radii of 0.074 nm for Zn^{2+} and 0.140 nm for O^{2-} [26]. This property accounts for the preferential formation of wurtzite rather than zinc-blende structure, as well as the strong piezoelectricity of ZnO.

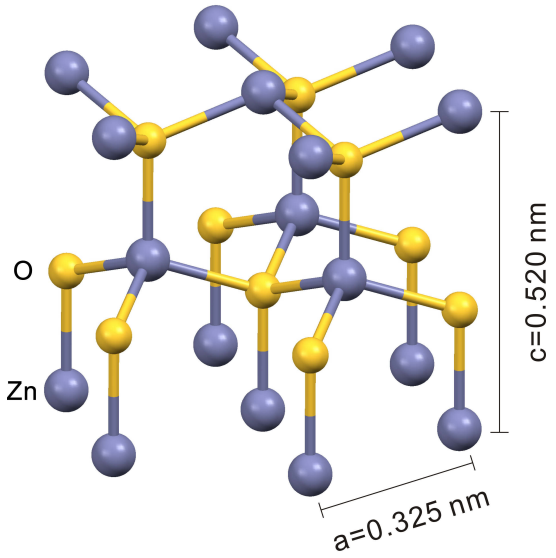

Figure 2.1: Schematic of the hexagonal wurtzite crystal structure of ZnO. a and c are the corresponding lattice constants.

2.1.2 Energy band structure

ZnO is a direct-gap semiconductor with the global extrema of the uppermost valence band (VB) and the lowest conduction band (CB) at the center of the Brillouin zone, namely the Γ-point where the wave vector $\boldsymbol{k} = 0$. Figure 2.2 shows a schematic representation of the energy band structure near the Γ-point. The lowest energy level in the conduction band is formed from the empty 4s states of Zn^{2+} or the antibonding sp^3 hybrid states. It has a symmetry $\Gamma_1 \otimes \Gamma_7 = \Gamma_7$ with inclusion of electron spin. The effective electron mass is almost isotropic, with a value around $m_e = 0.28 m_o$ [27].

The uppermost energy level in the valence band is formed by the occupied 2p orbital of O^{2-} or by the bonding sp^3 orbitals. It is split under the influence of the hexagonal crystal field and the spin-orbit interaction into three two-fold degenerate sub-bands with symmetries of Γ_7, Γ_9 and Γ_7 (Fig. 2.2). In all wurtzite-type semiconductors, these sub-bands are labeled from highest to lowest energies as A-, B-, and C-band. There was a long standing debate about the symmetry ordering of the valence bands in ZnO. Based on studies of the polarization dependence of reflectivity spectra, the A-Γ_7, B-Γ_9 and C-Γ_7 ordering was proposed by Thomas and Hopfield in 1960 [28, 29]. The A-Γ_9, B-Γ_7 and C-Γ_7 ordering is also supported by many works [30, 31]. In the present work, the most commonly accepted A-Γ_7, B-Γ_9 and C-Γ_7 ordering is used [32, 33]. The effective hole masses in ZnO are nearly isotropic, with typical values of $m_{h,A,B} = 0.59 m_o$ for the A and B bands, and $m_{h\|C} = 0.31 m_o$ and $m_{h\perp C} = 0.55 m_o$ for the C band with the wave vector direction perpendicular and parallel to the c-axis, respectively. [27].

The optical band gap E_g is defined by the energy difference between the conduction band bottom and the valence band top as depicted in Fig. 2.2. E_g is around 3.437 eV at $T = 1.6$ K, and it is reduced to 3.37 eV at room temperature [26].

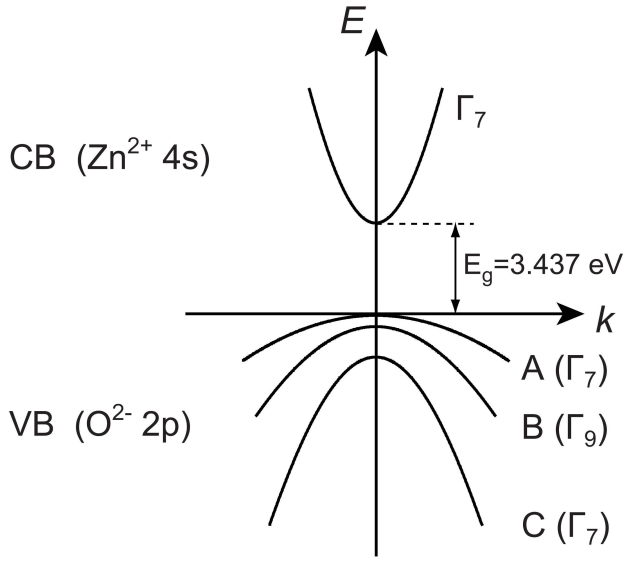

Figure 2.2: Schematic description of the band structure of ZnO near the center of the Brillouin zone. The band gap E_g corresponds to the value at $T = 1.6$ K.

2.1.3 Elementary excitations in ZnO associated with its optical properties

This subsection presents an overview of the elementary excited states in ZnO that dominate its band-edge luminescence properties. This includes the free excitons, excitons bound to donor or acceptor centers. Their transitions and coupling with lattice vibrations as well as the biexciton complexes formed at high excitation are introduced.

Free excitons and exciton polaritons

When ZnO is irradiated with light at a photon energy equal to or larger than its band gap, electrons can be excited into the conduction band while holes are generated in the valence band. Due to the Coulomb attraction between the electrons and holes, they can form electron-hole pair bound states, known as excitons. An exciton is a electrically neutral complex and has a slightly lower energy than the unbound electron and hole pair.

The Schrödinger equation of the exciton state within the effective-mass approximation can be written as [34]

$$\left(-\frac{\hbar^2}{2m_e}\nabla_e^2 - \frac{\hbar^2}{2m_h}\nabla_h^2 - \frac{e^2}{4\pi\varepsilon r_{eh}}\right)\psi_{ex} = E_{ex}\psi_{ex} \tag{2.1}$$

where r_{eh} is the electron-hole distance, ε is the dielectric constant. m_e and m_h are the electron and hole effective masses, respectively. E_{ex} is the energy eigenvalue. The equation yields a series of discrete hydrogen-like energy levels below the continuous free electron-hole pair energy states, as schematically depicted in Fig. 2.3(a).

The dispersion relation of the exciton states with the total wave vector $k = k_e + k_h$ is described as

$$E_{ex}(n,k) = E_g - \frac{1}{n^2}\frac{\mu}{m_0\varepsilon}R_y + \frac{\hbar^2k^2}{2M} \tag{2.2}$$

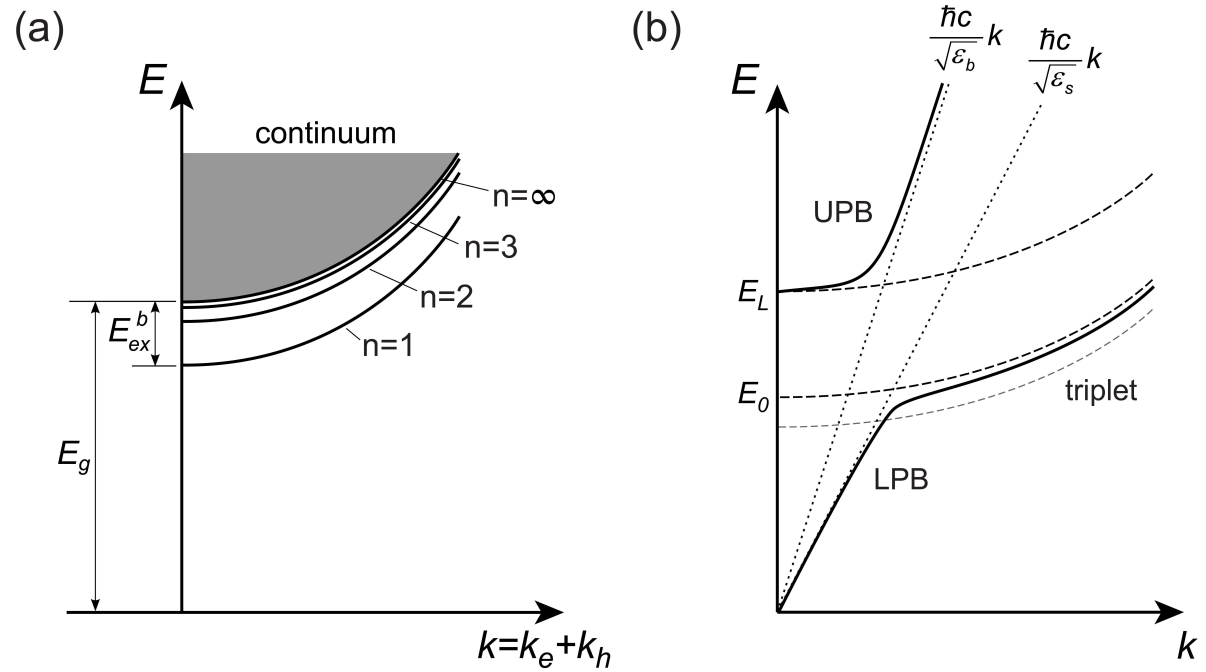

Figure 2.3: Schematic of the dispersion of (a) excitons with main quantum number n and (b) exciton polaritons resulting from the coupling of the excitons with photons in ZnO [35].

with

$n = 1, 2, 3, ...$	principal quantum number
$M = m_e + m_h$	total exciton mass
$\mu = \frac{m_e m_h}{m_e + m_h}$	reduced exciton mass
$R_y = 13.6$ eV	the Rydberg energy

E_g is the energy band gap of the material, and $\hbar$ is the reduced Planck constant.

The energy distance between the ground exciton state ($n = 1$) and the bottom of the free electron-hole pair ($n = \infty$) continuum is referred to as the exciton binding energy,

$$E_{ex}^b = \frac{\mu}{m_0 \varepsilon} R_y \tag{2.3}$$

In ZnO, there are three kinds of excitons, namely A-, B-, and C-exciton, corresponding to its three valence sub-bands. Their exciton binding energies are $E_{ex}^b \approx 60$ meV [36], which is about 2.4 times of the thermal energy at room temperature ($k_B T = 25$ meV, k_B is the Boltzmann constant). Thus excitons can stably exist in ZnO at room temperature, which is an efficient source for the band-edge luminescence of ZnO due to the tightly binding electron-hole pair states that favor efficient recombination. The recombination of an exciton gives rise to a photon emission with an energy defined by Equ. 2.2.

The spatial size of an exciton state is described by its Bohr radius,

$$a_B^{ex} = \frac{4\pi\varepsilon\hbar^2}{\mu e^2} \tag{2.4}$$

The Bohr radius is approximately 1.8 nm for the A-exciton in ZnO [27]. The value is much larger than the lattice constants of ZnO, implying that the exciton state exists over many unit cells. Such excitons are commonly called Wannier excitons [37].

Moreover, light propagates in a semiconductor in the form of electromagnetic field and can excite excitons. Those excitons can recombine and emit photons. The whole state can be deemed as a mixture of the electromagnetic field of the light and the excited excitonic polarizations. This mixed state is quantized and its energy quanta are known as exciton polaritons. For A-excitons in ZnO, both the electron and the hole states have a Γ_7 symmetry with angular momentum $l = 1/2$. Thus the total angular momentum of A-excitons is $L = 0$ (singlet state) or $L = 1$ (triplet state). Only excitons at the singlet state are dipole-allowed for optical transitions, and hence called bright excitons. They can couple with photons to form polaritons. This singlet state is split into two levels by the Coulomb interaction between electrons and holes, referred to as the longitudinal and the transverse excitons.

Figure 2.3(b) schematically shows the dispersion of the exciton polaritons in ZnO. The dispersion of the longitudinal (E_L) and the transverse (E_0) excitons are drawn as dashed lines. The dispersion of the dark triplet exciton is also plotted below the bright excitons. The two dotted straight lines are the dispersions of photons with slopes of $\hbar c/\sqrt{\varepsilon_b}$ and $\hbar c/\sqrt{\varepsilon_s}$, respectively, where c is the speed of light in vacuum. ε_b and ε_s are the background and static dielectric constants of the material for electromagnetic fields with high and low angular frequencies, respectively. The dispersion of polaritons has two branches (solid lines): the lower polariton branch (LPB) and the upper polariton branch (UPB). The LPB curve starts first with a photon-like dispersion and then bends over to an exciton-like dispersion. The UPB branch with higher energy starts along the longitudinal exciton dispersion and then transits to be photon-like. The transition regions between the photon-like and exciton-like dispersions are called “bottleneck”.

Longitudinal optical phonon replicas

An efficient luminescence channel of the exciton polaritons in semiconductors is formed through strong coupling with the lattice vibrations. The quanta of the lattice vibrations are known as phonons. Wurtzite-type ZnO has $s = 4$ atoms per unit cell in the lattice structure. Therefore, it has 3 acoustic phonon modes, and $(3s - 3) = 9$ optical modes with 3 longitudinal optical (LO) and 6 transverse optical (TO) types. The exciton polaritons can strongly couple with the LO phonons while their coupling with the TO and acoustic phonons is much weaker [26].

As schematically illustrated in Fig. 2.4, a polariton located at the exciton-like part of the LPB can be scattered into the photon-like branch by emission of one or more LO phonons. Afterwards, the photon-like polariton is converted to a photon and transmit through the semiconductor surface, yielding luminescence. Such transitions are referred to as LO-phonon replicas of exciton polaritons. The luminescence energy of the n-th LO-phonon replica is given by

$$\hbar\omega_n = E_g - E_{ex}^b - nE_{LO} \tag{2.5}$$

where E_{LO} is the LO phonon energy.

The luminescence intensity is related to the polariton-phonon coupling efficiency, which can be described by [35]

$$I_n = E_{kin}^{1/2}\, exp\left(-\frac{E_{kin}}{k_B T}\right) W_n(E_{kin}) \tag{2.6}$$

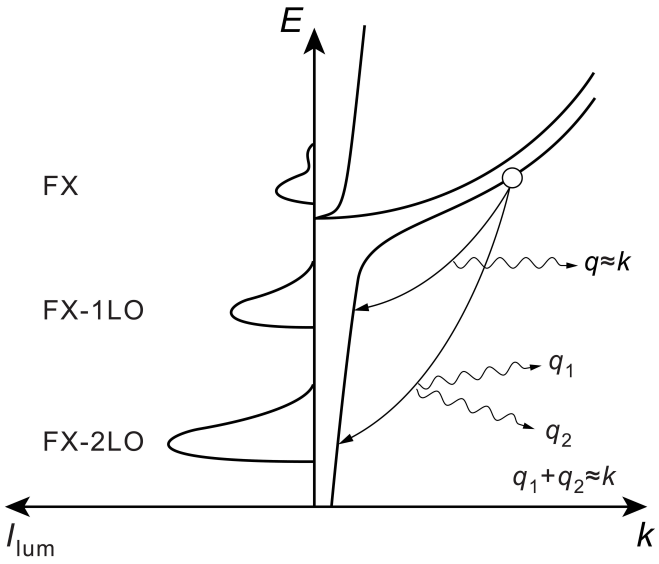

Figure 2.4: Schematic of the decay mechanisms of the exciton polaritons via longitudinal phonon (LO) replicas [35].

where $E_{kin} = (\hbar^2 k^2)/(2M)$ is the kinetic energy of exciton polariton. $W_n(E_{kin})$ is the transition probability, which depends on E_{kin} by a power law as

$$W_n(E_{kin}) \propto E_{kin}^{l_n} \tag{2.7}$$

where l_n is the scaling exponent with its first two values of $l_1 = 1$ and $l_2 = 0$.

Bound excitons and two-electron satellites

Free excitons can move around in semiconductor material and they may hit a trapping center to form a bound exciton complex. Excitons can be bound to neutral donors (D^0X) and acceptors (A^0X), as well as their ionized states (D^+X and A^-X), as schematically shown in Fig. 2.5. However, excitons bound to ionized acceptors are usually very unstable. The binding energy or localization energy of a bound exciton E^b is defined as the energy distance between the bound exciton state and the lowest free exciton state. Its magnitude for different kinds of bound exciton complexes usually obeys the following relationship

$$E^b_{D^+X} < E^b_{D^0X} < E^b_{A^0X} \tag{2.8}$$

For ZnO, they are typically in the range of 3-30 meV [38, 39]. In high quality ZnO single crystals, emission from neutral donor bound excitons (DBE) often dominates the near-band-

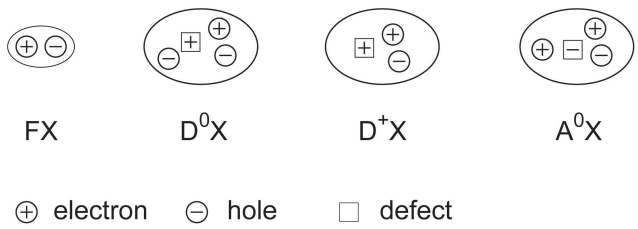

Figure 2.5: Visualization of free exciton (FX) and excitons bound to neutral donor (D^0X), ionized donor (D^+X), and neutral acceptor (A^0X).

edge photoluminescence due to the abundance of intrinsic shallow donor-type defects. These bound excitons have no translational degrees of freedom. Therefore, at low temperature their recombination can give rise to very narrow luminescence bands with spectral widths below 1 meV [27].

During the recombination of a neutral donor bound exciton, the donor could be left at its excited state ultimately. Such transition is referred to as two electron satellite (TES). The energy of the emitted photon is smaller than that of a normal DBE recombination by an amount equal to the energy difference between the ground state of the donor and its final excited state after recombination.

At low temperatures, the transitions of donor bound excitons and their LO phonon replicas as well as their TES generally dominate the band-edge luminescence of ZnO. With increasing temperature, the bound excitons gradually dissociate and tend to disappear for $T > 80$ K while the free exciton emission is significantly enhanced [27].

Biexcitons at high excitation

The above excitation states and their recombination are discussed in the linear optics regime, where the excitons and bound-exciton complexes are treated as separate particles and the interactions among them are not considered. When excitation intensity is increased, the concentrations of excitons and free charge carriers accordingly increase. Thus the effect of exciton-exciton collision and interaction becomes stronger. At low temperature, the collision processes can give rise to new excitation states like biexcitons — the bound states of two excitons. Apart from collision between two free excitons, biexcitons can also be created by direct two-photon absorption. The binding energy of a biexciton E_{xx}^{b} with respect to the energy of two free excitons is around 15 meV in ZnO [40].

In the recombination process, a biexciton normally decays into a free exciton with emission of a photon. The emission band is usually called the M band [41], which often appears in the spectral region of the A^0X and D^0X bound exciton transitions [27].

2.2 Energy band structures in low-dimensional semiconductor systems

The motion of charge carriers in semiconductors possesses wave-particle duality, as depicted in the concept of de Broglie waves. The wave property of the carriers is characterized by their de Broglie wavelength, which is given as

$$\lambda = \frac{2\pi\hbar}{\sqrt{3m^* k_B T}} \tag{2.9}$$

where $\hbar$ is the reduced plank constant, m^* is the effective mass of the carrier, k_B is the Boltzmann constant, and T is temperature in Kelvin. The value of λ is typically in the order of 10 nm for most semiconductors. In a semiconductor crystal with its size comparable to the de Broglie wavelength of the internal carriers, the quantum confinement effect occurs. In this case, the motion of the carriers and their excitations is confined by the physical dimensions of the semiconductor, leading to a profound change in the energy band structure. Such a so-

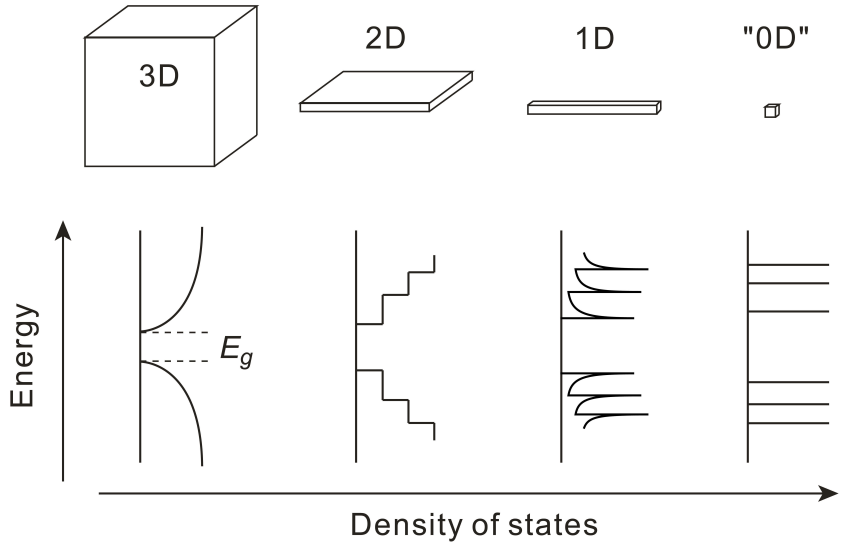

Figure 2.6: Evolution of the density of states in semiconductor materials from bulk to low-dimensional regimes.

called low-dimensional material system commonly shows novel properties compared to its bulk counterpart [42].

According to the degree of freedom in the carrier motion, the low-dimensional materials are commonly referred to as quantum well (2D), quantum wire (1D), and quantum dot (0D), as schematically shown in Fig. 2.6. The last case describes the semiconductor crystals in which the carrier motion is confined in all three dimensions. The density of states in the energy bands for these three systems are given by

$$D_{3D}(E) = \frac{(2m^*)^{3/2}}{2\pi^2\hbar^3}\sqrt{E} \tag{2.10a}$$

$$D_{2D}(E) = \frac{m^*}{\pi\hbar^2 L_z}\sum_n H[E - E_n] \tag{2.10b}$$

$$D_{1D}(E) = \frac{\sqrt{2m^*}}{\pi\hbar L_y L_z}\sum_{n,l}\frac{1}{\sqrt{E - E_{n,l}}} \tag{2.10c}$$

$$D_{0D}(E) = \frac{2}{L_x L_y L_z}\sum_{n,l,m}\delta[E - E_{n,l,m}] \tag{2.10d}$$

where E is the energy measured from the band edges. $H[x]$ is the unit step function with $H[x \geq 0] = 1$ and $H[x < 0] = 0$. $\delta(x)$ is the delta function. E_n, $E_{n,l}$ and $E_{n,l,m}$ with the quantum numbers n, l, and m denote the quantized energy levels in 2D, 1D and 0D materials, respectively. The density of states for different confinement cases are schematically shown in Fig. 2.6. For bulk materials, energy levels are quasi-continuously distributed in each energy band separated by the forbidden gaps. Reduction of the dimensions of a semiconductor induces two main aspects of changes in its band structure: the energy states gradually converge to atom-like discrete levels while the band gap broadens. These effects significantly modify the optical properties of low-dimensional materials.

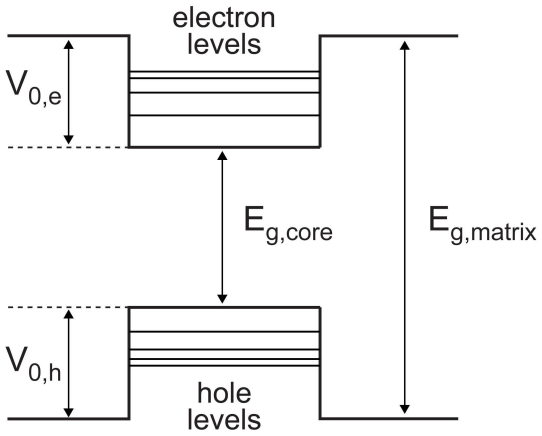

Figure 2.7: Finite depth potential well model for the theoretical treatment of the size-dependent band gap in semiconductor QDs. $E_{g,core}$ is the band gap of QDs. $E_{g,matrix}$ is the band gap of the surrounding matrix. For colloidal QDs, this corresponds to the surfactant ligands. $V_{0,e}$ and $V_{0,h}$ represent the confinement potential for photoexcited electrons and holes, respectively.

2.3 Colloidal semiconductor quantum dots and their size-dependent energy band gaps

Semiconductor nanocrystals (NCs) or quantum dots (QDs) are crystalline semiconductor particles with typical sizes ranging from 1 to 10 nm, consisting of hundreds to a few thousands of atoms. The QDs still maintain the bulk crystallinity of the material. However, as a result of the enhanced quantum confinement effects, the bulk energy band structure converges into discrete levels. The spacing between the levels can reach several hundred meV for QDs [43], which is much larger than the thermal energy at room temperature (25 meV).

Many techniques, including physically top-down (e.g. lithography [16]) and bottom-up (e.g. epitaxial self-assembly [17] and chemical [44]) approaches, have been developed for the preparation of semiconductor QDs. One of the most investigated type is the colloidal QD synthesized in liquid phase by wet chemical methods. The produced QDs are free-standing in solution and capped outside with a layer of organic molecules termed as surfactant ligands or stabilizers. These ligands are bound to the outer atoms of the QDs and saturate the dangling bonds, which ensures the chemical stability of the crystal core and in the meantime defines the solubility of the QDs in different solvents. In addition, these molecules can prevent the QDs from aggregation by the provided steric barriers or electrostatic repulsion among their outgoing head groups.

A unique property of semiconductor QDs is their size-tunable energy band gaps. The band gap of a semiconductor QD increases as the particle size decreases. In addition, the band gap also depends on the surrounding matrices of the QDs, e.g. the capping organic ligands of the colloidal QDs [45]. Many theoretical models have been developed for calculation of the size dependence of band gap in semiconductor QDs. One of the most successful models is the finite-depth square-well effective-mass approximation (FWEMA) [45, 46] for colloidal QDs. In this method, the QD is treated as a spherical potential well with finite depth in which the motion of carriers is confined.

In the FWEMA model, the stationary Schrödinger equation for the lowest excited state is

written as

$$H\psi(\mathbf{r}) = E\psi(\mathbf{r}) \tag{2.11}$$

with the Hamiltonian

$$H = -\frac{\hbar^2}{2m_e^*}\bigtriangledown_e^2 - \frac{\hbar^2}{2m_h^*}\bigtriangledown_h^2 + V_{0,e}(\mathbf{r}_e) + V_{0,h}(\mathbf{r}_h) - \frac{e^2}{\varepsilon r_{eh}} \tag{2.12}$$

where m_e^* and m_h^* are the effective masses of electrons and holes, ε is the effective dielectric constant, and $r_{eh} = |\mathbf{r}_e - \mathbf{r}_h|$ is the electron-hole distance. $V_{0,e}(\mathbf{r}_e)$ and $V_{0,h}(\mathbf{r}_h)$ are the confinement potentials for electrons and holes. They are constants ($V_{0,e}$ and $V_{0,h}$) outside the QD and zero inside the dot, as schematically shown in Fig. 2.7. These confinement potentials are related to the surfactant ligands used for the colloidal QDs. From Equ. 2.11, the variation of the band gap energy of a QD with radius a with respect to its bulk gap is given by

$$\triangle E_g = E_{g,QD} - E_{g,bulk} = \frac{\hbar^2\pi^2}{2a^2}\left[\frac{\eta_e^2}{m_e^*} + \frac{\eta_h^2}{m_h^*}\right] + E_{eh} \tag{2.13}$$

where η_e and η_h are dimensionless parameters depending on V_0, m^* and a, which can be calculated numerically. The first term is the quantum energy of localization of electron and hole due to the confinement of their motion inside the QD. It increases with a^{-2}. The second term E_{eh} is the Coulomb attraction between electrons and holes. With the potential depth $V_0 \to \infty$, Equ. 2.13 is converted to [47]

$$\triangle E_g = \frac{\hbar^2\pi^2}{2a^2}\left[\frac{1}{m_e^*} + \frac{1}{m_h^*}\right] - \frac{1.8e^2}{\varepsilon a} \tag{2.14}$$

As shown in Fig. 2.8(a), the calculated band gap by this FWEMA model shows a good agreement with the experimental data of CdSe QDs. Even though this model is based on an effective mass approximation which is only proper for the wide gap semiconductors characterized with nearly parabolic energy bands, a reasonably well agreement was also obtained in the calculations for the band gaps of narrow-gap semiconductor QDs (Fig. 2.8(b)). The band gap broadens significantly when the particle size decreases. For CdSe QDs with a particle size of $0.5a_B$ and 0.25 a_B ($a_B = 5.6nm$ is the bulk excitonic Bohr radius), the band gap increases from its bulk value of 1.74 eV to 1.95 eV and 2.3 eV, respectively.

2.4 Properties of colloidal CdSe quantum dots

Cadmium selenide (CdSe) is an important II-VI compound semiconductor. CdSe QDs are the most investigated colloidal semiconductor QDs due to their mature synthesis techniques [48]. Bulk CdSe has three crystalline forms: hexagonal wurtzite, cubic zinc-blende, and cubic rocksalt. The thermodynamically stable crystalline form is wurtzite structure, with two lattice parameters of $a = 4.3$ Å and $c = 7.01$ Å [49]. The zinc-blende structure is unstable and converts into the wurtzite type under moderate heating. Colloidal CdSe QDs can crystallize in either zinc-blende or wurtzite structures, or in some cases the coexistence of both structures, depending on the synthesis methods and conditions [44, 50, 51].

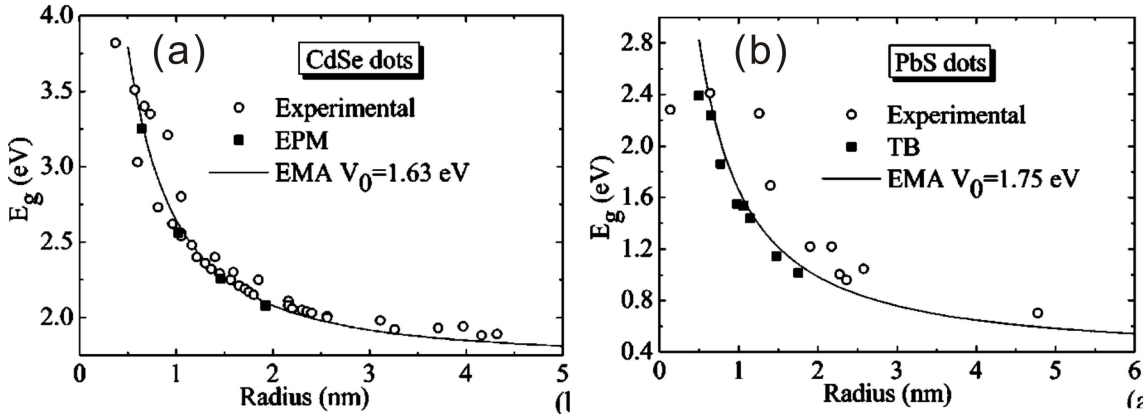

Figure 2.8: Calculated and experimentally measured band gaps in dependence on the QD radius for wide-gap CdSe QDs (a) and narrow-gap PbS QDs (b) [46]. The bulk band gap is 1.74 eV for CdSe and 0.41 eV for PbS, respectively. The solid line represents the result calculated with the FWEMA model. The solid squares in (a) represent the results predicted by an empirical pseudopotential method (EPM) and those in (b) are the results calculated based on a tight binding (TB) model.

2.4.1 Energy level structure

In the effective mass approximation model described in the above section, the energy bands are simplified to be parabolic. To obtain more accurate calculations, more realistic band structures have been considered. For binary semiconductors having zinc blende or wurtzite lattice symmetry, their conduction bands are formed by *s*-like atomic orbitals of the cations while the valence bands originate from *p*-like orbitals of their group VI elements. Therefore, the hole levels in the valence band are generally six-fold degenerate when spin is taken into account.

Figure 2.9 shows the schematic of the bulk band structures for zinc-blende and wurtzite type crystals. The valence band is split into three subbands by the spin-orbit interaction for each symmetry. Their dispersions are neither parabolic nor isotropic, with distinctly different effective hole masses. These valence subbands are classified with reference to the total angular momentum j, representing the sum of the orbital angular momentum and the spin angular momentum. The top two subbands have $j = 3/2$ and the lowest subband has $j = 1/2$ (Fig. 2.9). The subscript of j represents the projection of the total angular momentum. For zinc-blend symmetry, the valence subbands are referred to, from top to down, as heavy-hole (HH) band, light-hole (LH) band, and the spin-orbit split off (SO) band, respectively. The top of the HH and LH bands overlap and form a four-fold degenerate state at $\boldsymbol{k} = 0$. This degeneracy is lifted in the $\boldsymbol{k}$ space away from the Brillouin zone center. In wurtzite-type crystals, as described for the band structure of ZnO, the degeneracy of the two uppermost valence bands is eliminated due to the crystal-field splitting. These separated three valence bands are denoted, like in ZnO, as A-, B-, and C- band.

Based on the zinc-blende type energy band model, Ekimov et al. developed a theoretical calculation for the energy levels and the transition oscillator strengths in CdSe QDs [53]. Due to the wide band gap of CdSe (1.74 eV), the coupling between carriers in the conduction band and the valence band is ignored. The energy levels of electrons and holes are calculated independently. The Coulomb attraction between them is added afterwards. This theoretical

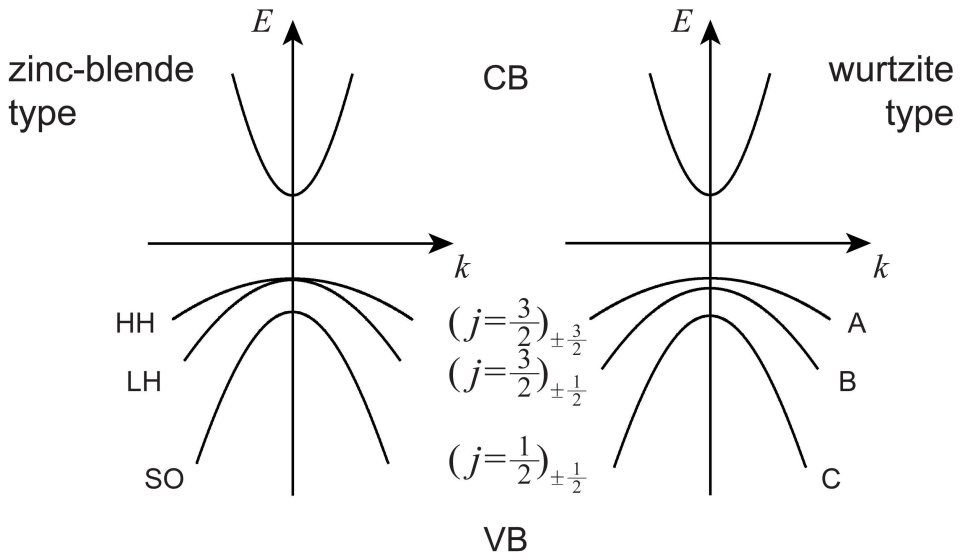

Figure 2.9: Schematic of the band structures of zinc-blende-type and wurtzite-type semiconductors [52].

model is referred to as a six-band model, corresponding to the six-fold degenerate valence band of the QDs.

In Fig. 2.10(a) the calculated energies of electron and hole levels with respect to the band edges for CdSe QDs are plotted versus the reciprocal of the squared QD radius. The notation for the hole states is as follows: for nL_j, j is the total angular momentum, $L = S, P, D, ...$ is the notation for the minimum orbital angular momentum (0, 1, 2, ...), and n is the ordinal number of the level with a given symmetry (e.g. $S_{3/2}$). The superscripts in $nP^l_{1/2}$ and $nP^{so}_{1/2}$ denote the states of light holes and holes in the split off band, respectively. The P-type hole levels are indicated by dashed lines. The hole ground state is an even state with total angular momentum $j = 3/2$ and orbital momenta 0 and 2. The energy levels deviate from a linear dependence on the reciprocal of the squared QD radius, due to the nonparabolicity of the energy bands. When the QD size decreases, all levels retreat away from the band edges, corresponding to the broadening of the band gap.

2.4.2 Optical transitions

The change in the energy band structure of semiconductor QDs has essential influence on their optical properties. As a result of their discrete energy levels, the absorption spectra of semiconductor QDs are generally characterized with multiple peaks and size-dependent onsets. The transition probability between different electron and hole energy levels is determined by the square of the wave function overlap [53]:

$$K = |\langle k, l, m \mid n, J, M \rangle|^2 \tag{2.15}$$

where k,l,m and n,J,M are quantum numbers denoting the electron and hole states, respectively. The transition energy is given by

$$\hbar\omega = E_{g,bulk} + \Delta E_e + \Delta E_h + E_{eh} \tag{2.16}$$

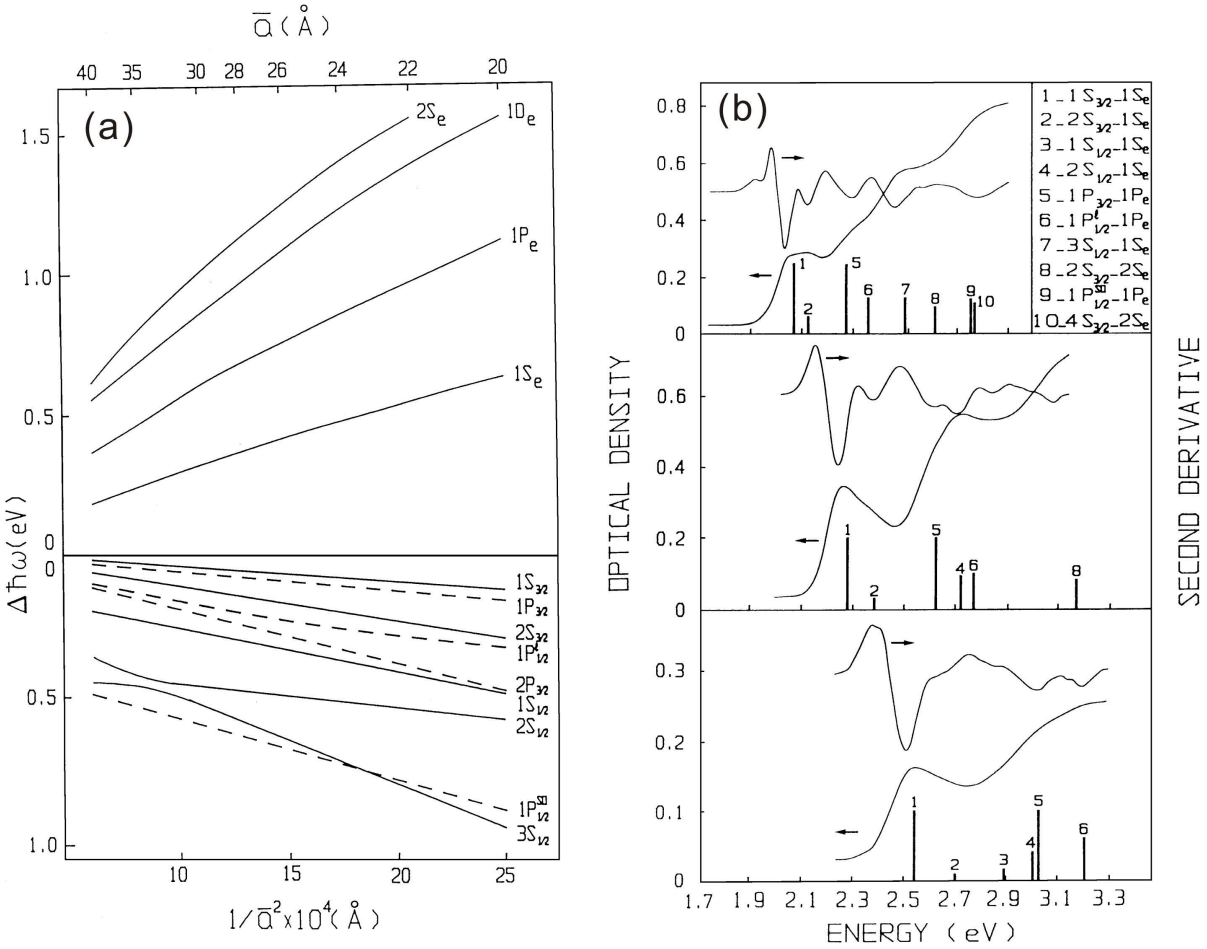

Figure 2.10: (a) Calculated electron and hole levels in CdSe QDs are plotted versus the reciprocal of the spared QD radius. The electron energies are relative to the bottom of the conduction band and the hole energies are referred to the top of the valence band. Only those levels involved in transitions with significant oscillator strength are shown. The P-type hole states are indicated by dashed lines. (b) Absorption spectra of CdSe QDs with three different mean radii (from top to bottom 3.8, 2.6 and 2.1 nm) compared with the theoretically calculated transition positions indicated by vertical bars. The height of the bars indicates the relative transition strength. The inset shows the assignments of these transitions. The pictures are from Ref. [53].

where $E_{g,bulk}$ is the bulk band gap. ΔE_e and ΔE_h are the energy retreats of electron and hole levels from the band edges as shown in Fig. 2.10(a). The last term E_{eh} is the Coulomb attraction energy between electron and hole, which decreases the transition energy. Figure 2.10(b) shows the absorption spectra measured for CdSe QDs with three different mean radii (from top to down, 3.8, 2.6, and 2.1 nm), compared to the calculated transition positions (vertical bars) by the six-band model. The height of the vertical bars represents the calculated relative transition strength. The inset shows the assignments of these transitions. The absorption spectra have rich features with multiple well-resolved peaks. The absorption onset shifts to higher energy for smaller QDs. The curve shape also changes significantly with the QD size. The resolved peaks coincide well with the calculated positions.

The optical transitions in semiconductor QDs have the following important properties:

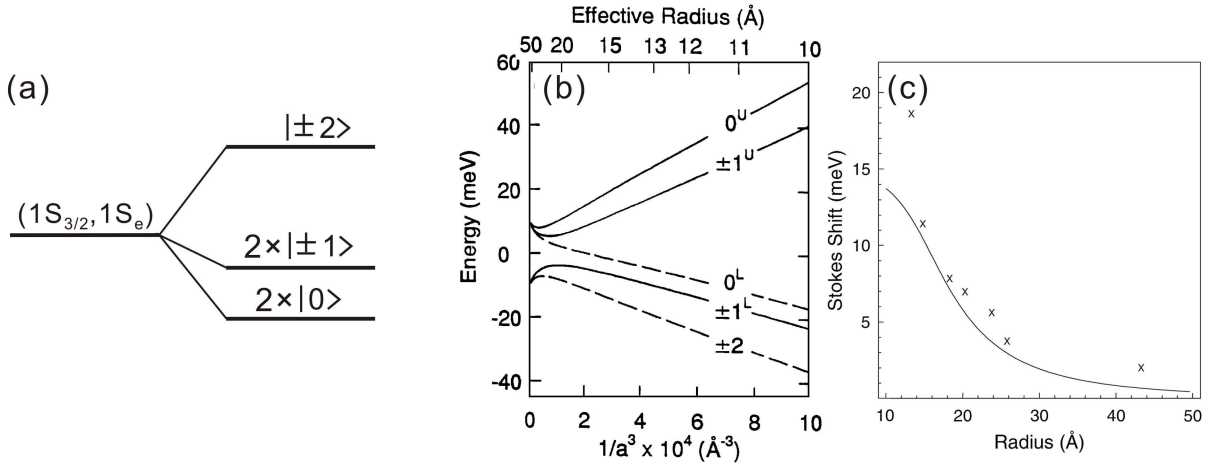

Figure 2.11: (a) Schematic of splitting of the ground exciton state in CdSe QDs. The resulting levels are denoted by the projection of the total angular momentum of the exciton state. (b) The size dependence of the ground exciton fine structure in CdSe QDs with elliptical particle shape. Solid (dashed) lines indicate optically active (inactive) levels. (c) Comparison between the experimental size dependence of the Stokes shift (crosses) and the theoretical calculation (solid line) which is defined as the energy spacing between the lowest optically active and inactive levels in image (b). The images (b) and (c) are reprinted from Ref. [57].

(1) The transition energies increase with decreasing QD size.
(2) Selection rules exist to fulfill that the integration in Equ. 2.15 is nonzero. Transitions to the S_e electron states are permitted from the $S_{3/2}$ and $S_{1/2}$ hole states. Transitions to the P_e electron level are possible from the $P_{3/2}$, $P^{l}_{1/2}$, $P^{so}_{1/2}$, and $P_{5/2}$ hole states. Moreover, transitions between the D_e electron levels and the $S_{3/2}$, $S_{1/2}$, $D_{5/2}$, and $D_{7/2}$ hole levels are permitted.
(3) The relative transition strength strongly depends on the particle size of the QDs, as shown in Fig. 2.10(b). Transition 3 ($1S_{1/2}$-$1S_e$), for instance, is only observed in the absorption spectrum of 2.1 nm CdSe QDs (bottom).

In addition, it is demonstrated by later work that the energy levels of CdSe QDs are quite insensitive to the zinc-blende type or wurtzite type crystal structure used for calculations. Both of them give rise to similar results [54, 55].

2.4.3 Stokes shift and the fine structure of the ground exciton state

In the optical spectra of semiconductor QDs, their photoluminescence is normally red-shifted in energy with respect to the lowest absorption peak arising from the fundamental transition $1S_{3/2}$-$1S_e$. This shift is in the order of 100 meV for CdSe QDs with a diameter of 1.6 nm. In addition, the lifetime of the photoluminescence is unusually long (up to 1 µs observed at 10 K) compared to that of the bulk material ($\tau \sim 1$ ns) [56]. Such phenomena have been observed in many semiconductor QDs, like CdSe, InP, and InAs QDs, and are referred to as the Stokes shift [57]. The origin of this effect involves the splitting of the ground exciton state of the QDs and the presence of so-called dark excitons.

While the absorption spectra of semiconductor QDs are mostly defined by the oscillator strengths of optical transitions between electron and hole levels, the excitonic photoluminescence is fur-

ther dependent on the population of electron-hole pairs at the band edges. As presented above, the ground exciton state in zinc-blende type CdSe QDs consists of the two-fold degenerate $1S_e$ electron state and the four-fold $1S_{3/2}$ hole state. It is in total eight-fold degenerate. This degeneracy can be lifted in a practical dot due to the asymmetry in the particle shape, the electron-hole exchange interaction, and perhaps the crystallization of the QD in hexagonal symmetry [58]. These effects become more significant in smaller QDs. As a result, the ground exciton state is split into five levels.

Figure 2.11(a) schematically shows the splitting of the band-edge exciton state. The resulting five levels are labeled by the projection of the exciton total angular momentum m_{ex}: there are one level with $m_{ex} = \pm 2$, two with $m_{ex} = \pm 1$, and two with $m_{ex} = 0$. In addition, the $|\pm 2\rangle$ and one of the $|0\rangle$ states are optically inactive in the electric dipole approximation. They can neither be excited by a photon nor recombine directly. These excitons are called dark excitons [58]. The energetic ordering of these five levels is very sensitive to the particle size and shape. In Fig. 2.11(b), the theoretically calculated size dependence of the exciton band edge structure in ellipsoid-shaped CdSe QDs is shown. The ellipticity of the dots used for calculation is derived from experimental data. The lowest exciton state is the dark $|\pm 2\rangle$ state, and the lowest bright exciton state is a $|\pm 1\rangle$ state. For absorption measurements, the absorption onset is arising from the fundamental transition of the lowest bright excitons $|\pm 1\rangle$. After photo-excitation, the bright excitons will relax quickly to the dark exciton state with lowest energy. These dark excitons finally recombine via interaction with phonons. Thus the lifetime for this recombination process is long. The emission energy is shifted relative to the fundamental absorption peak with amount of the energy spacing between the lowest dark exciton level and bright exciton level of the QDs. Fig. 2.11(c) compares the theoretical results of the size-dependent Stokes shift and the experimental observations, giving reasonable agreement in the order of the magnitude.

2.4.4 Phonon bottleneck in hot electron relaxation

When a bulk semiconductor is photo-excited over the band gap, the generated hot electron-hole pairs will relax to the band edges through efficient phonon coupling typically within a subpicosecond time scale, as depicted in Fig. 2.12(a). The situation is different for low-dimensional QDs, in which the energy level spacing is significantly increased. In CdSe QDs, as shown in Fig. 2.10(a), the energy spacing between the lowest two electron levels ($1S_e$ and $1P_e$) is several hundred meV. It is far larger than the longitudinal optical phonon energy of $\sim$ 25 meV in CdSe [60]. In comparison, the spacing of hole levels is much narrower, mostly due to their larger effective hole masses. As a result, the thermal relaxation of hot electrons at higher levels via phonon emission is hindered dramatically in QDs (Fig. 2.12(b)), which is referred to as a phonon bottleneck phenomenon [61, 62].

A significantly prolonged lifetime of hot electrons, however, is not commonly observed in semiconductor QDs. Several mechanisms are proposed to help the electron relaxation [59]. The hot electrons can relax by transferring their energy to holes which have a higher density of states and thus can relax afterwards via coupling with phonons (Fig. 2.12(c)). In addition, surface defects in QDs may insert energy states between the electron levels, which can provide relaxation channels for hot electrons (Fig. 2.12(d)). The electrons can also transfer their energy to the vibrations of surfactant ligands of the QDs (Fig. 2.12(e)). Long lifetimes up

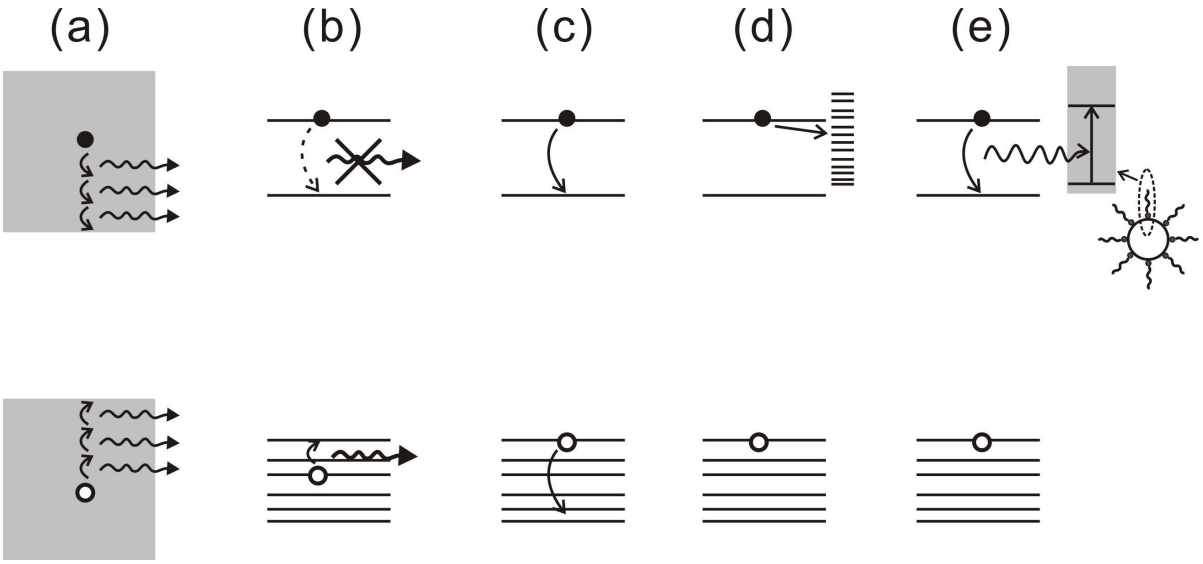

Figure 2.12: (a) Charge carrier relaxation in bulk semiconductor via emission of phonons. (b) Hot electron relaxation via phonon emission in semiconductor QDs is unlikely. (c) Electron can cool by transferring its energy to a hole with higher density of states. (d) Electron can relax via surface trap states. (e) Electron can transfer its energy to the high-frequency vibration of the surfactant ligands. The figure is based on Ref. [59].

to 1 nanosecond in CdSe QDs has been reported by growth of multiple semiconductor shells outside the QDs to eliminate their surface defects and modify the confinement of charge carriers [59].

2.5 Synthesis of colloidal semiconductor quantum dots

A typical reaction system for wet chemical synthesis of colloidal semiconductor QDs consists of three components: precursors, the organic surfactant and the solvent, while in some cases one chemical acts as both surfactant and solvent [63]. The precursors are chemical sources serving one or more atomic species for the desired QDs. Under specific reaction conditions, e.g. temperature and precursor concentrations, the precursors chemically react and form atomic or molecular complexes that work as basic building blocks for the QDs. These fundamental species are called monomers. The formation of the QDs can be generally divided into two stages: the nucleation of the active monomers and the subsequent growth of the formed nuclei [44, 63]. The first stage relies on a quick decomposition and reaction process of the precursors, which can induce a transient supersaturation of the monomers. This supersaturation is reduced by the nucleation process of the monomers. Afterwards, the formed nuclei grow gradually by incorporation of the residual monomers from the solution.

There are two important factors for the preparation of QDs: one is the quality of the dots including their crystallinity and the surface passivation quality with surfactant ligands. The other is the QD size distribution. Narrow size distribution is crucial for research on the size dependent properties of QDs and the related applications, like lasing and light-emitting devices. Generally, the preparation of QDs with narrow size distribution requires an instantaneous nucleation stage of the monomers to generate homogeneous QD “seeds”. Therefore, an

important issue for QD synthesis is the choice of suitable precursors which should react rapidly at a specific temperature during the synthesis to yield quick supersaturation of the monomers. The subsequent growth is largely affected by the surfactant molecules. During growth, these molecules are dynamically bound on the QD surfaces. The binding energy needs to be at such a level that it permits the surfactants to be transiently removed from the QD surfaces to allow the addition of extra monomers for particle growth, while at long time scale the QDs are still effectively capped to avoid aggregation [63].

2.5.1 Synthesis mechanism

In this subsection, the general synthesis mechanism for colloidal semiconductor QDs is presented. A solution under supersaturation possesses a high Gibbs free energy, which would be reduced by forming a solid phase. For formation of a spherical nucleus with a radius r, the total change of the Gibbs free energy is given by

$$\begin{aligned} \Delta G &= \Delta\mu_v + \Delta\mu_s \\ &= \frac{4}{3}\pi r^3 G_v + 4\pi r^2 \gamma \end{aligned} \tag{2.17}$$

with

$$G_v = -\frac{k_B T}{\Omega} ln(S) \tag{2.18}$$

where G_v is the Gibbs free energy per unit volume of the solid phase and γ is its surface energy per unit area. Ω is the molar volume of the material, k_B is the Boltzmann constant, and T is the absolute temperature. S is the supersaturation of the solution defined by $S = C/C_0$, wherein C and C_0 are the solute concentration and its concentration at soluble equilibrium, respectively. The two terms $\Delta\mu_v$ and $\Delta\mu_s$ in Equ. 2.17 are arising from the changes in the volume and surface area of the solid nucleus, respectively. According to Equ. 2.18, formation of solid volume in a saturated solution ($S > 1$) always reduces the Gibbs energy. However, this reduction is balanced by the increase of surface energy $\Delta\mu_s$.

Figure 2.13 schematically shows the change of the volume free energy $\Delta\mu_v$, the surface free energy $\Delta\mu_s$ and the total free energy ΔG as a function of the radius of the generated nucleus. The absolute magnitudes of $\Delta\mu_v$ and $\Delta\mu_s$ increase with increasing nucleus radius. There is a critical nucleus size r^* for the variation of the total free energy ΔG. Nuclei smaller than r^* will dissolve gradually into the solution to reduce their total free energies, whereas nuclei larger than r^* are stable and will continue to grow to to further reduce their free energies. It is easy to obtain this critical radius at a given supersaturation S by solving the differential $d\Delta G/dr = 0$, which yields

$$r^* = \frac{2\Omega\gamma}{k_B T ln(S)} \tag{2.19}$$

with the corresponding free energy maximum in the growth process of nuclei

$$\Delta G^* = \frac{16\pi\gamma}{9G_v^2} \tag{2.20}$$

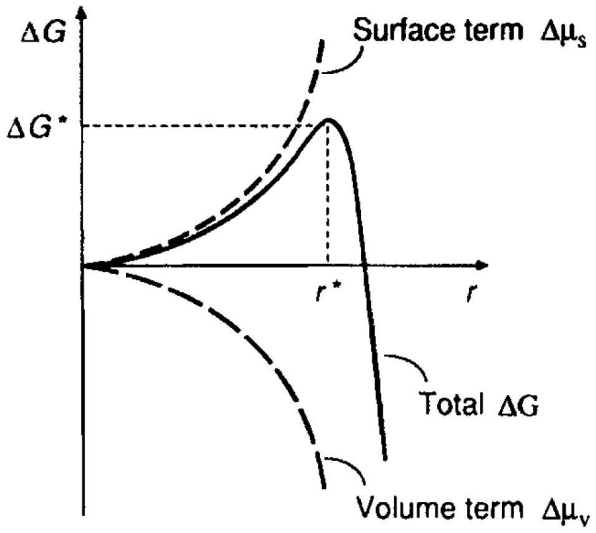

Figure 2.13: Schematic illustration of the variations of the volume free energy $\Delta\mu_v$, the surface free energy $\Delta\mu_v$, and the total free energy ΔG as a function of the nucleus radius [64].

Equation 2.19 defines the minimum radius that will persist and continue to grow to bigger particles. Thus, to initiate the nucleation process of a supersaturated solution, S should reach an sufficiently high level for the system free energy to overcome the critical energy barrier ΔG^*.

Figure 2.14 schematically shows a nucleation burst scheme proposed by LaMer et al. for the synthesis of monodisperse colloids [65]. It can be used to illustrate the change of the monomer concentration during the nucleation process in the synthesis of semiconductor QDs. The supersaturation boundary $S = 1$ and the critical supersaturation level S_c corresponding to the free energy barrier (ΔG^*, Equ. 2.20) for monomer nucleation are marked. In stage I, the monomer concentration in the solution continuously increases by either external addition or in situ generation. As long as the supersaturation is below the critical level S_c, no nucleation occurs. Once the supersaturation exceeds this critical level in stage II, the monomers agglomerate to-

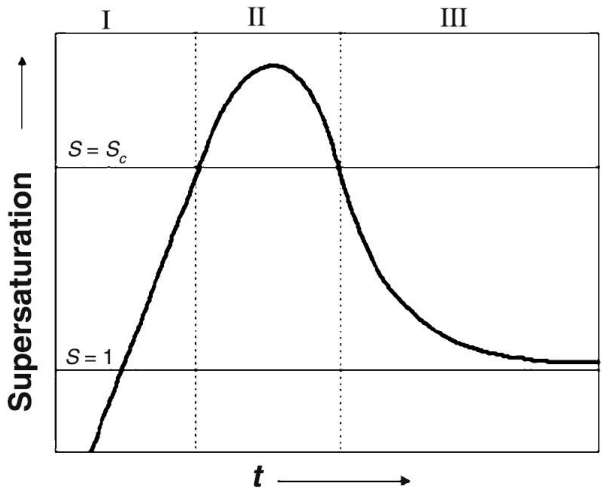

Figure 2.14: LaMer plot: the change of supersaturation degree as a function of reaction time during nanocrystal synthesis [65].

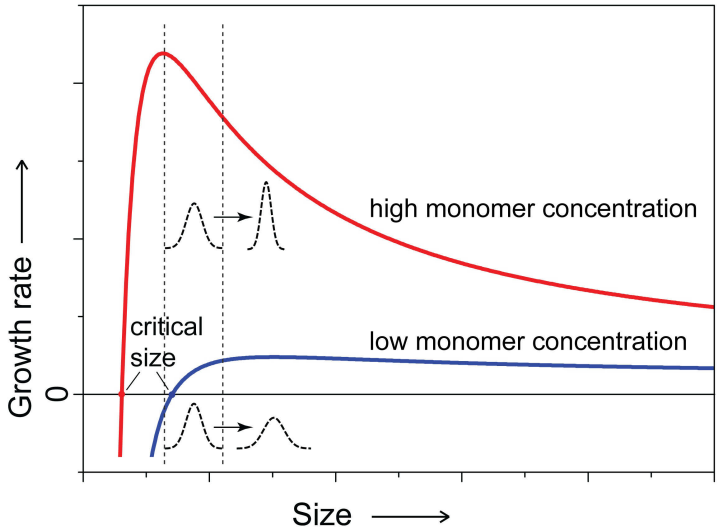

Figure 2.15: Growth rate of nanoparticles versus particle size at high (red line) and low (blue line) monomer concentrations [63]. The dashed lines represent size distributions of nanoparticles present in solution and their variations after a short period. At high monomer concentration, a size focusing occurs while the size distribution broadens at low monomer concentration, as a result of the Ostwald ripening.

gether and nucleate, which quickly reduces the monomer concentration and thus the degree of supersaturation to under S_c. Afterwards, the produced nuclei act as nanocrystal seeds and continue to grow on the expense of the residual monomers in stage III.

The average size and size distribution of the prepared QDs depend on the subsequent growth process. This growth process can be illustrated by the classic crystallization theory. The chemical potential μ_r of a crystal nucleus with a radius r and that of the monomers μ_m in solution can be expressed as [66]

$$\mu_r = \mu_\infty + 2\gamma\Omega/rk_BT \tag{2.21a}$$

$$\mu_m = \mu_m^\circ + k_BTln(R_mS) \tag{2.21b}$$

where μ_∞ is the chemical potential for crystal with infinite size, and μ_m° is the standard chemical potential of the monomers. R_m is the chemical activity coefficient of the monomers, which can be tuned by the surfactant ligands and their concentration in the reaction solution for QD synthesis. When $\mu_r < \mu_m$, the monomers will deposit onto the nucleus surface for particle growth. Otherwise, the nucleus will shrink and dissolve into the solution. According to Equ. 2.21, μ_r and μ_m are dependent on the nucleus size and the monomer concentration in the solution, which vary continuously during the growth process. The interaction between them dominates the growth dynamics of the QDs.

Figure 2.15 schematically illustrates two growth rate curves dependent on the QD size for high (red line) and low (blue line) monomer concentrations in the reaction solution, according to a model proposed by Sugimoto [67]. The positive growth rate represents particle growth whereas the negative rate implies the shrinking of the particles. The critical particle size (r_0) for zero growth rate shifts to larger value with decreasing monomer concentration.

The growth of the QDs after monomer nucleation can be divided into two stages. At the early stage, the concentration of the residual monomers is high (red line in Fig. 2.15) and r_0 is small.

All nuclei have positive growth rates while the growth rates for smaller particles are larger. Thus, they grow quickly by incorporation of the monomers from the solution. As a result, an important size-focusing process occurs. When the monomers in solution are depleted, the critical size r_0 significantly increases. Ultimately, there will be a part of the particles having sizes smaller than r_0 (blue curve). Then an Ostwald ripening process starts, in which smaller particles shrink gradually while the larger ones continue to grow at the expense of the dissolved particles. The monomer concentration in this stage keeps nearly constant while the total number of the particles reduces. As a result, the particle size distribution broadens. To avoid this size-defocusing stage, new monomers can be added which would shift the critical size r_0 back to smaller values [68].

Generally, the synthesis of QDs requires to be carried out at elevated temperatures. This on the one hand, ensures the sufficient reactivity of the reagents. On the other hands, the elevated temperature also provides effective annealing of the QDs to improve their crystallinity. The temperature that can achieve atomic rearrangement is therefore correlated to the melting point of the material, which is significantly reduced in nanometer-scale QDs. It is typically in range of 200-400 °C and can be realized in common organic solvents [63].

According to the used solvent environments, the wet chemical synthesis methods of semiconductor QDs are commonly classified into two categories: organic phase synthesis and aqueous phase synthesis [69].

2.5.2 Organic phase synthesis

Up to now, the most successful synthesis of colloidal semiconductor QDs in terms of crystallization quality and monodispersity is achieved in organic phase [44, 48, 71]. A typical synthesis setup and the temporal variation of the precursor monomer concentration in the reaction system are schematically shown in Fig. 2.16. The solvent is placed in a flask and heated to typically 150–350 °C. Synthesis has to be carried out under inert gas atmospheres in some cases. The precursor reagents are rapidly introduced into the hot solvent with a syringe, which results in a quick decomposition and reaction of the precursors and raises instantaneously the supersaturation of the monomers. This supersaturation leads to a short nucleation burst. Afterwards, the formed nuclei gradually grow under gentle heating. The growth should be stopped before the Ostwald ripening process to avoid the size-defocusing effect.

Commonly used organic solvents include trioctylphosphine (TOP), trioctylphosphine oxide (TOPO), fatty acids, and amines [44, 72, 73].

2.5.3 Aqueous phase synthesis

Aqueous phase synthesis shares the similar nucleation and growth processes with the organic phases [69, 74].Typically, the metal salts of the cation precursor and surfactants are dissolved in water to form a reaction solution. The pH value is adjusted with a basic solution (e.g. NaOH solution) to a specific value. Then the separately prepared anion precursor is added, resulting in supersaturation of the monomers and nucleation burst. Generally, the nucleation in aqueous phase is much slower than that in high temperature organic phases. It could coexist with the nuclei growth process for a period. The formed nuclei grow under further thermal treatment

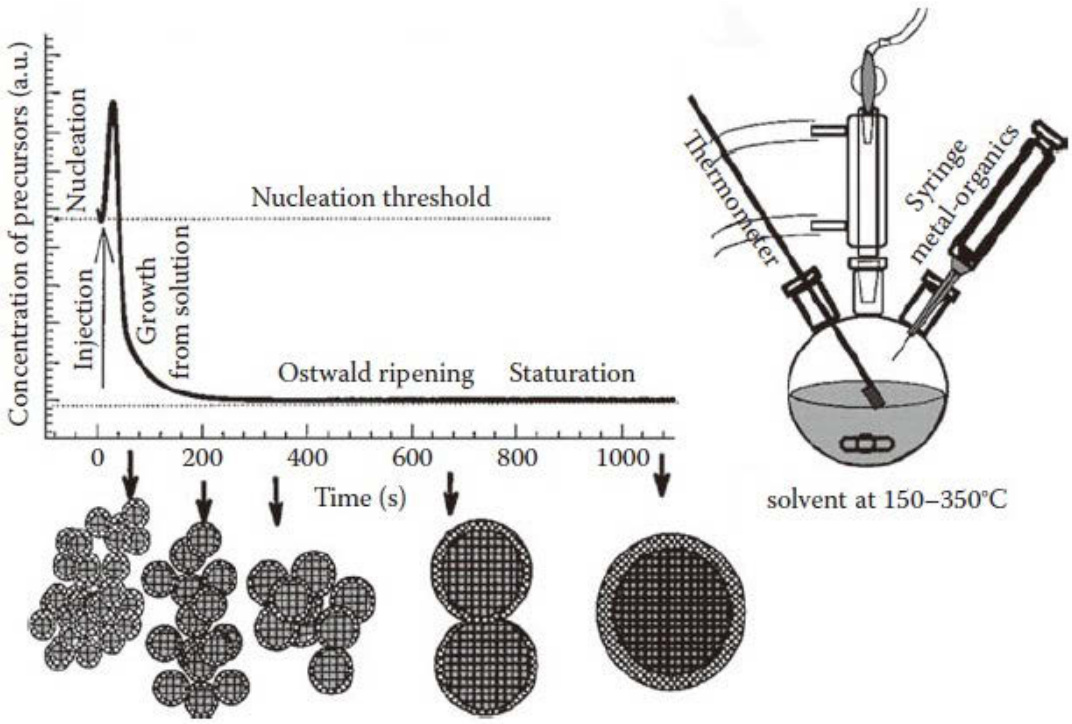

Figure 2.16: Scheme of crystal growth over time (left) and representation of the simple synthetic apparatus (right) employed in the preparation of monodisperse semiconductor QDs, taken from Ref. [70].

of the reaction system (refluxing, microwave irradiation, or UV light irradiation). The most commonly used surfactants in aqueous phase synthesis are various thiols [74–76]. Sometimes, carboxyl compounds and amines are also used for this purpose.

Due to the low boiling point of water relative to the organic solvents, the highest available synthesis temperature is confined, inducing low reactivity of the chemicals. Thus QD growth in aqueous phase is much slower than the organic phase synthesis, and in some cases it takes several days to reach the desired particle sizes. Moreover, the slow nucleation process of the monomers will produce QD seeds with large nonuniformity in their sizes. The low synthesis temperature cannot provide an effective annealing of the QDs during growth as well. Therefore, QDs synthesized in aqueous phase commonly suffer from low crystallinity and broad size distribution. However, aqueous phase methods are simpler and more friendly to the environment. More inorganic salts can be well dissolved in water, providing flexible sources for the metal precursors. Furthermore, by choosing proper bifunctional surfactants, it is possible to vary the surface functionality of the produced QDs, which is of great interest for conjugation of QDs with other materials to build hybrid structures. Therefore, aqueous phase methods provide important alternatives for the preparation of colloidal semiconductor QDs.

Chapter 3

State of Research

This chapter presents a brief overview of the state of research on ZnO materials, their photoluminescence, and the research on ZnO nanowires. It also includes the state of research on colloidal semiconductor quantum dots and hybrid structures of ZnO nanowires functionalized with semiconductor quantum dots.

3.1 ZnO and its optical properties

The research on ZnO can be traced back to the 1930s starting with the analysis of its crystal structure, ion radii, density, and basic electrical and optical properties, etc. [77]. Driven by the availability of high quality bulk single crystals and the epitaxial layers, ZnO research obtained its first peak between the end of the 1960s to the mid 1980s. Vibrational properties of ZnO were studied by Damen et al. [78] in 1966 by Raman scattering spectroscopy. ZnO growth by chemical vapor transport was obtained in 1970 [79]. In terms of devices, Au Schottky barriers were formed in 1965 [80]. ZnO based light emitting diodes were demonstrated in 1967 [81] wherein Cu_2O was used as the p-type material. Metal insulator semiconductor (MIS) structures were reported in 1974 [82]. ZnO/ZnTe p-n junctions were fabricated in 1975 [83], and Al/Au ohmic contacts were reported in 1978 [84].

3.1.1 Near-band-edge emission

Due to its wide direct band gap and efficient exciton emission, ZnO has attracted wide research interest for its promising applications in optoelectronics. The optical properties of ZnO, especially its near-band-edge excitonic emission, were widely studied since the 1960s. High resolution measurements at low temperatures found that the near-band-edge emission of ZnO has rich features [85] and shows many resolved emission lines. These emission lines with specific energies are mainly arising from transitions of different free excitons, excitons bound to donor and acceptor centers, their two electron satellites and phonon replicas. There are in total about twelve different emission lines in the near-band-edge luminescence that have been reported in literature, which are listed in Table 3.1, summarized by Meyer et al. [38]. These emission lines were generally numbered from I_0 to I_{11} in the early work of Reynolds et al. [86].

Table 3.1: Free and bound exciton recombinations and related properties (T = 4.2 K) [38].

line	wavelength (nm)	energy (eV)	localization energy (meV)	two-electron-satellite separation ($2P_{xy}-1S$) (meV)	donor binding energy (meV)	chemical identity
A_L *	367.12	3.3772				
A_T *	367.26	3.3759				
I_0	367.63	3.3725	3.4			
I_1	367.71	3.3718	4.1			
I_{1a}	368.13	3.3679	8.0			
I_2 **	368.19	3.3674	8.5			
I_3 **	368.29	3.3665	9.4			
I_{3a}	368.34	3.3660	9.9			
I_4	368.34	3.3628	13.1	34.1	46.1	H
I_5	368.86	3.3614	14.5			
I_6	368.92	3.3608	15.1	38.8	51.55	Al
I_{6a}	368.96	3.3604	15.5	40.4	53	
I_7	369.01	3.3600	15.9			
I_8	369.03	3.3598	16.1	42.1	54.6	Ga
I_{8a}	369.08	3.3593	16.6			
I_9	369.37	3.3567	19.2	50.6	63.2	In
I_{10}	369.76	3.3531	22.8	60.2	72.6	
I_{11}	370.28	3.3484	27.5			

* A_L and A_T are the longitudinal and transversal free A-exciton states. A_T is the reference for the determination of the bound exciton localization energy.
** I_2 and I_3 are assigned to ionized donor bound exciton recombinations.

In bulk ZnO crystals, the free exciton is observed at about 3.377 eV. The emission lines I_2 and I_3 at around 3.367 eV were assigned to ionized donor bound excitons by Reynolds in 1965 [86]. The assignments of the emission lines with lower energies still have controversy. The lines positioned between 3.3628 and 3.359 eV (I_4–I_{8a}) were attributed to neutral donor bound excitons by some experimental studies [87]. However, based on detailed high-resolution magneto-optical and excitation spectroscopy measurements, Gutowski et al. [88] in the 1990s comprehensively analyzed the electronic states and emission of acceptor-exciton complexes in ZnO, and they attributed the recombinations from I_5 to I_{10} to acceptor bound excitons. In addition, through the investigations on the emission line strength dependent on the doping extent, Tomzig assigned two emission lines at 3.356 and 3.353 eV (I_9 and I_{10}) to excitons bound to neutral Li and Na acceptors [85].

Meyer et al. recently carried out extensive studies on the near-band-edge excitonic recombinations in undoped ZnO crystals by photoluminescence and spatially resolved cathodoluminescence measurements [38]. They reported the binding energies of four shallow donors (H, Al, Ga, In) and assigned the emission lines observed between 3.353 and 3.363 eV to the corresponding donor bound excitons, as listed in Table 3.1. They also identified emission bands originating from donor-acceptor pair transitions in which nitrogen was believed to be the involved acceptor. Thonke et al. [89] observed transitions at 3.32, 3.33 and 3.333 eV in

undoped bulk ZnO, and assigned them to two-electron satellite transitions of neutral donor bound excitons.

3.1.2 Excitation-intensity-dependent photoluminescence

The photoluminescence spectra of a direct band gap semiconductor generally consist of two main parts of emissions: one is the near-band-edge emission originating from interband transitions. The other part is related to deep levels in the band gap induced by defects or chemical impurities, resulting in one or several emission bands. The relative strengths of these emission bands vary with excitation intensity. In other words, the luminescence properties of a semiconductor are excitation-intensity-dependent. Analysis of the dependence can give insight into the recombination processes in the material and the information about the deep centers.

One typical work on the excitation intensity dependence of the photoluminescence properties in a semiconductor was performed by Reshchikov and Korotkov in 2001 on undoped GaN films [90]. A continuous-wave He-Cd laser (photon energy 3.81 eV) was used as excitation source with its power density varying in the range of 10^{-5}–35 W/cm^2. The photoluminescence of the GaN films at room temperature exhibited a typical deep-level related yellow luminescence (YL) band peaking around 2.2 eV and a near-band-edge emission band. They measured the evolution of the YL band with excitation intensity. A model was established in the linear optics regime for the photo-excitation and relaxation processes in GaN. The interactions among charge carriers and excitations are ignored except for recombination processes. It assumed two types of deep centers: acceptor-type and donor-type centers, which are responsible for the YL emission and the non-radiative relaxation, respectively. The recombination rates were represented by the corresponding bimolecular recombination coefficients. Based on the balance between the generation and recombination of charge carriers at equilibrium, they calculated the dependence of the recombination rates of different channels on the excitation intensity.

Figure 3.1(a) shows the calculated evolutions of the deep-level emission intensity (I_i^{PL}), the photogenerated electron (δn) and hole (p) concentrations in GaN with the electron-hole pair generation rate G. At low excitation intensity (region I), I_i^{PL} increases linearly with G. Increasing excitation intensity induces a saturation-like behavior of the I_i^{PL} (region II). However, further increase of the excitation intensity makes I_i^{PL} rise again (region III). After another saturation-like stage (stage IV), the I_i^{PL} finally changes to a square-root dependence on the generation rate (stage V). The fitting results of the calculation to the experimental YL emission are shown in 3.1b, through which the authors determined the concentration of the acceptors in the GaN film responsible for its YL emission.

Cui et al. studied the excitation power dependence of the photoluminescence of ZnO in 2009 [91]. They investigated three types of ZnO samples, including sintered polycrystalline pellets, pulsed laser deposited thin films, and electrochemically grown nanowires. Figure 3.2 (a) and (c) present the photoluminescence spectra of ZnO pellets for different excitation intensities at room and low temperatures, respectively. With increasing laser power, the relative intensity of the band-edge emission (3.0–3.4 eV) and the deep-level emission (1.5–3.0 eV) change noticeably. Figure 3.2(b) plots the change of the emission maxima for those two bands against the laser power at room temperature. Both emission bands increase nonlinearly with excitation. The intensity ratio between the defect emission and the band-edge emission de-

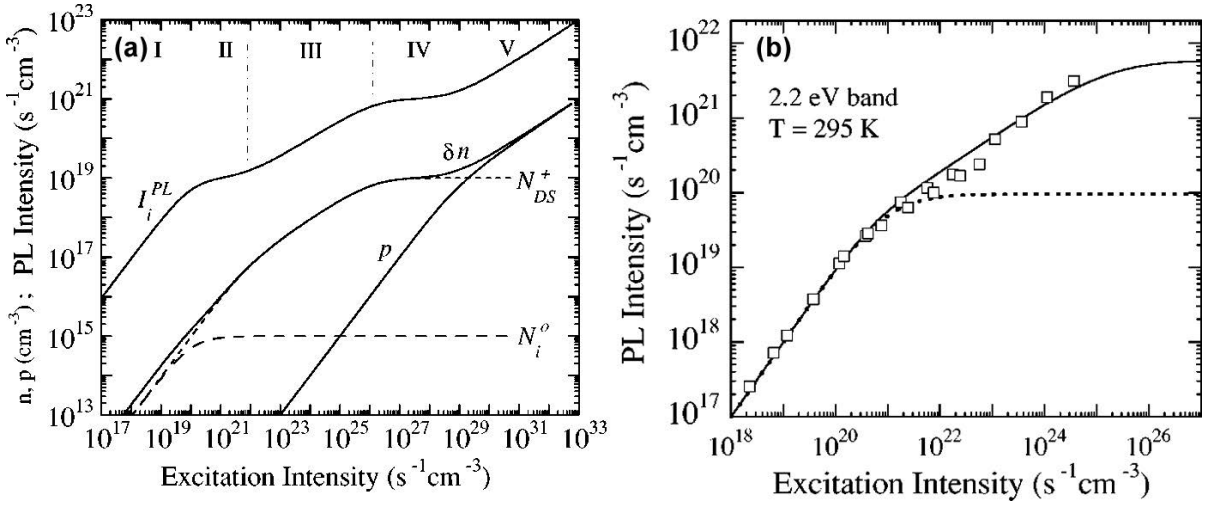

Figure 3.1: (a) Calculated defect-related emission intensity (I_i^{PL}) and concentrations of photogenerated electrons (δn) and holes (p) versus excitation intensity in GaN with the linear optics model. (b) Dependence of the deep-level emission intensity on excitation intensity of GaN films at room temperature fitted with the calculated result (solid line). The images are from Ref. [90].

creases from about 125 for laser power of 0.015 mW to 17 for 12.8 mW. The low temperature spectra (Fig. 3.2c) show two defect emission bands peaking around 2.35 eV (green band) and 1.82 eV (red band), respectively. With increasing laser power, the green band becomes stronger and dominates the defect emission finally. Figure 3.2(d) plotted the change of peak positions of these two bands with laser power. When the laser power is increased, these two bands shift to higher energies (Fig. 3.2(d)), which is consistent with the properties of donor-acceptor pair (DAP) emissions. The energy of the DAP transition is estimated by [91]

$$E_{DAP} = E_g - E_D - E_A + \frac{e^2}{4\pi\varepsilon_0\varepsilon r_{DA}} \tag{3.1}$$

where E_g is the band gap of the material, E_D and E_A are the donor and acceptor binding energies, respectively. The last term is the Coulomb attraction energy between the donor and the acceptor, where r_{DA} represents the average donor-acceptor distance. When the excitation intensity is increased, the number of occupied donor and acceptor centers increases and their average distance r_{DA} decreases. Thus, the DAP recombination energy E_{DAP} increases. The authors accordingly assigned the defect emission in the ZnO pellet samples to DAP-type recombinations [91], as schematically shown in the inset of Fig. 3.2(d). Similar results were also observed on their investigated nanowire and film samples.

With increasing excitation intensity, the concentrations of the photogenerated charge carriers and excitons increase, and the interactions between them become more and more important, which gives rise to new phenomena and features in the optical properties. The scenario of the high excitation of ZnO was gradually developed from the 1970s [40, 92, 93]. In 1973, Hvam reported his studies on the exciton-exciton interaction in ZnO single crystal platelets at low temperatures (T = 10 K) [93]. The samples were excited with a pulsed electron beam with an acceleration voltage of 40 kV and a maximum current density of 7 A/cm^2. A new emission band at 3.327 eV was observed, which was interpreted as a result of exciton-exciton scattering in which one exciton is scattered into a higher energy state while the other is scattered onto

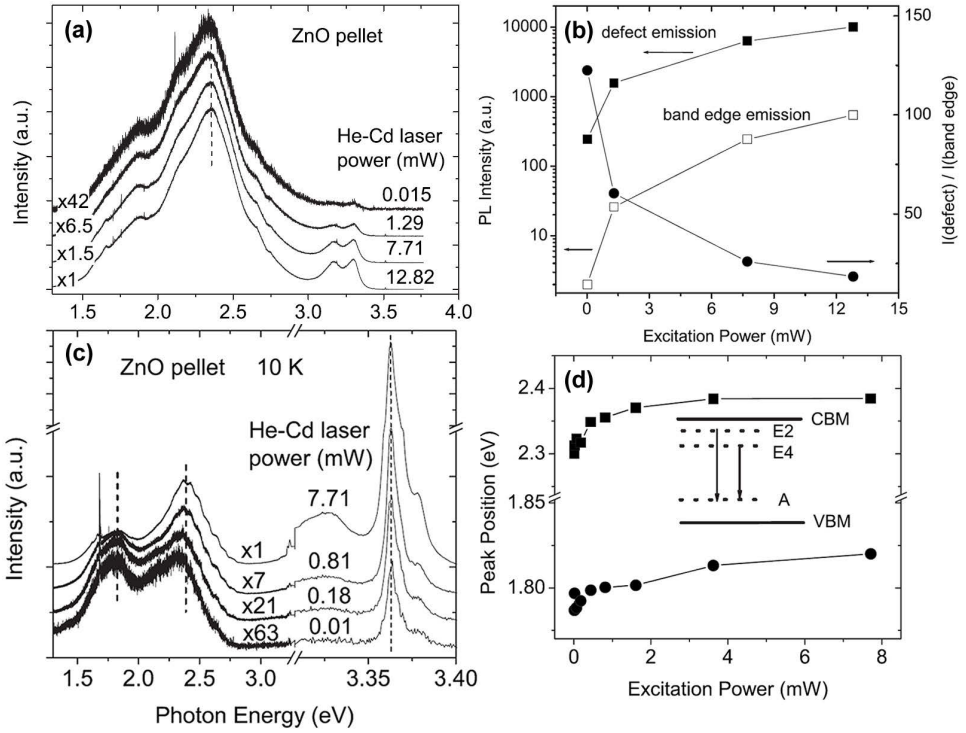

Figure 3.2: (a) Room temperature photoluminescence spectra of ZnO pellets excited with different laser powers. (b) Intensities of band-edge emission and defect related emission, and their ratio as a function of excitation power. (c) Photoluminescence spectra of ZnO pellets excited with different laser powers at $T = 10$ K. (d) Shifts of the luminescence peaks of the green (2.35 eV) and red emissions (1.82 eV) with the excitation power at 10 K. The images are from Ref. [91].

the photon-like part of the exciton-polariton dispersion and leaves the sample as a photon. The resulting new emission bands are commonly called the P bands [27].

Another effect at the high excitation regime of ZnO is the formation of biexcitons through the collision of two excitons at low temperature. The binding energy of a biexciton relative to two free excitons is around 15 meV in ZnO. The recombination of biexcitons gives rise to new emission band, called the M band [92]. Jen et al. studied the biexciton and donor bound biexciton emissions in high-quality ZnO thin films at low temperature [94]. Figure 3.3(a) shows the high resolution band-edge emission spectra they recorded with different excitation intensities. The band-edge emission is dominated by transitions of donor bound excitons (D^0X) at 3.37 eV. Increasing the laser intensity (1–6 kW/cm^2 at 360 nm) produced two extra bands at 3.361 and 3.353 eV, which were identified by the authors as the transitions of biexcitons (the M band) and the donor bound biexcitons (the D^0M band), respectively. They studied the excitation intensity dependence of these three emission bands. The results are shown in Fig. 3.3(b). The integrated luminescence intensities of all these three bands increase with excitation intensity by power law but with different exponents. The increase of the D^0X band has a slope of ~ 0.93, i.e. a sublinear dependence on excitation. The other two biexciton emission bands M and D^0M were found to increase superlinearly with excitation power.

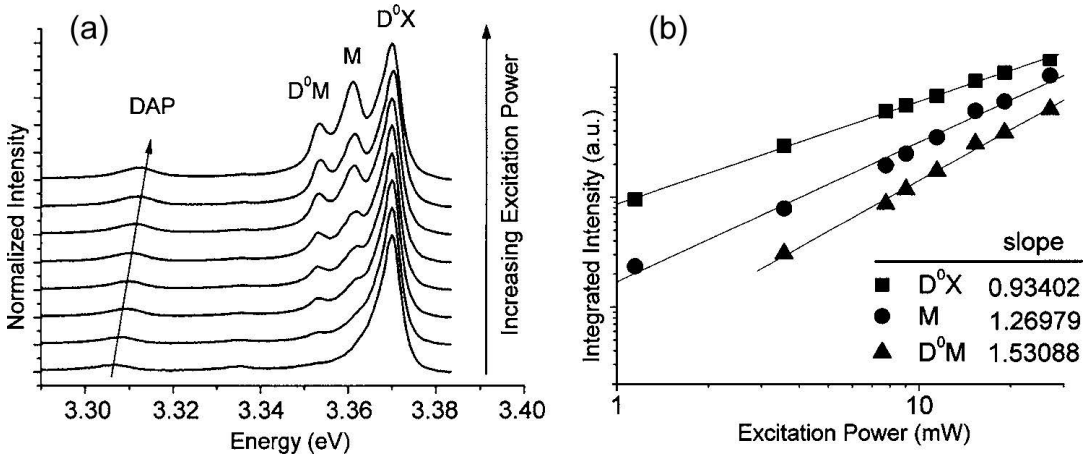

Figure 3.3: (a) Excitonic luminescence spectra of a ZnO thin film at 10 K for different excitation intensities. (b) Integrated luminescence intensities of the donor-bound exciton (D^0X), the M band of the biexciton, and the donor bound biexciton (D^0M) bands as a function of excitation power. The images are from Ref. [94].

3.2 Electrical properties of ZnO modulated by surface chemistry

The importance of the surface has been well-known in controlling the properties of semiconductors, which is especially true for nanostructured materials due to their much larger surface-to-volume ratios. In the atmosphere, many kinds of gas molecules and water vapor can be adsorbed on the surface of semiconductor crystals, which impacts their electronic structures and physical properties. Among these adsorbed molecules, oxygen is an important species due to its high reactivity, which has been widely studied.

As early as in 1957, Melnick studied the oxygen adsorption on porous sintered ZnO samples [95], which is one of the pioneering works on gas molecule adsorption on ZnO. He measured the photoconductivity of the samples with ultraviolet light illumination in gas environments with different oxygen pressures. Under illumination, the conductivity of the samples was found to increase dramatically and it was persistent for several hours after stopping the illumination. Based on the experimental observations, a model about oxygen adsorption on ZnO was proposed: in darkness, oxygen molecules are adsorbed on the ZnO surface and capture electrons to form oxygen ions. Under photoexcitation, these oxygen ions can react with the generated holes and are converted to be physically adsorbed and can be easily desorbed from the ZnO surface afterwards.

Adsorption of O_2, H_2, CO, NH_3, and NO_2 gas molecules on ZnO nanotubes was theoretically studied by An et al. using density functional theory (DFT) in 2008 [96]. The calculation indicated that surface defects are essential for gas molecules to form stable adsorption states on ZnO surface. For a defect-free ZnO single-walled nanotube (SWNT), O_2 and H_2 molecules are only physisorbed by van der Waals forces while the other three species are molecularly chemisorbed to form surface ions, acting as electron donors (CO and NH_3) or acceptors (NO_2). The adsorption on ZnO nanotubes containing oxygen vacancies (V_O) is more stable with increased binding energies. All gas molecules except H_2 are chemisorbed while O_2 adsorbates

act as strong electron acceptors. In addition, O_2 and NO_2 were found to dissociate near a V_O defect and one resultant atomic O would fill in the V_O site.

Oxygen adsorption was also found to significantly influence the properties of other semiconductor materials. Collins et al. reported the extreme sensitivity of the electronic properties of carbon nanotubes to gas environments in 2000 [97]. They investigated the electrical conductivity of single-walled carbon nanotubes (SWNT) in different gas environments. The electrical resistance R of the SWNT samples was found to decrease by up to 15% solely by changing the measuring environment from vacuum to air or oxygen. This effect is reversible. Alternating evacuation of the sample chamber and inflation with air or oxygen induced stepwise changes in the electrical resistance of the samples with reasonably a quick response (about 10 min) [97]. In contrast, inflation with an inert gas brought no change in R. The authors concluded that oxygen is the source that is modulating the conductivity properties of the carbon nanotubes.

Using scanning tunneling microscopy (STM), they further studied the effect of oxygen adsorption on the local density of electronic states in individual nanotubes. The results demonstrated that oxygen adsorption can induce a significant rearrangement of the electronic states of the nanotubes, which results in a shrinking of their band gaps to be metallic or semimetallic. In addition, electron transfer from the nanotubes to the adsorbed oxygen molecules was also proposed to be one important factor for the decrease in the resistivity, which could induce a hole-dominating (p-type) conductivity in the nanotubes.

3.3 ZnO nanowires

Semiconductor nanowires have become one of the most active research fields in the nanoscience community within the last decades. In 1965, Wagner et al. [98] proposed the dynamic equation $R_{min} = [(2V_l/(RTlns))]\sigma_{lv}$ for the vapor-liquid-solid (VLS) whisker growth, where R_{min} is the minimum whisker radius, V_l is the molar volume of the metal droplet, σ_{lv} is the liquid-vapor surface energy, and s is the degree of supersaturation of the vapor. Based on this, in the early 1990s, Yazawa et al. developed the growth of III-V nanowhiskers [99]. Later, good positional and orientational control was achieved in the same group as well as the demonstration of the first p-n junction based on heterostructured nanowhiskers [100].

The growth of ZnO nanowires via the VLS mechanism was developed gradually from 2000 with several important structural control capabilities on the orientation, position, and dimension of the nanowires [10, 101–103]. In a typical VLS growth process developed by Yang et al. [103], single crystalline silicon or sapphire wafer is used as substrate for the nanowire growth. The substrate is coated with a thin Au film. Equal amounts of ZnO powder and graphite powder are ground together and used as source material. The substrate and the source powder are placed in a quartz tube furnace connected with argon gas flow. The substrate is placed downstream of the argon flow. The source and the substrate are heated to over 800 °C at which the source powder vaporizes. The zinc and oxygen vapor are brought to the substrate by the argon flow. The Au film on the substrate melts and breaks up into discrete liquid particles. When zinc and oxygen in the liquid Au particles saturate, they solidify and grow into the nanowires. In 2003, Vayssieres developed the growth of ZnO nanorods and nanowires from aqueous solution [104]. In addition, other techniques, such as metal-organic chemical vapor deposition (MOCVD) [105], pulsed laser deposition (PLD) [106], and epitaxial electrodepo-

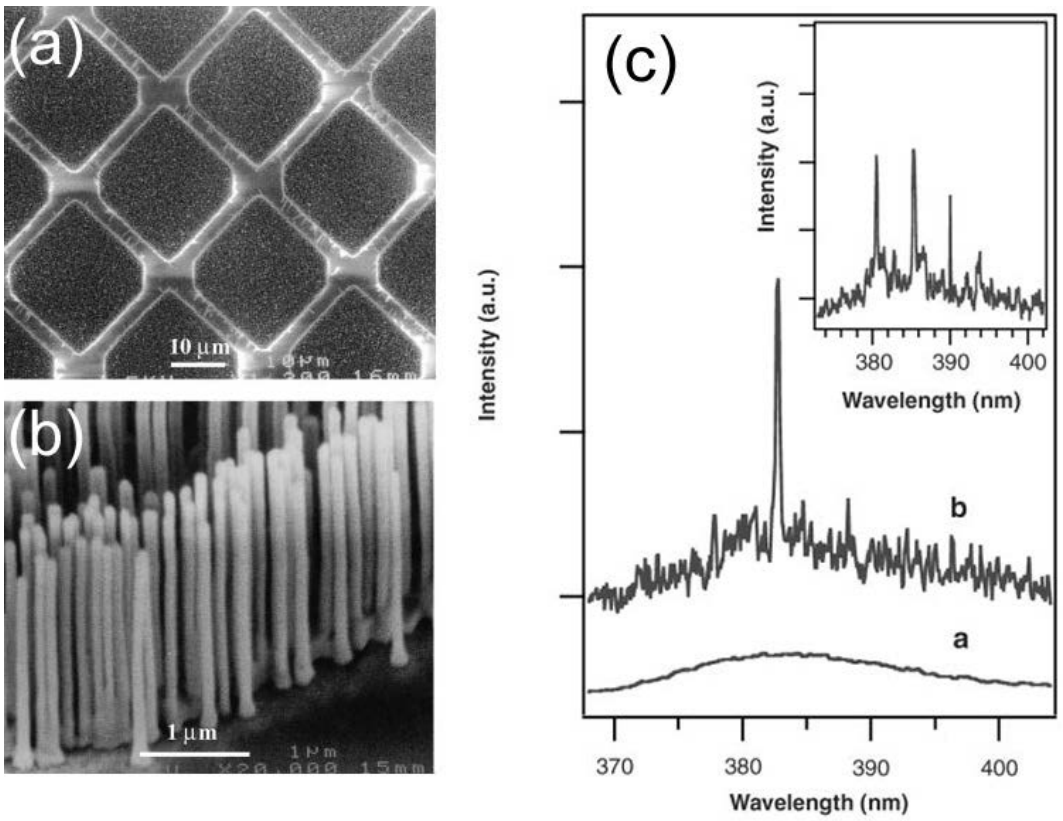

Figure 3.4: (a) and (b): SEM images of ZnO nanowire arrays grown on sapphire substrate by vapor phase transport method. (c) Emission spectra from nanowire arrays below (line a) and above (line b and inset) the lasing threshold. The pump powers for these spectra are 20, 100, and 150 kW/cm^2, respectively. The images are from Ref. [10].

sition [107], have also been developed for successful growth of highly oriented arrays of ZnO nanowires and nanorods.

The properties of ZnO nanowires and their potential applications have been intensively studied and explored since their successful growth. In 2001, Huang et al. [10] reported the lasing in VLS-grown oriented ZnO nanowires at room temperature. The nanowires were vertically grown on sapphire substrate, as shown in the scanning electron microscope (SEM) images shown in Fig. 3.4 (a) and (b). The nanowires had diameters varying from 20 to 150 nm and lengths up to 10 μm. They were optically pumped by the fourth harmonic of a Nd:YAG laser (266 nm, 3 ns pulse width) with an incidence angle 10° to the symmetry axis of the nanowires. Light emission was collected in the direction along their symmetry axis. When the excitation intensity exceeded a threshold ~ 40 kW/cm^2, surface-emitting lasing action was observed at 385 nm, with an emission linewidth less than 0.3 nm (Fig. 3.4(c)). In this process, the single-crystalline, well-faceted nanowires were thought to act as natural resonance cavities for the lasing.

Recently, ZL. Wang's group reported a series of works about the fabrication of nanogenerators from ZnO nanowires using their piezoelectric effect [13, 108–110]. In these works, ZnO nanowires were transferred to a flexible substrate to form horizontally aligned arrays. Then, Au parallel stripes were deposited to connect all of the nanowires (Figure 3.5). By introducing a mechanical deformation of the device, a macroscopic piezoelectric potential can be gener-

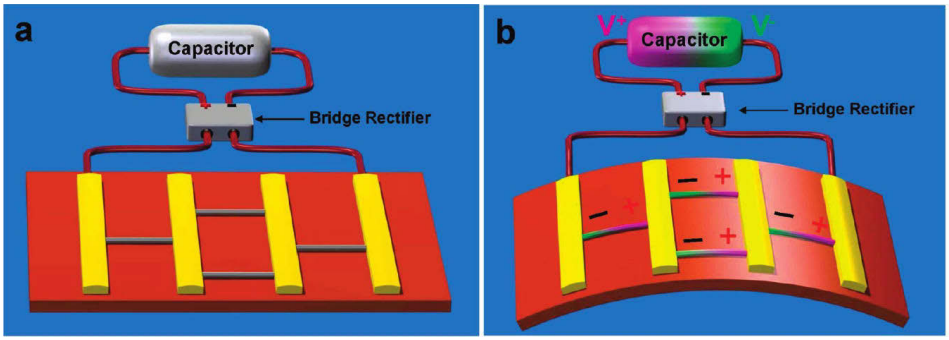

Figure 3.5: (a) Schematic diagram of a ZnO nano-piezogenerator without mechanical deformation. (b) Output generation when mechanical deformation is induced, where the "±" signs indicate the polarity of the local piezoelectric potential created in the nanowires. The images are from Ref. [108].

ated. Using a single layer of the nanowire piezogenerator structure, an open-circuit voltage of up to 2.03 V and a peak output power density of 11 mW/cm^3 have been achieved [108].

3.4 Colloidal semiconductor quantum dots

3.4.1 Synthesis

The research on colloidal semiconductor quantum dots (QDs) started from several pioneering works in the early 1980s [111–114]. The used synthesis methods were mostly based on traditional colloidal chemistry, such as arrested precipitation [111], reverse micelle [113], etc. The quality of the prepared QDs was generally very low while the particle size distribution was quite large.

The first major breakthrough in the preparation of high quality semiconductor QDs is the invention of the organometallic approach in coordinating solvents for the synthesis of cadmium chalcogenide QDs by Steigerwald et al. in 1990 [115], which was further developed to a practical level by Murray and co-workers in 1993 [44]. The synthesis begins with a rapid injection of organometallic reagents into a hot coordinating solvent to realize temporally separated nucleation of the precursor monomers and the growth of the formed nuclei. Organometallic compounds, such as $Cd(CH_3)_2$, $Zn(CH_3)_2$, were usually used as cation precursors. Trioctylphosphine (TOP), tributylphosphine (TBP), and trioctylphosphine oxide (TOPO) were used as solvents. The synthesis has to be carried out in non-aqueous and air-free environments since the precursors are extremely reactive. High reaction temperatures, typically between 150 and 400 °C, are also required. The prepared QDs are soluble in non-polar organic solvents, and are highly crystalline, due to the high reaction temperatures [44, 116].

In addition to the crystalline quality, control of the particle size distribution is another important target in QD synthesis, which is essential for research on the size-dependent properties of semiconductor QDs. Peng et al. studied the QD growth kinetics in the organometallic approaches in 1998 [68]. It was found that in the early stage of growth, wherein the monomer concentration in the reaction system is high, the QDs grow by incorporation of monomers while the size distribution quickly narrows, i.e. a size focusing process. When the monomers

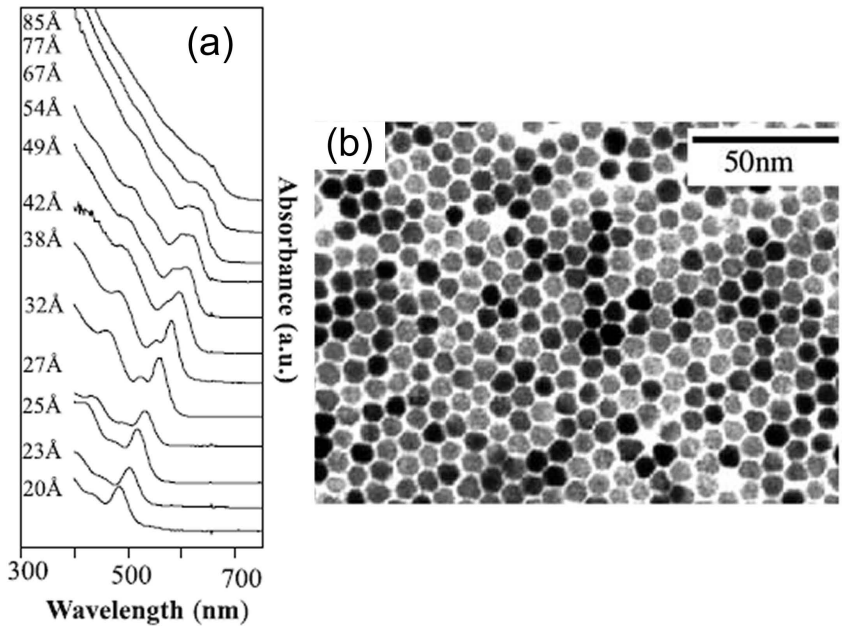

Figure 3.6: UV-Vis absorption spectra (a) and transmission electron microscopy (TEM) image (b) of the as-prepared CdSe QDs synthesized through organometallic approaches [116].

in solution are nearly exhausted, the QD growth initiates an Ostwald ripening process, in which smaller particles dissolve gradually into the solution while the larger ones continue to grow. Thus the QD sizes disperse gradually in this process, referred to as a size-defocusing process. Through control of the precursor concentrations and experimental conditions, the size-defocusing process can be avoided before reaching the desired QD sizes, thus yielding a narrow size distribution [68].

Figure 3.6 shows typical absorption spectra and a transmission electron microscopy (TEM) image of CdSe QDs produced by Peng et al. [116]. The absorption peaks are very sharp, indicating a narrow size distribution (reported to be 5–10% for the standard deviation of the particle sizes relative to the mean particle size) which can also be seen in the TEM characterization.

However, the organometallic precursors used in synthesis, such as $Cd(CH_3)_2$, are extremely toxic. To solve this problem, In 2001, Peng et al. proposed a so-called alternative synthesis route [73,117]. Low-toxic precursors, such as metal oxides, were developed. In addition to the traditional TOPO, fatty acids and amines can be used as ligands in the alternative route [72,73]. These chemicals are air-stable. Thus, the synthesis can be performed in open air. CdSe QDs prepared by this alternative route are comparable in crystallinity and size distribution to those by traditional organometallic approaches [72].

Later, Peng's group introduced the synthesis of CdS QD in non-coordinating solvents [71, 118, 119]. CdO and elemental sulfur were used as precursors while 1-octadecene (ODE) as non-coordinating solvent. Oleic acid and other fatty acids were chosen as the ligands. The key advantage of non-coordinating solvents is that the reactivity of the precursors can be tuned by varying the ligand concentrations in the solvents [71], which thus provides a better control on the particle growth. This simple and also much environmentally friendly synthesis yielded CdS nanocrystals of extremely high quality [71]. It was afterwards successfully applied to QD

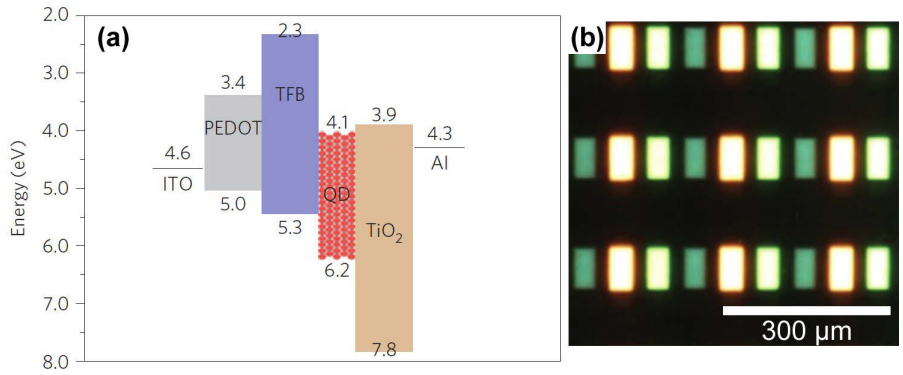

Figure 3.7: (a) Energy band diagram of the QD-LEDs. (b) Optical image of simultaneous red-green-blue (RGB) electroluminescence emission from all pixels of the QD-LEDs fabricated with differently sized QDs. The images are from Ref. [18].

synthesis of other semiconductor materials, like CdSe [120,121], CdTe [119,122], ZnSe [123], PbS [124], and some III-V materials [118]. Due to its simplicity, safety and high reproducibility, this alternative route in non-coordinating solvents has been developed to be the most used method today for preparation of colloidal semiconductor QDs.

As mentioned above, semiconductor QDs prepared from the organometallic approaches and the subsequent alternative routes are capped with hydrophobic ligands and only soluble in non-polar organic solvents. Water solubility of QDs is required for some applications such as biological analysis [125–127]. In addition, QDs capped with hydrophilic bifunctional molecules are also very interesting for conjugation with other materials to produce functional hybrid devices.

Water solubility of the QDs synthesized in organic phase can be achieved by a surface ligand exchange process, using water-soluble bifunctional molecules to replace the original hydrophobic ligands. The commonly used water-soluble molecules for ligand exchange are mercaptocarboxylic acids with different alkyl chain lengths (HS-$(CH_2)_n$-COOH, n = 1–15) with their thiol groups bound onto the surface cation of the QDs [128, 129]. However, the transfer of QDs from organic phase to aqueous phase generally results in significant reduction in their quantum efficiency and chemical stability due to the degradation of their surface passivation [130–135].

In parallel to the organic phase synthesis, QD synthesis in aqueous phase was also developed. In general, QDs synthesized in water possess a relatively low quality and a broad size distribution, mainly due to the relative low boiling point of water that confines the synthesis temperature. First steps towards a successful alternative to the organometallically synthesized QDs were done by NozikÂŠs [136] and later by Weller [75] in their preparation of CdTe QDs. Short-chain thiols were chosen as stabilizers in these works. Their methods were subsequently adapted for synthesis of other II-VI semiconductor QDs, such as CdS [137], CdSe [50, 76], CdTe [138, 139], HgTe [140], and ZnSe [141], which represent useful alternatives to the high-temperature organic phase methods.

3.4.2 Applications

The luminescence properties of semiconductor QDs, like high quantum yields, narrow spectral widths, and size-tunable colors, are very interesting for applications in light-emitting devices. The Alivisatos group reported the first QD-based light-emitting diodes (LEDs) in 1994 [142]. A CdSe QD film and a layer of semiconducting polymer *p*-paraphenylene vinylene (PPV) were used as emitting medium. Light emission arised from the recombination of holes injected into the polymer layer with electrons injected into the QD film with a low operating voltage of 4 V. The emission color can be varied from red to yellow by changing the QD size.

In 2011, Samsung scientists reported their full-color quantum dot displays with high brightness [18]. They developed a new transfer printing technique that allows spatially patterning differently sized QDs onto the pixelated display panel. Figure 3.7(a) schematically shows a schematic diagram of the structure and the energy band alignment of their QD-LEDs displays. TiO_2 and a polymer TFB are used as electron transport layer (ETL) and hole transport layer (HTL). Different core/shell QDs were used for red (CdSe/CdS/ZnS), green (CdSeS/ZnS), and blue (CdS/ZnS) emitting pixels. Figure 3.7(b) shows a picture of the simultaneous RGB electroluminescence emission of QDs from the pixelated area during operation. The maximum brightnesses are 16380, 6425 and 423 cd m^{-2} for red (615 nm), green (530 nm), and blue (480 nm) pixels, respectively.

3.5 Hybrid structures of ZnO nanowires and semiconductor quantum dots

Hybrid nanomaterials have been widely studied for new-generation photovoltaic devices. Compared to conventional bulk counterparts, they possess a much larger surface-to-volume ratio, promising more effective surface areas available for adsorption of photo-sensitizers and thus higher conversion efficiencies.

In 2007, Leschkies et al. reported photovoltaic devices made from ZnO nanowires functionalized with colloidal CdSe QDs [15]. Figure 3.8(a) shows the schematic of the QD sensitized solar cells (QDSSCs). CdSe QDs are attached on the surface of ZnO nanowire grown vertically on a fluorine-doped tin oxide conducting substrate. The QDs act as photo-sensitizers. When electrons in the QDs are excited by sunlight, they will transfer into the ZnO nanowires due to their low-lying conduction band. They are further transported to the nanowire substrate which acts as photoanode. The holes left in the QDs can transfer into the filled liquid electrolyte containing triiodide/iodide (I_3^-/I^-) couples by a redox process. These holes are collected by the top glass substrate coated with a 10 nm Pt layer, acting as photocathode.

The CdSe QDs they used were synthesized in organic phase and capped with TOPO molecules. A ligand exchange with hydrophilic 3-mercaptopropionic acids (MPA) was performed afterwards to transfer the QDs into the water phase. The ZnO nanowires were grown by a hydrothermal method. The QDs were attached onto the nanowires by the carboxylic groups of the MPA molecules bound to the zinc ions on the nanowire surfaces.

Figure 3.8(b) shows the wavelength dependence of the incident photon-to-current conversion efficiency (IPCE) for their solar cells using bare and QD sensitized ZnO nanowires, respec-

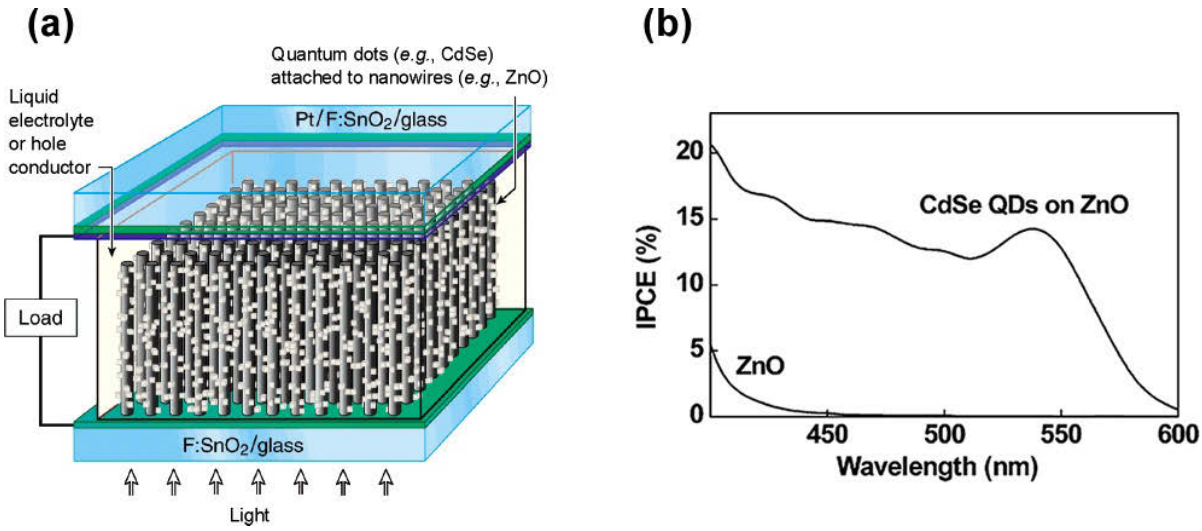

Figure 3.8: (a) Schematic of the quantum-dot-sensitized solar cell. (b) IPCE spectrum of the quantum-dot-sensitized and unsensitized ZnO nanowire solar cell. The images are from Ref. [15].

tively. The IPCE for the QDSSCs significantly increased in the absorption region of the QDs. The internal quantum efficiencies were reported to be 50-60%. The open-circuit voltages under illumination of 100 mW/cm^2 simulated sunlight was 0.5–0.6 V with short-circuit current ranging from 1 to 2 mA/cm^2 [15].

Chapter 4

Sample Preparation and Experimental Methods

In this chapter, the preparation of ZnO nanowire samples and the experimental techniques and setups used in this work are presented. The first section introduces the growth of the ZnO nanowire samples by hydrothermal method and a thermal chemical vapor deposition method. In the second section, the experimental techniques and the employed setups for synthesis and investigation of colloidal semiconductor quantum dots are presented. The photoconductivity and photoluminescence measurement setups are described in the last two parts of this chapter.

4.1 Growth of ZnO nanowire samples

4.1.1 Growth by hydrothermal method

The ZnO nanowires used for building the nanowire/quantum-dot hybrid structures in Chapter 6 are grown by Dr. A. Dev in the group of Prof. J. Gutowski at the Institute of Solid State Physics, Universität Bremen. The nanowires are grown by a hydrothermal method on glass sheets coated with a conductive fluorine-doped tin oxide (FTO) film.

The FTO-coated glass sheets are purchased from Solaronix. The chemicals used for growth are purchased from Sigma-Aldrich with analytical or puriss grades if available. First, ZnO seeds are produced on the glass substrates. 1.3 g zinc acetate dihydrate is dissolved in 10 ml ethanol. Diethanolamine is added dropwise under stirring until the solution becomes transparent. The obtained solution is spin-coated onto the FTO glass. Then, the coated glass sheets are annealed in air at 500 °C for 1 hour. This coating-annealing process is repeated twice to obtain a large amount of ZnO seeds on the glass. 7.2 g potassium hydroxide and 4.5 g zinc nitrate hexahydrate are each dissolved in 30 ml deionized water, and then mixed together. The glass sheets with ZnO seeds onside are inserted in this mixed solution. This reaction system is heated up to 80 °C and kept at this temperature for 3 hours. After that, nanowire arrays are obtained on the FTO glass.

Figure 4.1(a) shows a scanning electron microscope (SEM) image of the prepared ZnO nanowires. The diameters of the nanowires are in the range of 50–300 nm with lengths around 1 μm. The nanowire density is estimated to be around 10^9 cm^{-2}. The nanowires show approxi-

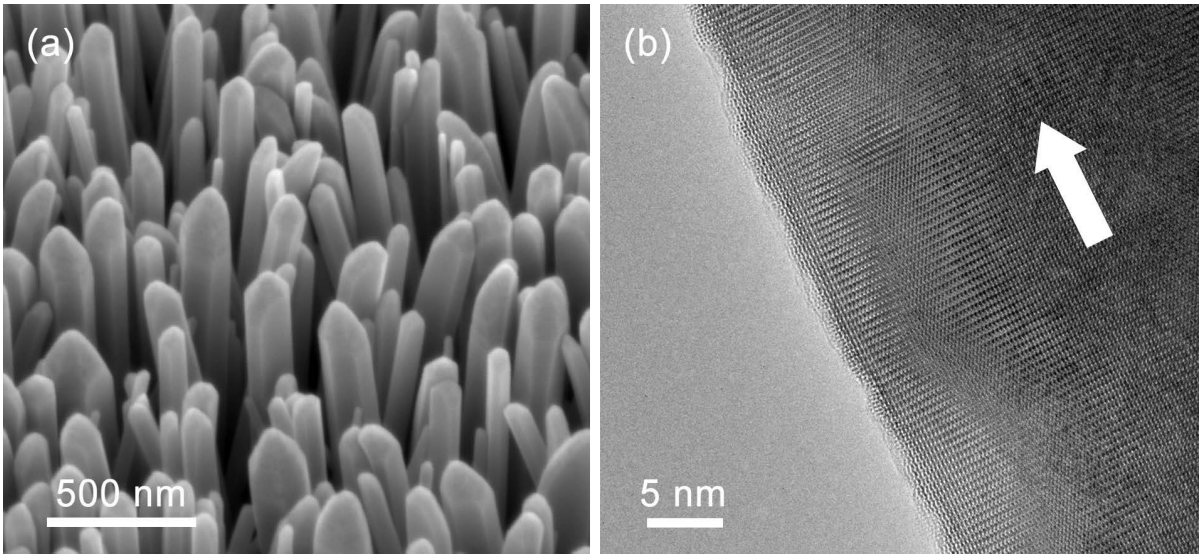

Figure 4.1: (a) SEM image of the prepared ZnO nanowire arrays. (b) High-resolution TEM image of a ZnO nanowire measured by K. Frank in the group of Prof. A. Rosenauer at the Institute of Solid State Physics, Universität Bremen. The white arrow indicates the growth direction.

mately hexagonal cross sections, illustrating their ⟨0001⟩ growth direction, as indicated in the high-resolution transmission electron microscopy (TEM) image of the nanowire shown in Fig. 4.1(b).

4.1.2 Growth by chemical vapor deposition method

The ZnO nanowire samples used for the studies of the excitation intensity dependence of the photoluminescence properties of ZnO were grown by the chemical vapor deposition (CVD) method, which are based on the transport of Zn and O vapor onto a substrate where they react to form ZnO nanostructures. Two kinds of nanowires were prepared based on different growth mechanisms, namely the vapor-liquid-solid (VLS) process and the direct vapor-solid (VS) process.

The VLS growth of ZnO nanowires was performed in the group of Prof. C. Ronning at the Institute of Solid State Physics, Universität Jena [143]. The growth is carried out in a horizontal tube furnace with several separate heating zones. ZnO powder (99.9% purity) is put in an alumina boat in the middle of the furnace and heated up at a rate of 200 K/h. At 600 °C, an argon flow of 50 sccm is introduced to the tube at a pressure of 100 mbar, which is pumped out from the other end. A p-Si(100) chip sputter-coated with 5 nm Au film is used as substrate and placed in an alumina boat at a downstream position. After reaching a temperature of 1350 °C, the source powder vaporizes. The Zn and O vapors are carried by the argon flow to the substrate which is heated to ∼ 1000 °C. At this temperature, the Au layer melts and turns into discrete Au droplets. These Au droplets act as catalysts for the nanowire growth. The Zn vapor forms a liquid alloy with the Au droplets, and nanowire growth begins after the supersaturation of the alloy by reaction with the O vapor, corresponding to a vapor-liquid-solid (VLS) growth process. The diameters of the resulting nanowire are thus defined by the sizes

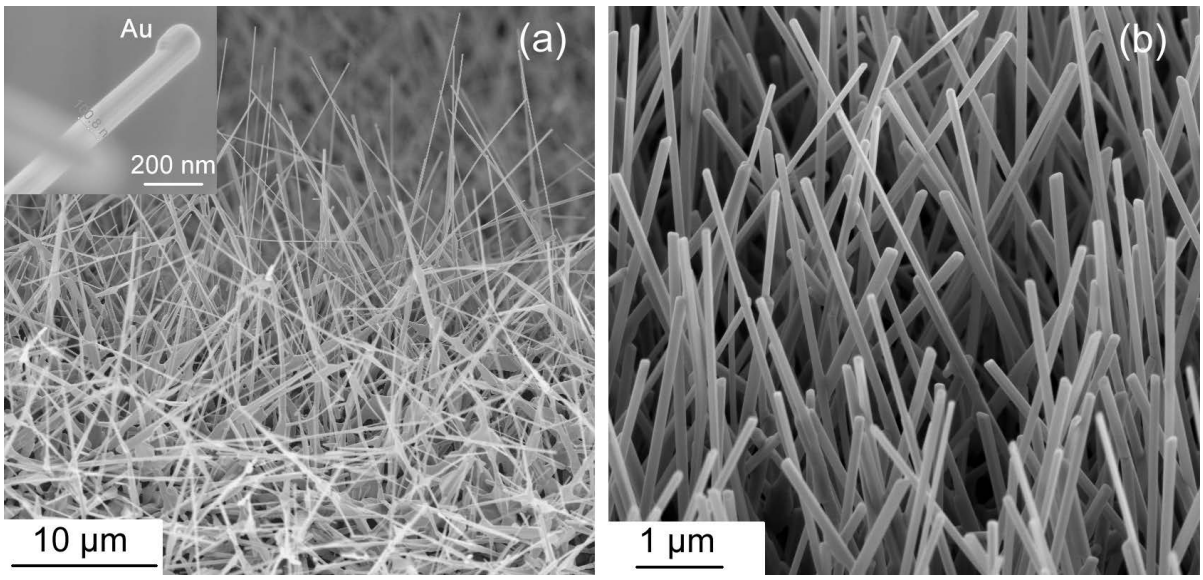

Figure 4.2: SEM images of ZnO nanowires grown by thermal CVD methods based on a Au catalyzed vapor-liquid-solid (VLS) process (a) and a catalyst-free vapor-solid (VS) process (b).

of the Au droplets. The growth lasts for about 90 minutes for the preparation of the nanowires used in this work.

The VS growth of ZnO nanowires was done by Andreas Menzel in the group of Prof. M. Zacharias at the "Institut für Mikrosystemtechnik (IMTEK)", Universität Freiburg [144]. The growth was performed at relatively low temperature. In this case, 1:1 weight mixture of ZnO and graphite powders is used as source material in which the graphite can lower the decomposition temperature of ZnO significantly. A flow of 30 sccm Ar and 1.5 sccm O_2 mixture is used as carrying gas. Silicon wafers coated with 5 nm Au film are used as substrates. The source and substrate temperatures for the growth are 950 °C and 750 °C, respectively. At this temperature, the Zn and O vapors react directly at the substrate through a vapor-solid (VS) process without the catalysis of Au. The growth lasts for 40 minutes.

Figure 4.2 shows SEM images of the ZnO nanowires grown by those two methods. The nanowires (a) are grown based on the former Au-catalyzed VLS process and have diameters around 100 nm and length in the range of 10–100 µm. However, at the bottom of the nanowires, nanosheets are formed. The inset shows a image of a single nanowire in which the Au particle can be seen at the end of the nanowire. The nanowires grown by the latter catalyst-free VS process are shown in Fig. 4.2(b) and have much shorter lengths of $\sim$ 4.9 µm. The average diameter of the nanowires is around 95 nm.

4.2 Experimental techniques for semiconductor quantum dots

4.2.1 QD synthesis setup

Figure 4.3 shows a schematic of the setup used for the synthesis of colloidal semiconductor quantum dots (QDs) in aqueous phase. The solution of the cation precursor and the surfactant

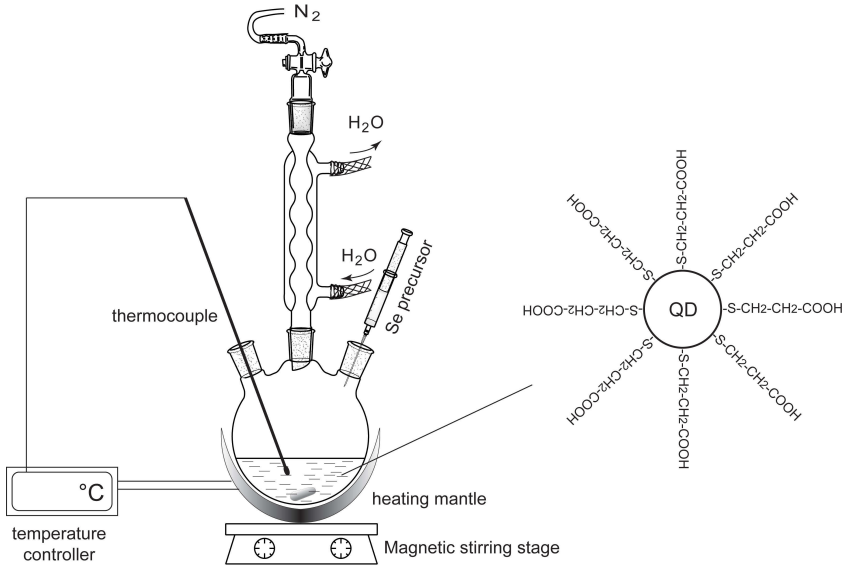

Figure 4.3: Schematic of the experimental setup for the synthesis of CdSe QDs. The synthesis is performed under the protection of nitrogen.

are placed in a 250 ml round-bottom flask with 3 necks. One stirring bar is put inside the flask. The two side necks are sealed with rubber stoppers. A thermocouple is inserted into the solution through one side neck and connected to a temperature controller. The center opening is connected with a condenser. The condenser is further connected on its top end with a balloon filled with nitrogen. The flask can be heated with a heating mantle over an magnetic stirring stage. For the QD synthesis, the reaction solution is first bubbled with nitrogen for 1 hour using a needle inserted into the solution through a side opening of the flask. Afterwards, the anion precursor solution is quickly injected with a syringe under strong stirring. The reaction solution is heated up and the temperature can be controlled by adjusting the power of the heating mantle with the temperature controller. During the refluxing process, the condenser is cooled with water. The synthesis is performed under a hood.

4.2.2 Purification of as-prepared quantum dots

For further use, the prepared QDs normally need to be purified from the crude solution to remove the residual reagent chemicals and byproducts. To do this, 2-propanol is added dropwise into the crude QD solution under mild stirring until turbidity appears. The solution is further stirred for 1 h. Then the QDs are isolated by centrifugation at 3500 rpm for 10 min. The QDs precipitated at the bottom are washed with ethanol twice. Afterwards, the QD precipitation is dried under vacuum for 1 h and redispersed in water. The pH value can be adjusted by tetraethylammonium hydroxide. The obtained QD dispersion is stored in darkness.

4.2.3 Measurements of the absorption and photoluminescence spectra

The absorption spectra of the QDs are measured using a Jasco V-670 spectrometer instrument. The QD water solution and pure water are filled in two identical cuvettes, respectively. The

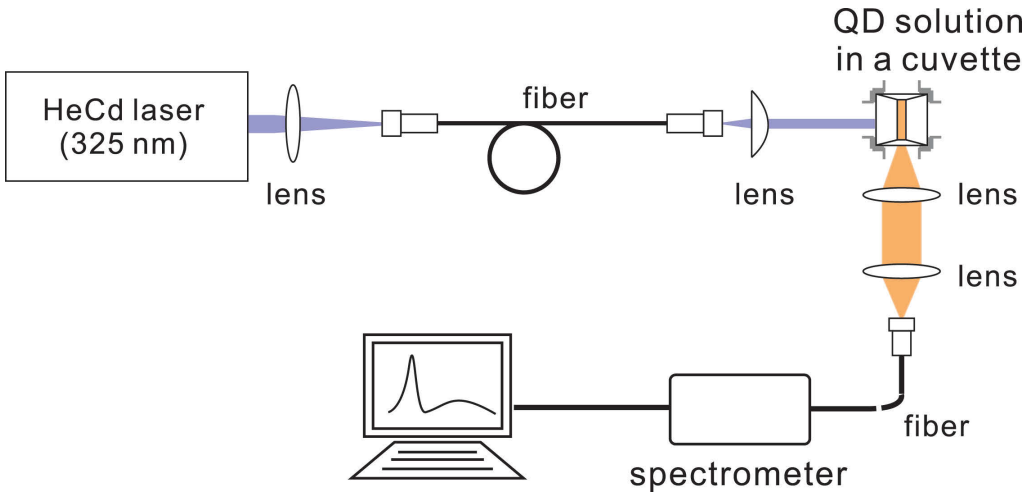

Figure 4.4: Schematic of the setup used for measuring the photoluminescence spectra of semiconductor QDs in solution phase.

transmission through them is recorded and the absorption of the QDs is calculated automatically. The length of the effective optical path of the cuvette for measurement is 1 cm.

Figure 4.4 is a schematic of the setup used for measuring the photoluminescence (PL) spectra of QDs in solution phase. The QD solution is filled into a cuvette with narrow cross section (2 mm in thickness), which is placed on a positioning stage. A HeCd laser operating at 325 nm is used as excitation source. The laser light is guided to the measurement setup by a optical fiber. It is collimated with a UV lens with a beam diameter of 3 mm. The laser light excites the QD solution from a side of the cuvette. The luminescence of the QDs is collected by a lens and coupled into a fiber with a second lens. The spectra are recorded using an Avantes 2048TEC spectrometer with measurement range of 200–1100 nm and resolution of 2.4 nm.

4.2.4 Calculation of the quantum dot size and molar concentration

The band gap of semiconductor QDs is size-dependent. From the absorption measurements, the average particle size of a given QD ensemble can be calculated. For CdSe QDs, the magnitude of the average particle diameter D (in nanometer) of a QD ensemble is related to the magnitude of their first absorption peak wavelength λ (in nanometer) by an empirical equation [145]

$$D = (1.6122 \times 10^{-9})\lambda^4 - (2.6575 \times 10^{-6})\lambda^3 + (1.6242 \times 10^{-3})\lambda^2 - 0.4277\lambda + 41.57 \quad (4.1)$$

The molar concentration of QDs in a solution can also be extracted from the absorption measurements [145]. For this purpose, the absorbance A at the first absorption peak position of the QD sample is calibrated as

$$A_{cali} = A\frac{W}{W_{std}} \quad (4.2)$$

where W is the half width (in nanometer) at half maximum (HWHM) of the first absorption peak on its long wavelength side. W_{std} is the value of W for a standard QD sample used in the literature corresponding to the empirical equation (Equ. 4.1), which is 14 nm for CdSe QDs.

The absorbance at the first absorption peak of CdSe QDs is given by [145]

$$A_{cali} = \epsilon C L \tag{4.3}$$

where ϵ is the extinction coefficient per mole of the QDs (l cm^{-1} mol^{-1}) at its first absorption peak position. C is the desired molar concentration (mol l^{-1}) of the QDs. L is the effective path length (cm) of the radiation beam for recording the absorption spectra, which is, in the present case, 1 cm. The value of ϵ dependent on the QD size D (nm) can be calculated by an empirical equation [145]

$$\epsilon = 5857 D^{2.65} \tag{4.4}$$

Using Equ. 4.1-4.4, the particle size and molar concentration of CdSe QDs in solution phase can be calculated.

4.2.5 Measurements of the photoluminescence quantum yield

The photoluminescence quantum yield (QY) of the CdSe QDs is determined using the dye Rhodamine 6G dissolved in ethanol as reference. Six solution samples with different concentrations are prepared for the dye and the CdSe QDs, respectively. The concentrations of these sample are at such levels that their absorbance at the excitation wavelength for the photoluminescence measurements (in this case 325 nm) is below 0.1 to avoid significant reabsorption effect. The absorption and photoluminescence spectra of these samples are measured. A HeCd laser operating at 325 nm is used as excitation source. The integrated photoluminescence of a dye or a QD sample is linearly related to its absorbance at the excitation wavelength. The slopes of the dependence are calculated for the dye and the QD samples, and referred to as m_{ref} and m_{QD}, respectively. The QY of the CdSe QDs is calculated by:

$$\Phi_{QD} = \Phi_{ref} \frac{m_{QD}}{m_{ref}} \frac{\eta_{water}^2}{\eta_{ethanol}^2} \tag{4.5}$$

where η is the refractive index of the solvent ($\eta_{water} \approx 1.335$ and $\eta_{ethanol} \approx 1.362$) [50]. Φ_{ref} is the QY of Rhodamine 6G, which is known to be $\sim 95\%$ at a concentration of 10^{-7} M [146].

4.3 Photoconductivity measurements of ZnO-nanowire/CdSe-quantum-dot hybrid structures

Figure 4.5 presents a schematic setup for the photoconductivity measurements of the ZnO-nanowire/CdSe-QD (NW/QD) hybrid samples. The sample is covered with a piece of FTO glass sheet and mounted in a small vacuum chamber. The FTO glass forms a top electric contact with the tips of ZnO nanowires. The contact area is around 0.4 cm^2. The chamber is equipped with a quartz window and can be pumped to high vacuum (10^{-7} mbar) and filled with gas. An argon laser emitting at 458 nm (2.71 eV) is used to illuminate the sample vertically through the top FTO glass. The laser has a photon energy below the band gap of ZnO ($\sim$ 3.37 eV at room temperature [19]). Therefore, only CdSe QDs in the hybrid structures can be excited. The laser spot on the sample has a diameter of 1.5 cm with a laser intensity of 1.0

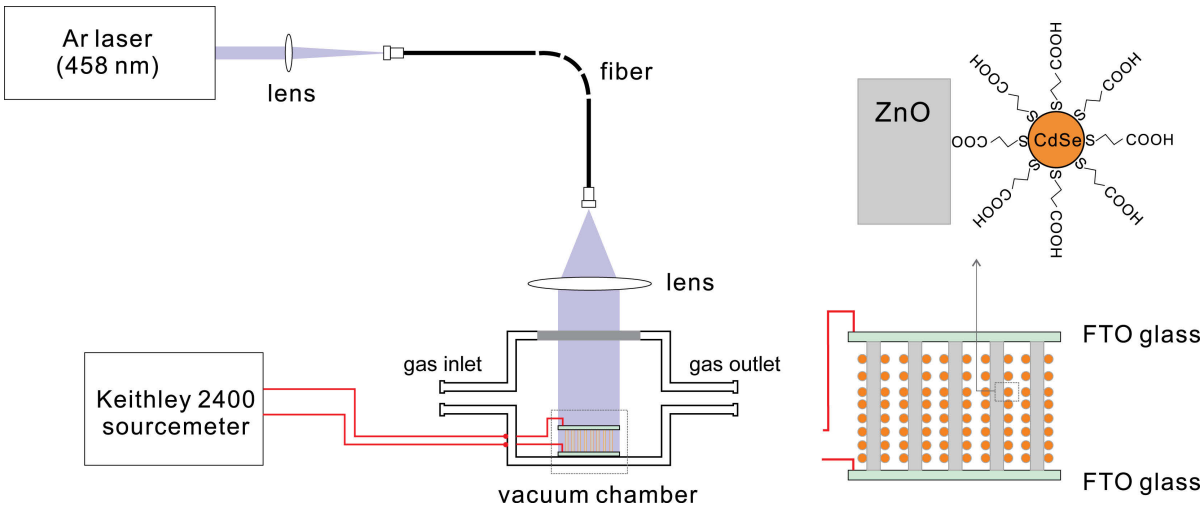

Figure 4.5: Schematic representation of the experimental setup used for the photoconductivity measurements.

mW cm^{-2}. The top FTO glass and the FTO glass substrate of the nanowires are connected to two electrode arms in the chamber, respectively. These arms are connected with a Keithley 2400 SourceMeter to form a circuit. The SourceMeter imposes a constant bias voltage (1.0 V) between the top glass sheet and the substrate of ZnO nanowires, and measures the electric current through the nanowires. Thus, the photoresponse of the conductivity of the QD decorated nanowires is measured.

The photoresponse of the conductivity of the NW/QD hybrid samples is investigated in air, vacuum (10^{-6} mbar), dry oxygen, and constant flows of nitrogen and argon, respectively. For the measurements in oxygen, the chamber is first pumped to vacuum ($\sim 10^{-6}$ mbar) for 10 min and then connected with a balloon filled with highly pure dry oxygen gas (purity of 99.9995%). The pressure inside the chamber is $\sim$ 1.1 bar. For the measurements in the nitrogen (purity of 99.999%) and argon (purity of 99.9999%) environments, the gas flow is introduced into the chamber through one channel tube with a constant speed (40 sccm). Before the measurements, the gas flow is applied for 15 minutes in advance to replace the air in the chamber. After every photoresponse measurements, the chamber is left in darkness overnight to allow the sample to return back to the original state. All measurements are performed at room temperature.

4.4 Photoluminescence measurement setup

This section introduces the experimental setups used in this work for standard photoluminescence measurements at room and low temperatures and the investigation of the excitation intensity dependence of the photoluminescence properties of ZnO.

4.4.1 The standard photoluminescence setup

Figure 4.6 shows a schematic of the experimental setup used for the standard photoluminescence measurements at room and low temperatures. The sample is placed in a cryostat and

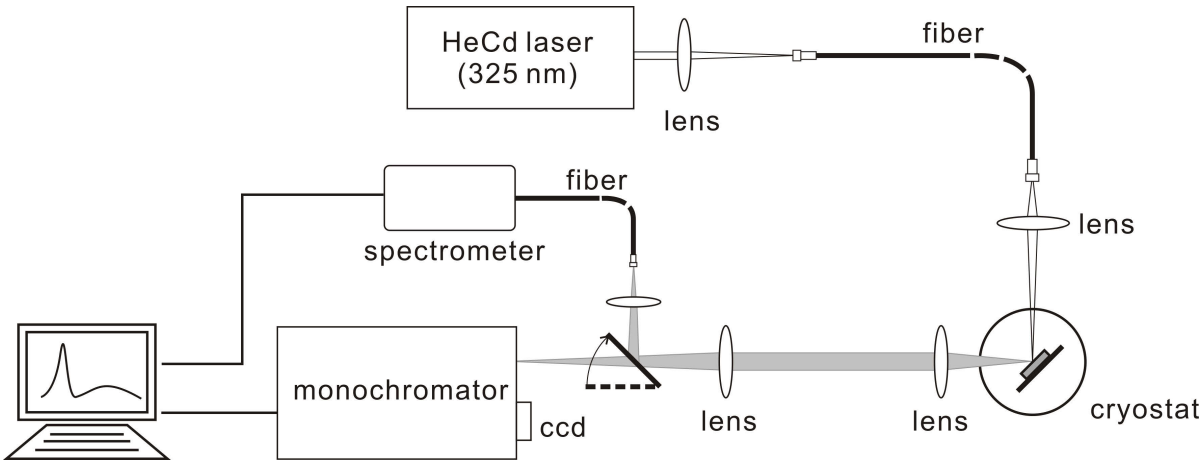

Figure 4.6: Schematic of the experimental setup for general and high resolution photoluminescence measurements.

mounted on a copper sample finger which is tightly attached to a cooling tube. This tube is connected to an external helium gas condensing and pumping machine, which can cool the cryostat to 10 K.

For photoluminescence measurements, a helium-cadmium (HeCd) laser operating at 325 nm (3.8 eV) is used as excitation source. The photon energy of the laser is well above the band gap of ZnO which is around 3.437 eV at $T = 1.6$ K. Thus ZnO samples can be excited non-resonantly. The laser light is coupled into a fiber and directed towards the top of the cryostat. It is focused with a UV lens onto the sample at an angle of about 45 °. The laser spot size on the sample is 1 mm with a power intensity of ~ 0.1 W/cm^2.

The photoluminescence from the sample is collected and focused with two extra UV lenses. The light is coupled into a monochromator or a fiber spectrometer with a turning reflector, for high resolution and general photoluminescence measurements, respectively. The monochromator (Spex 1401) has two diffraction gratings with 1200 lines/mm and a spectral resolution of $\sim$ 0.3 meV. The spectra are recorded using an Ames LARRY 2048 linear CCD camera. An Avantes 2048TEC spectrometer (measurement range of 200–1100 nm and resolution of 2.4 nm) is used for the general photoluminescence measurements, which is equipped with a thermoelectric cooling element on its detector which can cool it to $T = 5$ °C in order to reduce noise.

4.4.2 The excitation-intensity-dependent photoluminescence setup

Figure 4.7 shows the measurement setup for investigating the excitation intensity dependence of the photoluminescence properties of ZnO. The sample is placed in a temperature variable cryostat which is mounted on a positioning stage. For low temperature measurements, the cryostat is cooled with liquid nitrogen to $T \approx 70$ K.

The 325 nm HeCd laser is used as excitation source with a maximum output power of $\sim$ 50 mW. The laser light is focused with a UV lens (L1) perpendicularly on the sample surface. The laser intensity can be adjusted with a neutral density filter (NF) and measured using a powermeter behind the lens. The luminescence of the sample is collected with the same UV

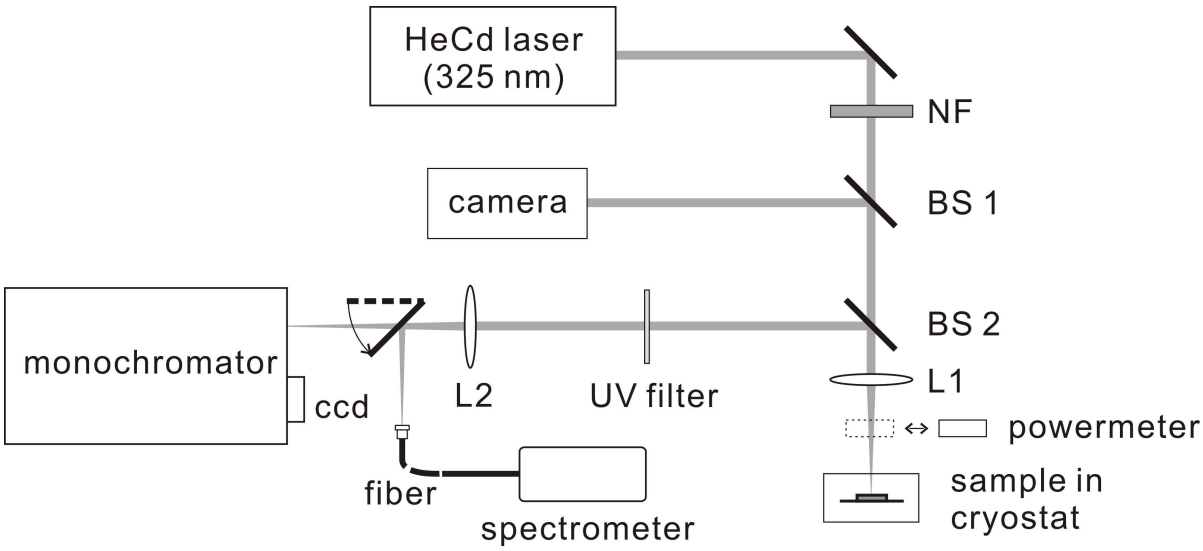

Figure 4.7: Schematic of the experimental setup for the measurements of the excitation intensity dependence of ZnO photoluminescence properties.

lens L1 and reflected by a beam splitter (BS2) to the spectrometers. The laser light reflected from the sample surface is eliminated with a UV blocking filter. For obtaining high resolution spectra, the luminescence light is focused with lens L2 into a monochromator equipped with a CCD camera. To record the general overall emission spectra, the luminescence is reflected with a turning reflector to a fiber spectrometer Avantes 2048TEC.

In order to obtain high excitation intensities, the laser line is focused onto the sample surface with a rather small spot size. To accurately determine the laser spot size, a scaling reference with a calibrated length scale is mounted together with the sample in the cryostat. The imaging of the sample is realized with a second beam splitter BS1 that reflects the light coming from the sample into a camera. Through adjusting the positioning stage of the cryostat, the sample can be properly focused to form a clear image in the camera. Then, the laser spot size is determined by calibration with the scaling reference. The spot size in the experiments is variable in the range of 4–30 μm depending on the focusing lens used.

Chapter 5

Synthesis, Optical Properties, and Chemical Stability of Colloidal CdSe Quantum Dots

Colloidal semiconductor quantum dots (QDs) are crystalline semiconductor nanoparticles with sizes typically ranging from 1 to 10 nm which are capped with organic molecules for surface passivation. They are synthesized in liquid phase by wet chemical methods and are free-standing in solutions. Colloidal semiconductor QDs have attracted intense research interests in the last two decades. The most striking property of QDs is their size-dependent band gap as a result of the strong quantum confinement effect on the motion of the charge carriers. This largely modifies their physical properties and brings in new phenomena. Synthesis of colloidal semiconductor QDs has been greatly developed since the milestone work of Murray et al. in 1993 which realized an efficient control on the crystal quality and size distribution of the dots [44]. Generally, colloidal QDs with outstanding quality are exclusively synthesized in organic solution. However, water-phase synthesis methods provide significant alternatives with special advantages like simplicity and low energy consumption [147]. Moreover, water soluble QDs capped with bifunctional ligands are of great interest for conjugation with other materials to fabricate functional hybrid nanostructures.

In this chapter the synthesis of cadmium selenide (CdSe) QDs and their optical properties will be presented. The QDs are synthesized by a wet chemical method. The synthesis procedure will be described in the first section. Then the basic optical properties and the transmission electron microscopy characterization of the prepared QDs are presented. In the third section, the evolution of the QD size and concentration during synthesis are studied, giving insight into the growth kinetics of the QDs. Afterwards, the size-dependent Stokes shift in the optical spectra of the QDs and their photoluminescence quenching in oxygen-deficient environments are investigated. Then the chemical stability of the prepared QDs against light irradiation and oxidation is studied. The last section summarizes the results obtained in this chapter.

5.1 Synthesis procedure

CdSe QDs are synthesized in aqueous phase by a wet chemical method. A short-chain thiol 3-mercaptopropionic acid (MPA) is used as surfactant. The thiol groups (-SH) of the acid molecules are bound to the cadmium ions on the QD surfaces, which passivate the surface dangling bonds. The outgoing carboxyl groups of the acid molecules make the QDs water soluble. They further provide repulsion effect and steric barriers between the dots to prevent them from aggregation and ensure a good dispersion in the solution. The experimental setup used for the synthesis is introduced in section 4.2.1.

The synthesis method is adapted from the literature [50]. A typical synthesis process of CdSe QDs is as follows. First, the selenium precursor is prepared. 20 mg selenium and 124 mg sodium sulfite (Na_2SO_3) are mixed in 25 ml deionized (DI) water. The mixture is heated to 90 °C under nitrogen until the selenium is completely dissolved. Then, the 0.01 M Na_2SeSO_3 solution is obtained. The solution is stored under nitrogen for later use.

0.064 g (0.24 mmol) of cadmium acetate dihydrate ($Cd(CH_3COO)_2{\cdot}2H_2O$) and 50.2 µl (0.58 mmol) of 3-mercaptopropionic acid (MPA) are dissolved in 48 ml DI water. The pH value is adjusted to 10.5 with a 1 M NaOH solution. The mixture is bubbled with nitrogen gas for 1 h to replace the air. Afterwards, 2.4 ml of the prepared Na_2SeSO_3 solution is swiftly injected into the mixture under strong stirring. The final molar ratio of Cd^{2+}:MPA:Se^{2-} in the reaction solution is 1:2.4:0.1. Then the system is heated to 100 °C under nitrogen atmosphere for several days until QDs with the desired size are obtained. During the synthesis, aliquots are frequently taken from the reaction solution. The absorption and photoluminescence (PL) spectra of these samples are measured with the experimental setup described in Chapter 4.

When the selenium precursor solution is injected into the reaction system, the following reactions occur immediately,

$$SeSO_3^{2-} + OH^- \rightarrow HSe^- + SO_4^{2-} \tag{5.1a}$$

$$HSe^- + OH^- \rightarrow Se^{2-} + H_2O \tag{5.1b}$$

$$Cd^{2+} + Se^{2-} \rightarrow CdSe \tag{5.1c}$$

The fast reactions generate an instantaneous supersaturation of the Cd^{2+} and Se^{2-} monomers which act as the basic building blocks for CdSe QDs. The solution releases the supersaturation through nucleation of the monomers, forming the CdSe crystal seeds. The sizes of the crystal nuclei depend on the initial concentrations of the precursor chemicals and the chemical reactivity which can be controlled by the concentration of the stabilizers [48]. Afterwards, the nuclei seeds continue to grow under heating by incorporation of the residual monomers inside the solution,

$$Cd^{2+} + Se^{2-} + (CdSe)_m \rightarrow (CdSe)_{m+1} \tag{5.2}$$

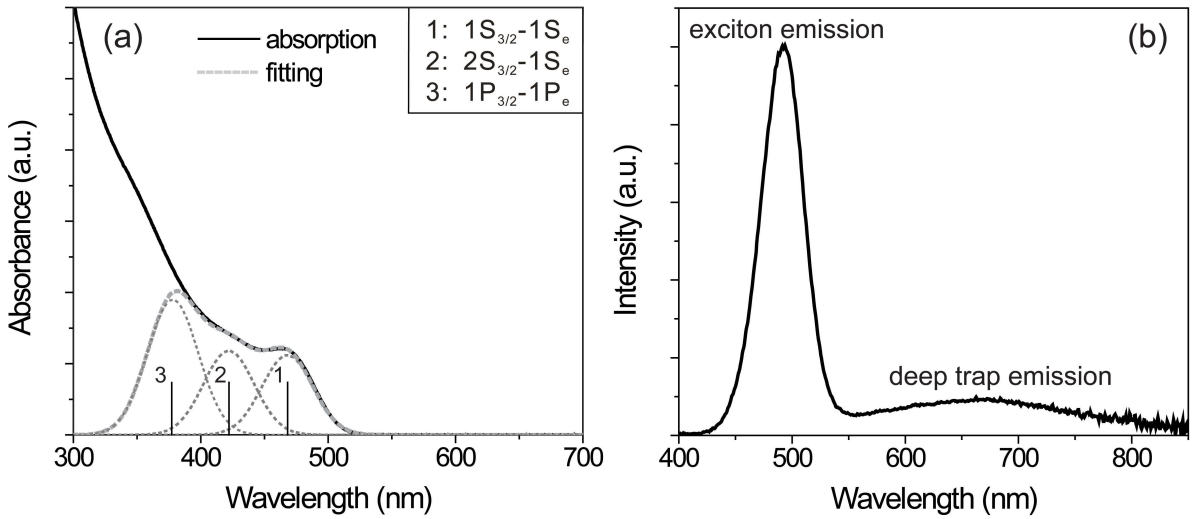

Figure 5.1: (a) Absorption spectrum of MPA-capped CdSe QDs taken after 22 hours of synthesis. The vertical bars represent the calculated spectral positions of the first three electronic transitions for the QD sample. The spectrum is fitted with three Gaussian-shaped bands (dotted curves) corresponding to these three electronic transitions. The dashed curve is the superposition of the results. (b) Photoluminescence spectrum of the same QD sample.

5.2 Basic properties of the prepared CdSe quantum dots

5.2.1 Optical properties

Fig. 5.1 shows the absorption (a) and photoluminescence (b) spectrum of a CdSe QD sample taken after 22 hours of synthesis. The absorption spectrum exhibits several weak peaks. These peaks are arising from different electronic transitions. The first absorption peak appears around 468 nm, corresponding to a band gap of 2.65 eV, which is significantly higher than the bulk band gap energy of CdSe (1.74 eV), indicating the significant band gap broadening of the QDs as a result of the quantum size effect. The band gap of the QDs is strongly dependent on their particle size. From the spectral position of the first absorption peak λ, the average QD size can be calculated by an empirical equation (Equ. 4.1) introduced in Chapter 5 to be 2.08 nm. It is about 0.37 times of the exciton Bohr radius in bulk CdSe ($a_B \approx 5.6$ nm).

Using previously developed theoretical methods (see section 2.4.1), the energies of the first several electronic transitions of the QDs can be calculated, which are marked by vertical bars in Fig. 5.1(a). Their assignments to transitions between electron and hole levels are listed in the inset. The notations for the levels are introduced in section 2.4.1. The transitions 1 and 2 are from the lowest two hole levels $1S_{3/2}$ and $2S_{3/2}$ to the ground electron level $1S_e$. Their energy difference ($\sim$ 300 meV) corresponds to the energy spacing between these two hole levels, which is 12 times larger than the thermal energy at room temperature (25 meV). The lower energy part of the absorption spectrum is fitted with three Gaussian bands corresponding to these three transitions. The same band width of 47 nm is used for the fitting. This band width is mostly due to the size distribution of the prepared QDs. The dashed line in the figure represents the superposition of the fitted bands, which shows a good agreement with the spectrum.

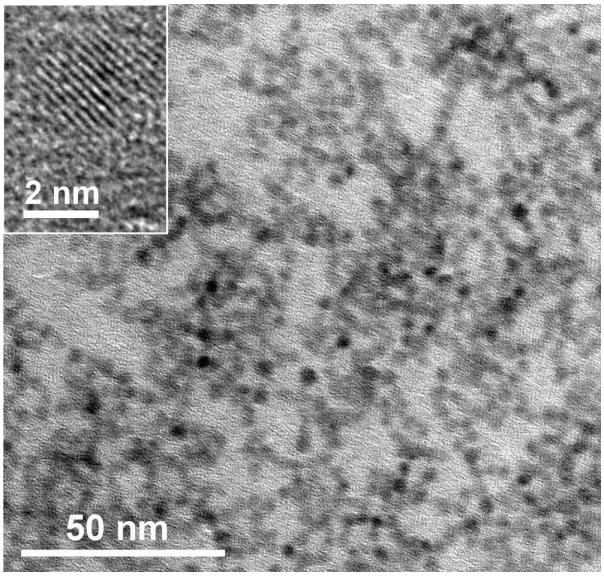

Figure 5.2: TEM image of the prepared CdSe quantum dots without post-preparative size separation. The inset is a high resolution TEM (HRTEM) image of an isolated QD. The measurements were performed by K. Frank in the group of Prof. A. Rosenauer at Universität Bremen.

The photoluminescence spectrum of the QDs has two main emission bands. The band centred around 500 nm originates from the band-edge exciton recombinations. The second wide band at longer wavelengths is related to recombinations through defect states in the band gap of the QDs. These states could be induced by surface defects or unpassivated dangling bonds of the QDs. Defects could also be formed in the crystal core of the QDs due to the low synthesis temperature in water phase. For longer synthesis times, the exciton emission would gradually increase relative to the defect emission due to the improvement of the crystal quality and the surface passivation of the QDs.

5.2.2 Structural characterization

The prepared QDs are further characterized with transmission electron microscope (TEM). For this purpose, the prepared QDs are first purified from the crude reaction solution. The purification of the QDs based on repeated precipitation-centrifugation process is described in section 4.2.2. The TEM samples are prepared by dropping the diluted aqueous solution of the QDs onto carbon-coated copper grids. Then the samples are left in air to dry naturally. The TEM measurements were performed by K. Frank in the group of Prof. A. Rosenauer at Universität Bremen using a FEI Titan microscope operating at 300 kV.

Figure 5.2 shows a TEM overview image of the CdSe QDs. The QDs seem to have a spherical shape with narrow size distribution. The dark spots in the image are probably aggregations or overlap of QDs formed during the preparation of the TEM sample. The inset is a high resolution TEM image of an isolated CdSe QD. The lattice fringes confirm the crystallinity of the QDs. The capping MPA molecules cannot be recognized in the image.

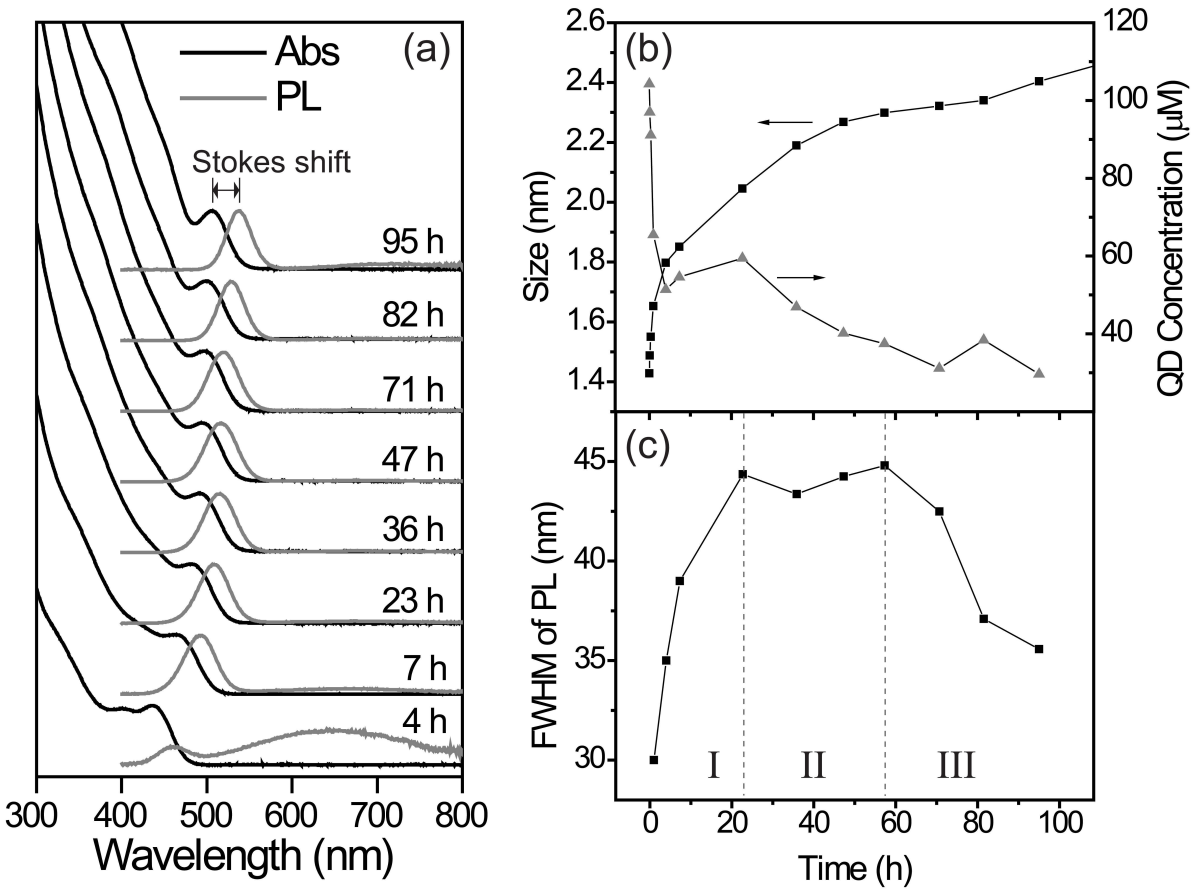

Figure 5.3: (a) The absorption and photoluminescence spectra of MPA-stabilized CdSe QDs after different synthesis times. (b) The evolution of the average size (diameter) of the QDs and their molar concentration during synthesis. (c) The evolution of the full width at half maximum (FWHM) of the photoluminescence of the QDs during synthesis.

5.3 Growth kinetics

5.3.1 Evolution of particle size and quantity

Figure 5.3(a) shows a series of absorption and photoluminescence (PL) spectra measured for the CdSe QD aliquots taken after different synthesis times. The absorption spectrum after 4 hours of synthesis shows two well-resolved peaks at around 430 nm and 400 nm, originating from the interband transitions $1S_{3/2}$-$1S_e$ and $2S_{3/2}$-$1S_e$, respectively (see section 2.4.1). The photoluminescence spectrum has two emission bands centered at 460 nm and 648 nm, respectively. The 460 nm band is due to the band-edge excitonic emission while the wide 648 nm band is from defect-related emission. When the synthesis is continued, the absorption and photoluminescence of the QDs shift gradually to longer wavelengths, illustrating the size-dependence of the band gap. The band-edge luminescence becomes stronger while the defect-related emission reduces and becomes undetectable after 23 hours of synthesis, due to the improvement of the crystal quality and the surface passivation of the QDs. From the absorption spectra, the QD size for these aliquot samples can be calculated with Equ. 4.1. The molar concentration of the QDs in the solution can also be deduced, as described in section

4.2.4.

Figure 5.3(b) shows the evolution of the QD size and concentration in the solution with the synthesis time. With the present experimental parameters, the smallest size of the QDs that can be obtained is about 1.4 nm. Under 100 °C refluxing, the QDs grow by incorporation of the Cd and Se monomers from the solution, as described in Equ. 5.2. The growth is fast at the beginning. The QD size increases from 1.4 to 2.0 nm in the first 20 hours. Then the growth gradually slows down and exhibits a saturation after about 50 hours. The final QD size measured after 95 hours of synthesis is ~ 2.35 nm. The reduction in the growth rate over time is due to the depletion of the monomers, especially the selenium monomer whose initial precursor concentration is much lower. In addition, when QDs grow bigger, they need more monomers to deposit on the surface for increasing a quantity of the radius.

The molar concentration of the QDs in the solution (solid triangle in Fig. 5.3(b)) quickly decreases during the growth process. At the beginning, the particle concentration is ~ 104 μM. This value decreases rapidly to 51 μM in the first 4 hours. Afterwards, the decrease slows down. After 95 hours of refluxing, the concentration reduces down to ~ 30 μM. This change is further accompanied with the change in the QD size distribution.

Figure 5.3(c) presents the full width at half maximum (FWHM) of the excitonic photoluminescence (PL) band of the QDs versus synthesis time. As stated above, the band width mostly originates from the size non-uniformity, i.e. size dispersion, of the QD ensemble. The evolution of the PL FWHM can be divided into three stages. At the beginning, the FWHM is around 30 nm. It increases quickly to 44 nm after 22 hours of growth (stage I). During the following 40 hours (stage II), the value has no big change. From 60 hours on, the PL FWHM decreases gradually (stage III). It is reduced down to ~ 35 nm after 95 hours of synthesis. This evolution curve can reflect the change of the QD size distribution during the synthesis process.

As described in section 2.5.1, the growth rate of QDs in the solution is particle-size-dependent at a given moment and varies continuously during synthesis, as presented in Fig. 2.15. There is a critical size r^*. QDs smaller than r^* have negative growth rates and will dissolve into the solution while QDs larger than r^* will grow by deposition of the monomers. When r^* is in the range of the QD size distribution, an Ostwald ripening process occurs.

The quick decrease in the QD concentration and the broadening of the QD size distribution observed in stage I in the present synthesis are typical characteristics of the Ostwald ripening growth process. After entering stage II, the QD size exceeds r^*, the Ostwald ripening stops. No particles will shrink anymore. The concentration and the size distribution of the QDs remain constant. When the QD sizes further increase and get to the descending part of the growth rate curve presented in Fig. 2.15, a size-focusing process occurs. In this process, smaller particles have larger growth rates and grow faster while larger particles grow slower. As a result, the size distribution will be narrowed, as observed in stage III in Fig. 5.3.

This growth kinetics is significantly different from that observed in organic phase synthesis. As reported by Peng et al. [68], QD growth in organic phase starts first with a quick size-focusing process. When the monomers are depleted, the critical size r^* for zero growth rate shifts to a larger value accordingly. When it increases into the range of the size distribution of the QDs, the Ostwald ripening process starts afterwards. In contrast, the present growth seems to immediately enter into an Ostwald ripening process after the synthesis starts. There could be also a short size-focusing period during the heating up process of the reaction mixture

(around 10 min). However, the absorption spectra of the samples taken during this stage have no well resolved peaks. Therefore, the extraction of the QD parameters is hindered.

The growth in aqueous phase could be explained by the large biased ratio between the concentrations of the cadmium and selenium precursors used for the synthesis (10:1 in molar). A large excess of one precursor was thought to ensure an approximately constant concentration of the generated monomers in the solution, which could provide a desirable condition for the construction of the most favorable surface structures of the QDs [148]. Such a scheme is suggested initially in the molecular beam epitaxy (MBE) growth of compound semiconductors to improve their surface quality [149]. It has been found that a largely biased precursor ratio is necessary to produce semiconductor QDs with high luminescence yield in aqueous phase [148].

Due to the relatively low concentration of the selenium precursor used in the present synthesis, the produced selenium monomers could be quickly depleted after nucleation at the beginning. This results in a large critical size r^*. Its value has no big change through the whole growth process due to the nearly constant concentration of the cadmium monomers. The QD growth starts first with the Ostwald ripening process. When the QD sizes quickly increase and exceed r^*, the size-focusing process is initiated.

5.3.2 Evolution of photoluminescence quantum yield

In this subsection, the evolution of the photoluminescence quantum yield (QY) of the CdSe QDs during synthesis is presented and discussed. The PL QY of the QDs is defined as the ratio between the number of the photons emitted through interband transitions to those absorbed. It is calculated using an ethanol solution of a dye Rodamine 6G as reference. The detailed process is described in section 4.2.5.

Figure 5.4 shows the temporal evolution of the PL QY of the CdSe QDs during synthesis. The solid line is plotted as a visual guide. Initially, the band-edge emission of the QDs is very weak. The photoluminescence is dominated by a wide defect-related band in longer wavelength region, as shown in Fig. 5.3(a). This corresponds to a nearly zero QY. As the synthesis proceeds, the value monotonically increases to a maximum ($\sim$ 11%) after 47 hours of refluxing. Then it gradually decreases. Such a phenomenon is commonly observed in different wet chemical synthesis methods of semiconductor QDs, including the synthesis in organic phase [146]. The position of the maximum PL QY is commonly referred to as the "bright point".

The origin for the existence of the bright point is still not completely understood. According to a common interpretation [146], the band-edge photoluminescence of semiconductor QDs is very sensitive to their surface states. Surface defects and unpassivated surface dangling bonds, for instance, could form deep levels in the band gap of the QDs. They act as trapping centers for the photogenerated carriers, inducing defect emission or non-radiative recombinations, which significantly reduces the QY of the QDs. It was thought that approximate chemical potentials of QDs and monomers in the solution would provide a favorable environment for the QDs to construct their preferable surface structures with few defects [146]. As shown in Fig. 5.3 (b) and (c), the bright point of CdSe QDs (47 h) appears during the stage II of the growth. In this stage, the Ostwald ripening terminates and the size focusing stage has not

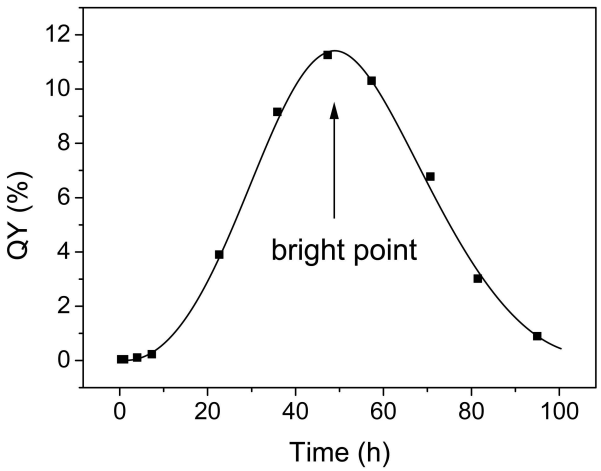

Figure 5.4: The photoluminescence quantum yield (QY) of the MPA-capped CdSe QDs as a function of synthesis time. The solid line is a visual guide.

started yet. The QD nuclei would not dissolve quickly into the solution while the monomers in the solution would not preferably deposit onto the QD surface, corresponding to a growth balance. The QD crystallinity could be improved in this stage, resulting the PL QY maximum.

In addition, the maximum QY of CdSe QDs (11%) obtained with this method is much lower than that reported by the organic phase synthesis (over 50%). It is mostly due to the relatively low boiling point of water which cannot provide sufficiently high synthesis temperature to achieve an effective annealing for the QD crystal structure during growth. As a result, structured defects could form in the crystal core of the QDs, inducing the low luminescence efficiency.

5.4 Size-dependent Stokes shift

In the optical spectra of CdSe QDs (Fig. 5.3(a)), it is interesting to notice a red shift of the photoluminescence maximum relative to the first absorption peak. This phenomenon is commonly observed in many types of semiconductor QDs, which is known as Stokes shift. The magnitude of the shift is sensitive to the particle size and shape. Its origin is related to the fine structure of the ground exciton level of the QDs and the presence of so-called dark excitons.

As introduced in section 2.4.3, in an ideal spherical CdSe QD crystallized in zinc-blende symmetry, its ground exciton state $1S_{3/2}1S_e$ has 8-fold degeneracy. This 8-fold degeneracy is lifted by the asymmetry in the practical QD shape, the electron-hole exchange interaction, and the possible crystallization in wurtzite structure [57, 150]. As a result, the ground exciton state is split into five levels. Two of them are optically inactive. Direct photoexcitation or radiative recombination for these states are impossible. Thus they are commonly called dark excitons. The energetic ordering of these levels and their spacing are sensitive to the particle size and shape. In most cases, the lowest energy level is a dark exciton state [57].

The excitation and relaxation processes considering the fine structure of the ground exciton state in CdSe QDs are schematically shown in Fig. 5.5. In the weak absorption regime, the absorbance of QDs depends exclusively on the oscillator strength of the electronic transitions.

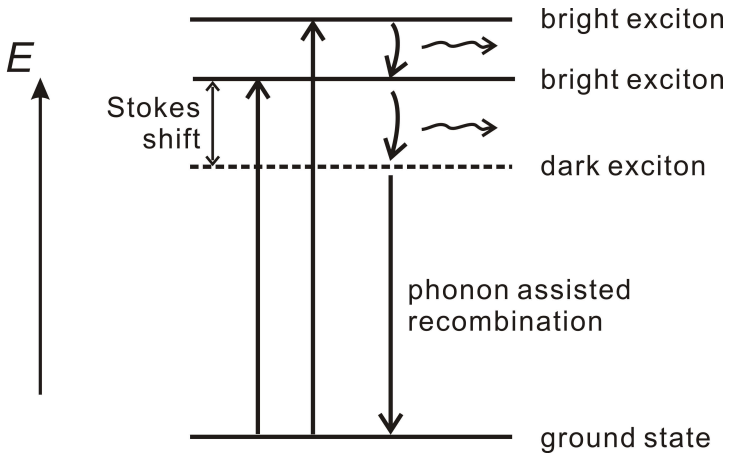

Figure 5.5: Schematic illustration of the excitation and relaxation processes involving the fine structure of the ground exciton state of CdSe QDs to explain the Stokes shift effect. The Stokes shift corresponds to the energy difference between the dark exciton level and the lowest bright exciton level.

Thus, the position of the first absorption peak is determined by the energy of the lowest bright exciton state. After excitation, the excitons will rapidly thermalize to the lowest dark exciton level by emitting phonons. Subsequently, the recombination can occur via phonon assisted process [150, 151]. The Stokes shift corresponds to the energy spacing between the lowest dark and bright exciton levels. Due to the requirement of the participation of phonons, the radiative lifetime of dark excitons is quite long, and it is reported to be ~ 1 µs at 10 K for CdSe QDs [57].

The Stokes shift of the prepared CdSe QDs is plotted in Fig. 5.6 versus the QD size. Its value varies in the range of 100–200 meV. The overall trend of the evolution is that the shift decreases with increasing QD size but with strong fluctuations. As described in section 2.4, for larger QDs, the quantum confinement effect and the electron-hole exchange interaction become weaker. Thus, the splitting of the ground exciton level reduces, resulting in the decreased

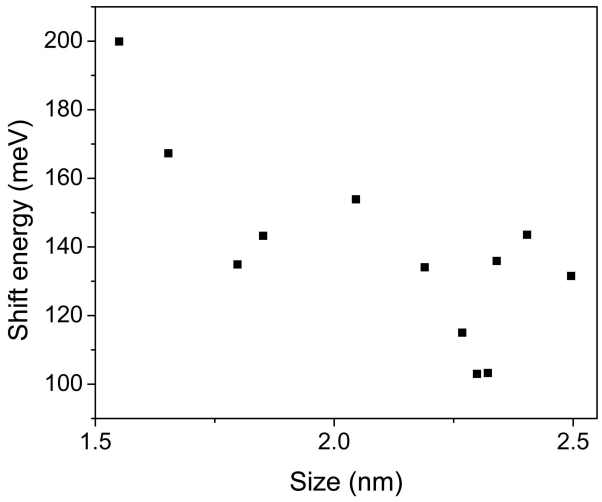

Figure 5.6: Stokes shift of CdSe QDs prepared by the aqueous phase synthesis method as a function of the QD size.

Stokes shift. However, it is difficult to find a systematic dependence in the present results. As mentioned above, the QD shape could influence Stokes shift significantly. Thus, these fluctuations in the dependence are probably due to a continuous variation in the QD shape during synthesis.

5.5 Photoluminescence quenching in oxygen-deficient environments

In many applications, QDs operate directly in open gas environments. Due to their small sizes, the ambient conditions could impose essential influence on their properties. In this section, the photoluminescence properties of the MPA-capped CdSe QDs in dry powder form are investigated in different gas environments. The as-prepared QDs (120 hours of synthesis) were first purified with the procedure described in section 4.2.2. Then the QD precipitation was left in air overnight to dry naturally. The obtained QD powder was transferred onto a silicon wafer and spread to a thin layer for full exposure to ambient gas. This sample is used for the subsequent photoluminescence measurements. The sample is placed in a vacuum chamber which can be evacuated to $\sim 10^{-6}$ mbar and flushed with gas flow. A HeCd laser emitting at 325 nm is used as excitation source. A mild laser intensity (~ 0.01 W/cm^2) was used to avoid significant degradation of the QDs under irradiation.

Figure 5.7 shows the temporal evolution of the excitonic luminescence intensities of the QD powder measured in air, vacuum and nitrogen flow, respectively. The time zero is set at the start of the laser irradiation. All results have been normalized to their initial PL intensities for easy comparison. In air, the PL intensity decays slightly over time. It is reduced down to 0.9 of the initial value after 10 minutes. This is probably due to a little degradation of the QDs under laser irradiation. When the measurements are performed in vacuum, the PL intensity significantly decreases. In the first minute, the luminescence is reduced to half of the initial intensity. Then the decrease gradually slows down. After 10 minutes of irradiation, it decreases to 0.24 of the initial value. When atmospherical air is filled into the sample chamber, the PL intensity of the QD powder is observed to increase rapidly and return to the initial value within 10 minutes. The whole process is reproducible. Repeated evacuation-flooding processes yield similar results. In addition, it is interesting to notice that the initial PL intensity of the QDs recorded in vacuum is similar to that measured in air. This indicates that the vacuum pumping solely could not reduce the PL intensity. These observations indicate that the PL quenching of the QD powder in vacuum is a surface effect.

The PL measurements are further performed in a nitrogen flow. For this purpose, a constant dry nitrogen flow is introduced to pass through the sample chamber. Before the PL measurements, the chamber is flushed for 10 minutes with the gas to remove the inside air. A gas flow is used with the consideration that it can carry away the molecules that could be detached from the QD surfaces during the PL measurements. As shown in Fig. 5.7, the PL evolution of the QD powder exhibits a very similar behavior to that in vacuum. The final intensity in nitrogen flow is 0.3 times the initial value, which is slightly higher than that measured in vacuum. Filling of air into the chamber restores again the photoluminescence intensity of the QDs. These results demonstrate that nitrogen is not the component in air which controls the photoluminescence properties of the QD powder.

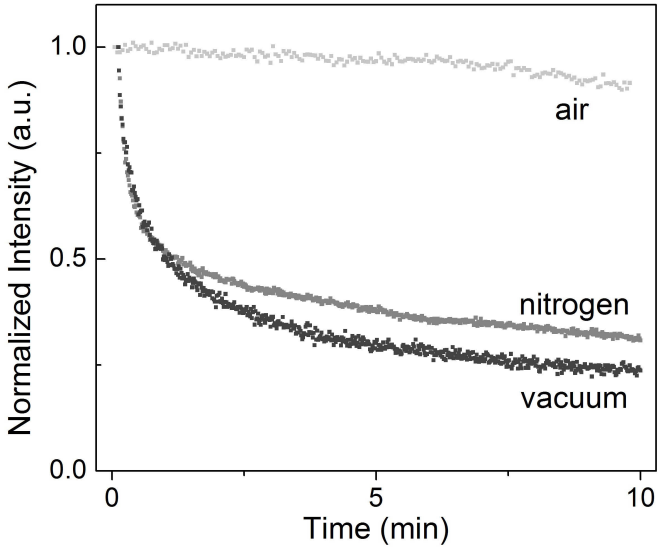

Figure 5.7: Temporal evolution of the excitonic photoluminescence maxima of MPA stabilized CdSe QD powder measured in air, vacuum, and nitrogen flow, respectively. A HeCd laser operating at 325 nm is used as excitation source. All the measurements are performed with the same laser intensity. The measuring setup is presented in Chapter 4. The time zero is set at the start of laser irradiation. The results are normalized to the initial photoluminescence intensities for easy comparison.

In previous studies it has been found that under continuous photo-excitation, the photoluminescence of individual QDs randomly switches between emission states with high and low intensities, which are referred to as emission ON and OFF states, respectively [152–155]. This phenomenon is known as luminescence blinking, which is not only observed in semiconductor QDs but also in many other types of molecular emitters such as dyes [156], polymers [157], and carbon nanotubes and nanowires [158]. These ON and OFF states are conventionally attributed to a neutral QD and a charged QD model, respectively [155].

A schematic of the luminescence blinking phenomenon is shown in Fig. 5.8(a). In the bright ON state, the luminescence is dominated by radiative recombinations of excitons, which is characterized with a mono-exponential decay dynamics with a lifetime typically in the range of 15–30 ns. The occurrence of OFF states is induced by the generation of an additional charge in the QD core. In this case, excitons will recombine through a non-radiative Auger-type process, in which the exciton transfers its energy to the extra charge carrier rather than emitting a photon. The Auger recombination process further induces a significantly shortened lifetime of the band-edge excitons (a few nanoseconds or less [155], Fig. 5.8(b)). As a result, the photoluminescence intensity of the QD is largely reduced.

The mechanism for the QD charging during the luminescence OFF period is attributed to surface defects of the QDs such as unpassivated dangling bonds and structured defects [159], which could form energy levels in the forbidden gap that act as trap centers for the photoexcited carriers, as schematically shown in Fig. 5.8(c). When a charge carrier is captured by the trap centers, the QD core becomes charged, initiating the luminescence OFF period. During this period, the extra free carrier could be excited to higher energy states by absorbing the energy of excitons. This energy is, in some cases, high enough to excite the carrier into the outside capping surfactant ligands. This also hinders the neutralization of the defect states. Therefore,

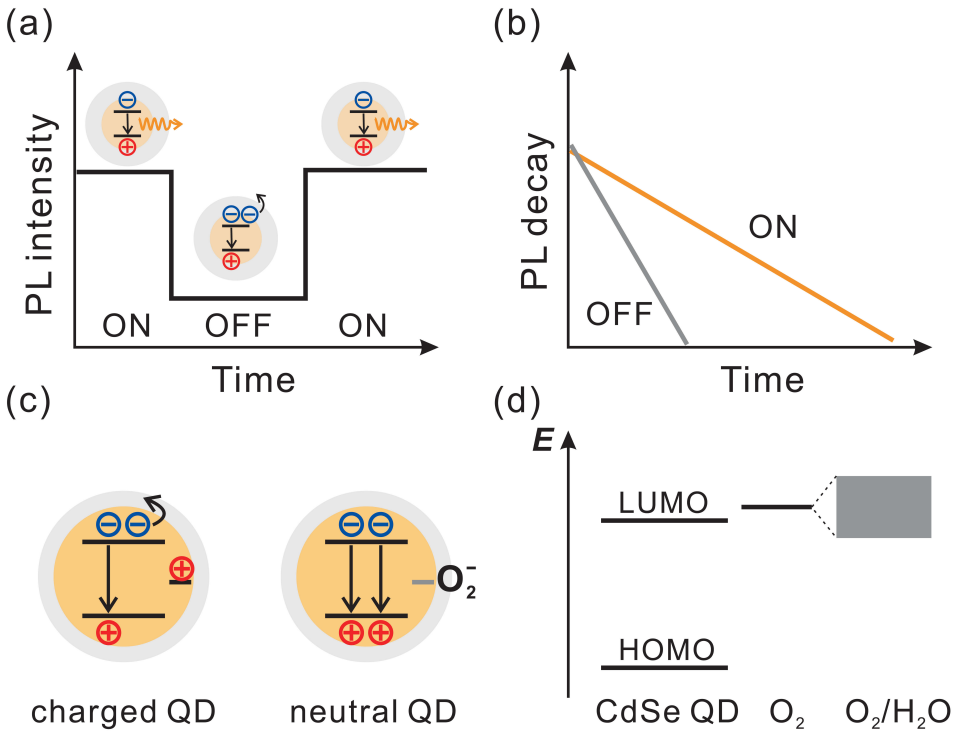

Figure 5.8: Schematic of the luminescence blinking of CdSe QDs and the effects of oxygen and water molecules. (a) Random switching between the ON and the OFF states in the blinking process. The bright ON state corresponds to radiative exciton recombination in a neutral QD. The OFF state is related to non-radiative Auger processes in a charged QD. (b) Schematic of the PL decay during the ON and OFF period. The Auger recombination process is much quicker than the neutral exciton recombination, leading to a shorter radiative lifetime of the OFF state. (c) Left: surface defect level in QDs acts as trap centers for photoexcited holes, inducing a charged QD core. Right: oxygen molecule passivates a defect state, ensuring a neutral core and high-intensity emission. (d) Energy level alignment of CdSe QDs and the oxygen redox potential. The oxygen redox potential level is significantly broadened under the presence of water molecules.

a macroscopic time period (on the order of seconds) of the ON and OFF states are normally observed.

The luminescence blinking of QDs was found to be sensitive to the gas atmospheres [153,154]. In a study of single CdSe/ZnS core shell nanocrystal, when the measuring environment was changed from air to vacuum, the duration of the ON state was significantly shortened while the probability of the OFF event is remarkably increased [153]. As a result, the overall luminescence intensity was observed to decrease by a factor of 60 in vacuum [153]. Oxygen molecules were proposed to account for this phenomenon. It was suggested that oxygen molecules in air can effectively passivate the surface defects in QDs. A direct oxidation of the defects could occur by transferring their extra electrons to surface oxygen molecules, as illustrated in Fig. 5.8(c). This effect passivates the possible hole traps and prevents the QD core from charging during photoexcitation. In an oxygen-deficient environment, oxygen molecules are detached from the QD surface. As a result, the probability of the luminescence OFF state is significantly enhanced by the active surface traps.

Water molecules in air were also found to strongly influence the luminescence blinking properties of QDs [153]. When considering the energy level for the redox potential of oxygen, a small barrier exists for electrons transfer from the CdSe QD to oxygen, as illustrated in Fig. 5.8(d). Presence of strongly polar medium such as water molecules could lead to a broadening of the oxygen redox level, thereby facilitating electron transfer to form O_2^- species. It was reported that the photoluminescence of CdSe/ZnS core/shell QDs in atmospheric air was 9 times stronger than that in dry oxygen, due to the water molecule-assisted passivation of the QD surface in air [153].

The present observations for the MPA capped CdSe QD powder are consistent with the above model. In addition, the fact that the PL of QDs remains unchanged during evacuation and rapidly decreases in vacuum when photoexcitation starts further demonstrates that photoexcitaton is a requisite to detach oxygen from the QD surface. One possible mechanism is through the reduction of the oxygen ions by the photogenerated holes. As a result, the oxygen molecules are converted to be physisorbed on the QD surface, and can be easily detached by evacuation or nitrogen gas flow. However, when measured in air, the active surface defect sites of the QDs could be quickly re-passivated, due to the abundance of oxygen molecules in the surroundings. This ensures a high photoluminescence intensity of the QDs.

The effect of water vapor in air is not specially examined in this case. However, the work presented in Chapter 6 suggests that oxygen-related surface passivation of the CdSe QDs in dry oxygen gas is not so effective like that in the atmospheric air without the assistance of water molecules.

5.6 Chemical stability

Water soluble semiconductor QDs usually suffer from gradual degradation of their surface passivation during storage [160]. In this section, the chemical stability of the MPA-capped CdSe QDs against light irradiation and oxidation is examined and analyzed.

The as-prepared QDs are purified from the crude solution following the procedure described in section 4.2.2. The purified QDs are re-dispersed in deionized water with the same concentration as in the as-prepared solution. Then, it is distributed into eight 2 ml transparent glass vials and their pH values are adjusted with tetraethylammonium hydroxide, respectively. The vials are covered with parafilm with small holes onside. The pH value for these QD samples and their storage conditions are listed in Table 5.1. The samples N1–N4 and A1–A4 are placed in two identical gas-tight glass bottles, which are evacuated and filled with dry nitrogen and atmospheric air, respectively. Four of the samples are wrapped with aluminum paper for the darkness storage condition.

Figure 5.9 shows the photographs of the QD samples taken after four weeks of storage ((a) in nitrogen, (b) in air). The QDs stored in dry nitrogen still preserve excellent dispersity in the solution. In contrast, QD samples stored in air undergo significant aggregation. The QDs in sample A1–A3 form big agglomerates which deposit at the bottom of the vials with nearly colorless supernatant liquid. However, the sample A4 with pH of 10.5 stored in darkness still shows high dispersity without obvious aggregation.

There are three main mechanisms for the degradation of thiol-stabilized CdSe QDs [160]: one

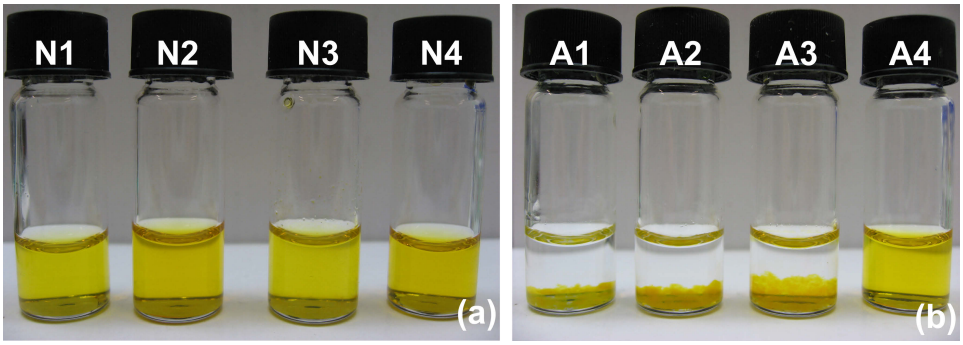

Figure 5.9: Photograph of the CdSe QD samples after two week storage in nitrogen (a) and air (b) for the chemical stability experiments.

is the light irradiation induced photo-oxidation of the ligands in which the photogenerated holes react with the thiol groups with the presence of oxygen. This can detach the ligands from the QD surfaces. These detached ligands are converted into disulfide compounds afterwards [160]. When nearly all of the ligands are removed, the QDs will aggregate together and precipitate out of the solution.

The photo-oxidation process is probably accompanied by two additional effects, the chemical oxidation and the hydrolysis of the thiol bindings, but at relatively lower rates. The stability of the cadmium-thiol bonds on the QD surfaces is sensitive to the pH of the solution environment. In the solution, the thiol group could occur a hydrolysis process, which is related to its acidity described by the acid dissociation constant pK_a. An acid HA in a water solution could dissociate and form the following equilibrium

$$\mathrm{HA} \rightleftharpoons \mathrm{H^+ + A^-} \tag{5.3}$$

Its pK_a is calculated by the equilibrium concentrations (in mol/l) of the chemical species,

$$\mathrm{p}K_a = -log_{10}\left[\frac{(H^+)(A^-)}{(HA)}\right] \tag{5.4}$$

The pKa is $\sim$ 10.2 for the thiol group in MPA molecules. When the pH of the QD solution

Table 5.1: Parameters for testing the chemical stability of the CdSe QDs. Natural ambient light is used for ambient light condition of the samples. The darkness condition is realized by wrapping the sample vials with aluminum paper.

Sample Nr.	pH value of QD solution	Storage: atmosphere	Storage: light conditions
N1	7.0	nitrogen	ambient light
N2	10.5	nitrogen	ambient light
N3	7.0	nitrogen	darkness
N4	10.5	nitrogen	darkness
A1	7.0	air	ambient light
A2	10.5	air	ambient light
A3	7.0	air	darkness
A4	10.5	air	darkness

is below this value, the thiol ligands will gradually detach from the QD surface due to the hydrolysis effect.

In the present study, for the QD samples stored in nitrogen (N1–N4), photo- and chemical oxidation of the ligands are avoided. The well-preserved dispersity of the dots indicates that the hydrolysis of the ligands in the sample N1 and N3 dissolved in pure water is quite slow and has negligible effect during the experimental period. In comparison, the samples stored in air suffer from severe oxidation effect. The samples A1 and A2 exposed to ambient light exhibit severe aggregation due to the combined effects of the photocatalytic and chemical oxidation while the hydrolysis of the ligands further occurs in A1. In A3 and A4, the photo-oxidation effect is prevented. Compared to A4, A3 suffers from further the ligand hydrolysis degradation in addition to the chemical oxidation, which induces the aggregation of the QDs. However, it seems that the extent of QD aggregation becomes gradually milder from A1, A2 to A3, demonstrating that the photo-oxidation is the dominant effect in the degradation of the QDs during storage.

5.7 Summary

In this chapter, colloidal CdSe QDs are synthesized using a wet chemical method. The growth kinetics of the QDs is studied. The size-dependent Stokes shift and the photoluminescence quenching of the QDs in oxygen-deficient environments are investigated. At last, the chemical stability of the prepared QDs is examined.

The prepared QDs are capped with bifunctional thiol-carboxyl molecules as stabilizers. TEM measurements demonstrate the spherical shape of the QDs and their crystallinity. The absorption spectra of the QDs exhibit multiple peak features arising from different electronic transitions. The absorption peak with the lowest energy is assigned to the transition from the $1S_{3/2}$ hole level to the $1S_e$ electron level of the QDs. Based on a previously reported method, the evolutions of QD size and size distribution during the synthesis are extracted from optical measurements. CdSe QDs synthesized by this method have sizes in the range of 1.4–2.5 nm with molar concentration of 30–100 μM in the crude solution. Based on these results, the growth mechanism of the QDs is analyzed.

The growth of the QDs can be divided into three stages. At the beginning (0–20 h), the growth is based on an Ostwald ripening process in which smaller particles in the solution gradually shrink while the bigger ones continue to grow. This deviation in the growth rates results in the quickly decreased total number of the particles and the broadening of the particle size distribution. Afterwards, with increased average particle size, the growth enters into a balanced stage where the growth rate slows down and the size distribution tends to be constant. This stage lasts for another 20 hours. After that, the growth enters a size-focusing stage, which is characterized by a gradual narrowing of the particle size distribution. During this stage, smaller particles have larger growth rates and vice versa. This process lasts until the termination of the synthesis. This study improves the understanding of the growth kinetics in the aqueous phase synthesis of semiconductor QDs.

In addition, a so-called bright point phenomenon is observed for the synthesis. It represents the fact that there exists a specific time for QD synthesis at which the photoluminescence quantum yield of the QDs reaches its maximum ($\sim$ 11% for the present synthesis). The appearance of

the bright point is thought to correspond to the balancing between the QD shrinking and growth during synthesis. For applications that prefer high luminescence efficiency of the QDs, it is crucial to determine the bright point in order to obtain QDs with high optical quality.

The Stokes shift effect — the redshift of the photoluminescence with respect to the absorption, is studied for the prepared CdSe QDs. Its value is found to vary in the range from 100 to 200 meV for differently sized QDs. It exhibits an overall decreasing trend with increasing QD size but with strong fluctuations. This non-systematic dependence is probably due to the continuous variation in the QD shape during the synthesis process.

The photoluminescence of the prepared QDs in dry powder form is studied in air, vacuum, and nitrogen flow, respectively. The luminescence intensity is found to be strongly dependent on the ambient gas. In air, the photoluminescence is approximately constant while it decreases dramatically in vacuum and nitrogen flow. Referring to previous studies on the optical properties of single semiconductor QDs, this photoluminescence quenching effect is attributed to oxygen-controlled surface effects in the QDs. Surface defects of QDs act as trap centers for photogenerated charge carriers during excitation, which can induce a temporally charged QD core and non-radiative Auger-type recombination channels with significantly shortened lifetimes. Oxygen was found to passivate these surface defects and ensure a high luminescence efficiency, which results in the ambient-dependent photoluminescence of QDs. The experimental results indicate that the charge relaxation dynamics of semiconductor QDs is very sensitive to the ambient environments, which should be paid special attention to during the design of the related devices and the studies on the electronic operating properties.

The chemical stability of the prepared CdSe QDs is further examined. CdSe QD dispersions stored in air with exposure to ambient light undergo severe aggregation after two weeks of storage, which is maily attributed to the photooxidation of the capping ligands of the QDs. The experimental observations suggest that an oxygen-free, dark condition and high pH value (relative to the pKa of the thiols) of the dispersion are beneficial for maintaining the chemical stability of thiol stabilized semiconductor QDs.

Chapter 6

Oxygen-controlled Photoconductivity in ZnO Nanowires Functionalized with Colloidal CdSe Quantum Dots

One important research topic in contemporary nanotechnology is the assembly and study of hybrid nanostructures for fabrication of functional devices. Semiconductor quantum dots (QDs) represent one kind of interesting nanomaterials featured with their striking size-tunable band gaps, which makes them promising candidates as photo-sensitisers. Semiconductor nanowires, as quasi-one-dimensional materials, are natural transport media for charge carriers in optoelectronic devices. ZnO is a widely studied semiconductor due to its direct wide band gap, large exciton binding energy, and high electron mobility. In this chapter, a hybrid nanostructure is fabricated by surface functionalization of ZnO nanowire (NW) arrays with colloidal CdSe QDs. This hybrid structure has potential applications in photosensing and photovoltaic devices. Through photoconductivity measurements, the charge transfer mechanism in the hybrid structure and the influence of the operating gas environment are studies.

The first section presents the assembly method of the ZnO-NW/CdSe-QD hybrid structures and their optical and structural characterization. In the second part, the photoconductivity of the hybrid sample is investigated in different gas environments, including air, oxygen, vacuum, and inert gases. In order to specifically study the charge transfer mechanism between the nanowires and the QDs, a laser with a photon energy that can exclusively excite the CdSe QDs is used as excitation source. After that, the influence of the ambient gas, with emphasis on oxygen, on the optical and electrical properties of ZnO nanostructures and CdSe QDs is discussed. In the fourth section, a model of the electron transfer mechanism in the NW/QD hybrid structure is proposed to explain the photoconductivity results. The last section summarizes the results obtained in this chapter.

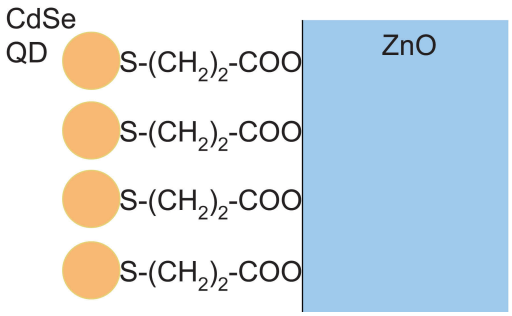

Figure 6.1: Schematic of the ZnO-nanowire/CdSe-quantum-dot (ZnO-NW/CdSe-QD) hybrid structure.

6.1 Surface functionalization of ZnO nanowires with CdSe quantum dots

In this section the surface functionalization of ZnO nanowires (NWs) with colloidal CdSe quantum dots (QDs) is presented. The obtained hybrid sample are characterized with optical and transmission electron microscopy (TEM) measurements.

The ZnO nanowires used in this work are grown on fluorine-doped tin oxide (FTO) coated glass sheets by a hydrothermal method. The detailed growth procedure is described in section 4.1.1. The prepared nanowire arrays have diameters in the range of 50–300 nm and lengths $\sim$ 1 µm. The nanowire density on the glass substrate is around 10^9 cm^{-2}. Colloidal CdSe QDs are synthesized with a method described in Chapter 5. The QDs are capped with a layer of bifunctional 3-mercaptopropionic acid (MPA) molecules (HS-$(CH_2)_2$-COOH) and are soluble in water. The thiol groups of the MPA molecules are bound to the QD surfaces. The outgoing carboxyl groups can form chemical bonds with the zinc ions on ZnO nanowire surfaces [15], as schematically shown in Fig. 6.1, which allows an efficient attachment of the QDs on the nanowires.

The surface functionalization process of ZnO nanowires with CdSe QDs is as follows. After synthesis, the CdSe QDs are purified from the reaction solution following a procedure described in section 4.2.2. This step removes the residual chemicals in the crude solution, especially the MPA molecules, which can compete with the QDs to deposit on the nanowire surface. Then the QDs are re-dispersed in deionized water with molar concentration of $\sim$ 30 µM. The pH value of the dispersion is adjusted to 9.0 by addition of tetraehylammonium hydroxide. In atmosphere, there are many gas molecules and compounds like hydrocarbon and hydroxyl species adsorbed on the surface of ZnO [15, 161], which hinders the binding of the CdSe QDs. To remove these adsorbed species, the as-grown ZnO nanowires are annealed in air at 500 °C for 1 hour. Then the nanowires are immersed in the QD solution and kept inside for one day to ensure a saturated attachment of the QDs. After that, the sample is extracted and rinsed completely with deionized water. Then it is left in air overnight to dry naturally. The final sample is referred to as ZnO-NW/CdSe-QD hybrid structure.

Figure 6.2(a) shows a scanning electron microscope (SEM) image of the as-prepared ZnO nanowire arrays. The nanowires show approximate hexagonal cross section, indicating their growth along the c-axis of the hexagonal wurtzite symmetry. After QD coating, a weak color change can be seen on the nanowire samples, which can be used as a quick judgement for QD

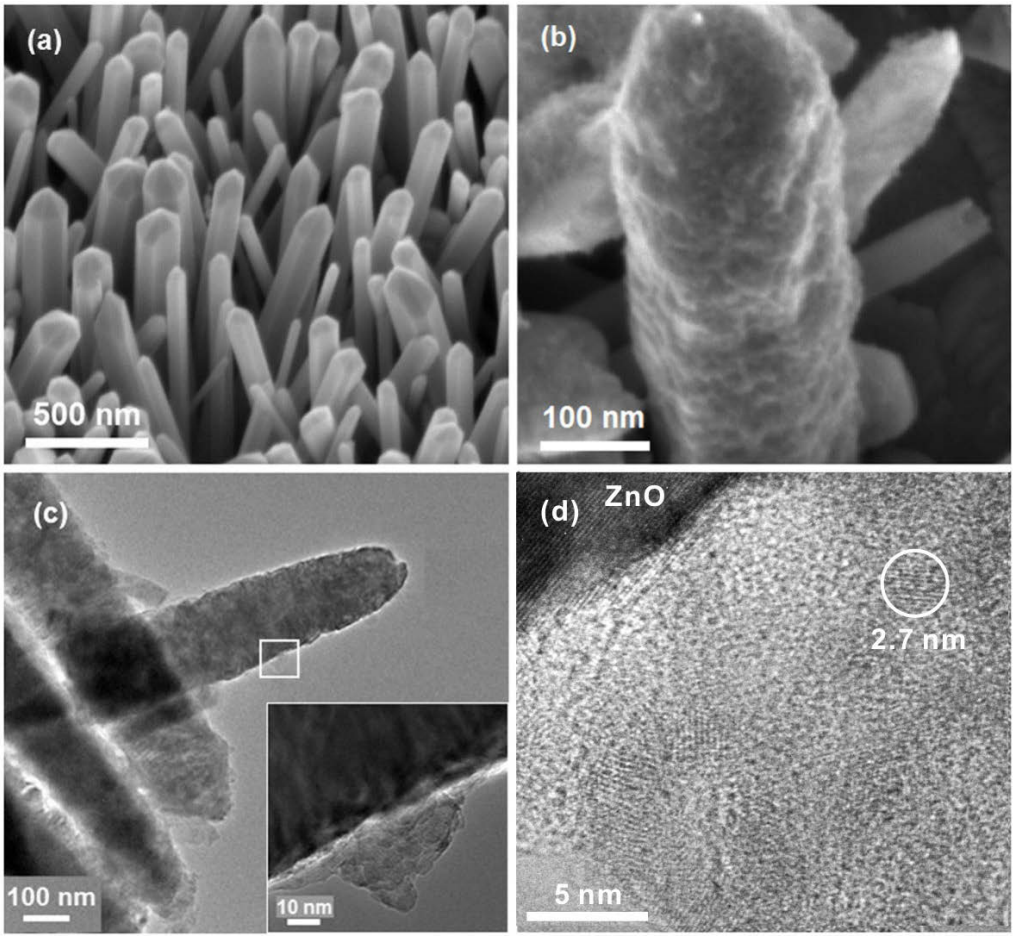

Figure 6.2: (a) SEM image of as-prepared ZnO nanowires. (b) SEM image of a single ZnO nanowire coated with CdSe QDs. The QDs form cluster-like structures on the nanowire surface. (c) TEM image of ZnO nanowires coated with CdSe QDs. The inset is a magnification of a QD cluster on the nanowire surface. (d) HRTEM image of the CdSe QD cluster. A QD is marked with a circle. The TEM and HRTEM measurements were performed by K. Frank in the group of Prof. A. Rosenauer at the Institute of Solid State Physics, Universität Bremen.

attachment. A SEM image of a single ZnO nanowire after QD coating is shown in Fig. 6.2(b). The coating material forms clusters on the nanowire surface. The thickness of the coating layer at the most densely coated places is estimated to be around 20 nm while some areas seem to be poorly covered. The clustered structure is probably due to a partial capping of the QDs, which results in QD aggregation during the coating process. As discussed in section 5.6, when the pH value of the CdSe QD solution is below the pKa of the thiol groups in the stabilizer molecules ($\sim$ 10.2 for MPA), the stabilizers will gradually detach from the QD surface as a result of the slow hydrolysis of the thiol groups. In this way, the attachment efficiency of the QDs is increased.

Figure 6.2(c) shows a TEM image of QD-coated ZnO nanowires. The samples for TEM measurements are prepared by scratching a small amount of the nanowires from the glass substrate and transferring them onto carbon coated copper grids. In the TEM image, the QD agglomerates can be recognized as dark floccules. The inset is a magnified image of a QD cluster with a dimension around 30 nm. A high resolution TEM (HRTEM) image of the QD cluster is shown

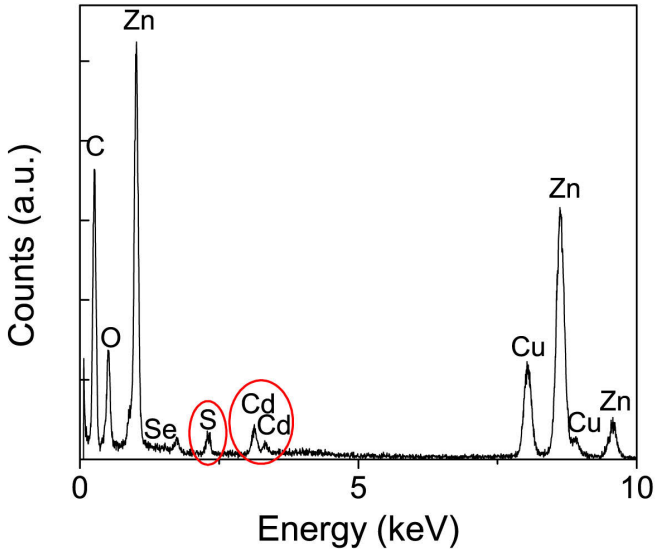

Figure 6.3: Energy-dispersive X-ray (EDX) spectrum of the ZnO-NW/CdSe-QD hybrid sample measured by K. Frank in the group of Prof. A. Rosenauer at the Institute of Solid State Physics, Universität Bremen.

in Fig. 6.2(d) and the QDs can be identified by their lattice fringes.

Figure 6.3 shows an energy-dispersive X-ray (EDX) spectrum of the ZnO-NW/CdSe-QD hybrid sample. The peaks assigned to Zn and O in the spectrum arise from the ZnO nanowires. The Cu signal is due to the used copper grid for preparation of the TEM sample. The distinct Cd and S peaks are from the QD core and the thiol groups of the stabilizer molecules, respectively. The strong peak assigned to carbon is due to the carbon coating of the copper grid and

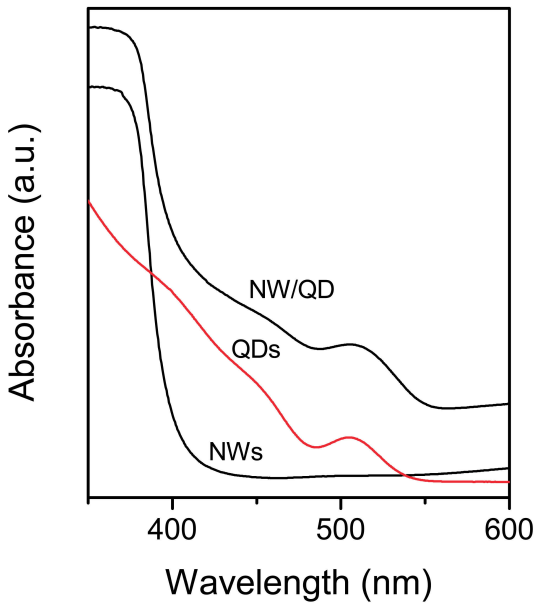

Figure 6.4: Absorption spectra of ZnO nanowires before and after QD coating. The spectra are shifted vertically for clarity. The red line is the absorption spectrum of the CdSe QDs in solution phase.

the MPA stabilizers of the QDs. This finding demonstrates that the coating material on the nanowire surface is the MPA-capped CdSe QDs.

Figure 6.4 compares the absorption spectra of the ZnO nanowires before and after coating with CdSe QDs. A spectrum of CdSe QDs dispersed in water solution is also plotted for comparison. The absorption onset of ZnO appears around 400 nm due to the interband transition [19]. In the absorption spectrum of the NW/QD hybrid sample, extra absorption appears in the range between 400–550 nm, which is attributed to the deposited CdSe QDs. The first absorption peak at 505 nm arises from the fundamental electronic transition between the $1S_{3/2}$ hole level and the $1S_e$ electron level of the QDs (see section 2.4.1). Using the empirical equation 4.1, the average size of the CdSe QDs can be calculated from the first absorption peak position to be 2.4 nm. In comparison to the reference QD sample, the absorption peak of the QDs in the hybrid sample has no obvious spectral shift or band width broadening. This illustrates that the optical properties of the QDs are well preserved after attaching onto ZnO nanowires.

6.2 Photoconductivity of the ZnO-nanowire/CdSe-quantum-dot hybrid structure

In this section, the photoconductivity (PC) properties of the ZnO-NW/CdSe-QD hybrid structure are investigated. Photoconductivity is an optical and electrical phenomenon that describes the change of the electrical conductivity of materials due to light irradiation. An argon ion laser emitting at 458 nm (2.7 eV) is used in the present work for excitation. Thus its photon energy is below the band gap of ZnO (3.37 eV at room temperature [27]), exciting only the CdSe QDs in the hybrid samples. The photoresponse of the electric current flowing through the ZnO nanowires under constant bias voltage is measured. The detailed information about the measurement procedure and the experimental setup are described in section 4.3. Several NW/QD hybrid samples have been investigated, and all measurements exhibited similar behaviors. The results shown here were obtained all from the same sample.

6.2.1 Photoconductivity in air

Figure 6.5(a) shows the temporal evolutions of the electric current for the NW/QD hybrid sample and a pure ZnO nanowire sample for reference. The reference sample has been thermally treated with the same conditions as used in the assembly of the NW/QD hybrid sample. The laser intensity is 1.0 mW/cm^2. The bias voltage applied on the nanowires is 1 V. When laser irradiation starts, the current of the hybrid sample rapidly increases from the initial 28 μA to 200 μA in the first 6 minutes. After 30 minutes of irradiation, it reaches a value around 250 μA. Then the current gradually approaches saturation. When the laser is blocked, the current drops immediately with a rate slowing down over time. It takes more than 6 hours for it to return completely to the original dark value. In comparison, the current enhancement in the bare ZnO nanowires under irradiation is very weak. The current climbs from 36 μA to 56 μA in 2 hours and restores back to the original value in darkness. The above observations indicate that the CdSe QDs in the hybrid sample play a crucial role in its strong PC enhancement.

The decay kinetics of the photoconductivity in darkness can be well described by a stretched

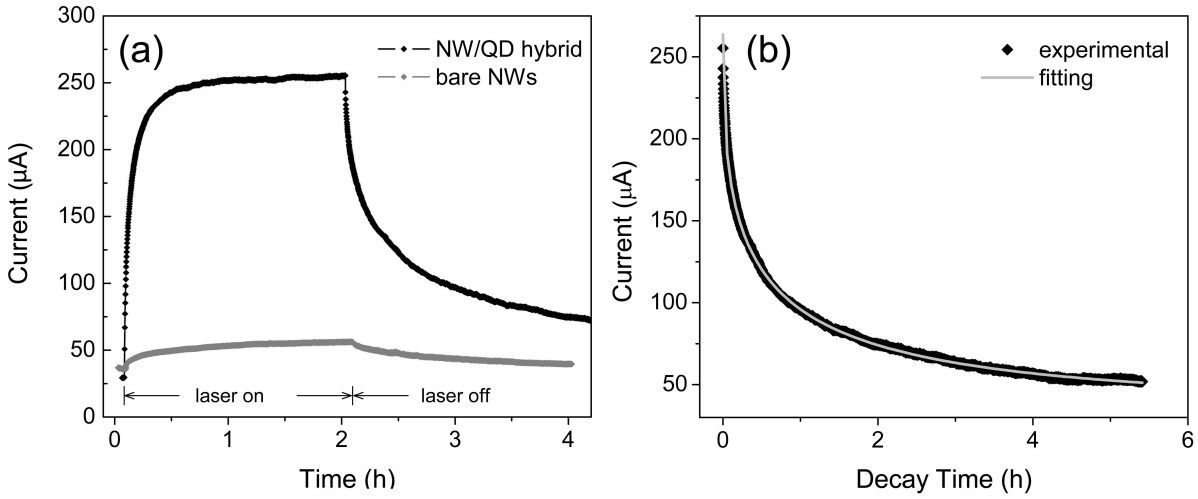

Figure 6.5: (a) Photoresponse of the current of the ZnO-NW/CdSe-QD hybrid sample and a bare ZnO NW reference sample measured in air as a function of time. (b) Decay kinetics of the current of the NW/QD hybrid sample in darkness fitted with the stretched exponential function Equ. 6.1.

exponential function with the form:

$$I = I_{inf} + (I_0 - I_{inf})exp[-(t/\tau)^{\alpha}] \tag{6.1}$$

where I_0 and I_{inf} are the steady-state current reached under irradiation and the final dark current after decay. τ is the decay time constant, describing the decay speed. α is the stretching exponent. The zero point of time t is set at the termination of laser irradiation. Figure 6.5(b) shows the fitting result of the current decay in air up to 5.5 h with the parameters $\tau = 0.5$ h and $\alpha = 0.43$. It can be seen that the experimental result shows an overall excellent agreement with the model in the whole time period.

To further examine the effect of the QDs in the photoconductivity enhancement, new measurements are performed using a laser emitting at 532 nm. Figure 6.6 shows the measured current evolutions of the NW/QD sample compared with the results obtained using the argon ion laser with the same photon flux. As shown in the inset, the 532 nm laser locates spectrally at the absorption tail of the QDs, implying that it can only excite a small part of the QDs. The current evolution kinetics in both cases is very similar to that observed in Fig. 6.5(a). However, the steady current reached under the 532 nm irradiation is only 75 μA compared to 160 μA reached under the argon ion laser. This observation is consistent with the above speculation, confirming that the CdSe QDs are strongly involved in the PC enhancement of the NW/QD hybrid sample.

To interpret the observed PC enhancement in the NW/QD sample, the energy band alignment of the hybrid structure has to be considered. It is known that the size-dependence of the band gap is one of the main interesting features of semiconductor QDs. In the frame of the effective mass approximation [45, 162], the band edge positions (E_{cb} for the conduction band and E_{vb}

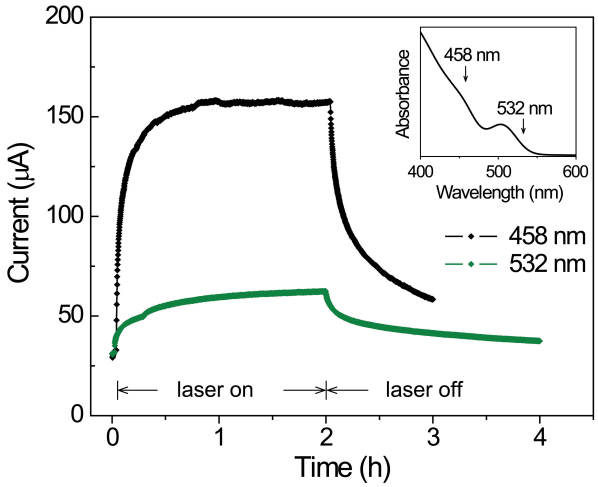

Figure 6.6: Photoresponse of the current of the ZnO-NW/CdSe-QD hybrid sample versus time under different laser irradiation.

for the valence band) can be approximately determined by

$$E_{cb} = E_{cb,bulk} + \Delta E \frac{m_h^*}{m_h^* + m_e^*} \tag{6.2a}$$

$$E_{vb} = E_{vb,bulk} - \Delta E \frac{m_e^*}{m_h^* + m_e^*} \tag{6.2b}$$

with

$$\Delta E = E_{g,QD} - E_{g,bulk}$$

where $E_{g,bulk}$, $E_{cb,bulk}$ and $E_{vb,bulk}$ are the band gap energy, the conduction band and the valence band positions of the bulk semiconductor material, respectively. $E_{g,QD}$ is the band gap energy of the QDs determined from the spectral position of their first absorption peak. m_e^* and m_h^* are the effective masses of electrons and holes, respectively. For CdSe, the following parameters are taken [162]. $E_{g,bulk}$ is around 1.74 eV at room temperature. The bulk band edges locate at $E_{cb,bulk} \approx -4.3$ eV and $E_{vb,bulk} \approx -6.04$ eV in the absolute vacuum scale. The effective masses of electrons and holes are $0.13m_0$ and $0.45m_0$, respectively. The first absorption peak of the CdSe QDs in the hybrid sample is measured to be 505 nm, corresponding to a band gap of 2.45 eV. From Equ. 6.2a, the absolute energy positions of their conduction band and valence band are determined to be -3.75 eV and -6.20 eV, respectively. For the band positions of ZnO nanowires, bulk values are taken. The conduction band is located at around -4.19 eV [163]. Using the band gap of 3.37 eV of ZnO [164], its valence band position is determined to be -7.56 eV.

Figure 6.7 shows a diagram of the energy band alignment inside the NW/QD hybrid structure in the absolute vacuum scale. When electrons in the CdSe QDs are photoexcited, they can transfer into the conduction band of ZnO nanowires lying at a lower energy position, which increases the concentration of the conduction electrons in the nanowires and therefore increases the conductivity. This charge transfer may be a factor that accounts for the observed PC enhancement of the hybrid sample. However, such a process is not complete yet. After electron transfer, it is supposed to be a mechanism for the charged QDs to be neutralized and

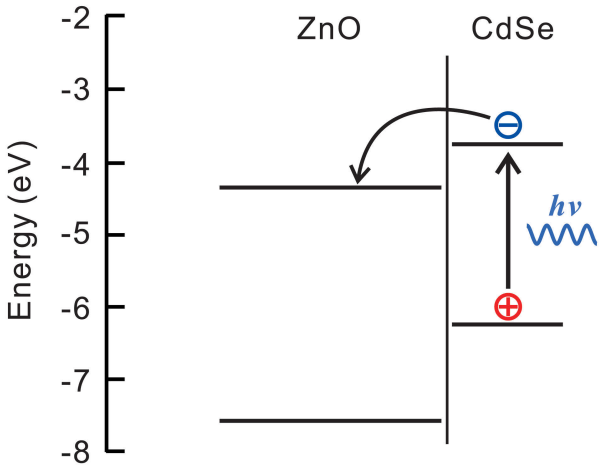

Figure 6.7: Diagram of energy levels of ZnO nanowires and CdSe QDs in absolute vacuum scale determined from the literature values [162, 163].

go back to their original states. In addition, when laser is blocked in the photoconductivity measurements, the currents reduce and return to the original values, indicating that the added conduction electrons during the irradiation stage get trapped again. Moreover, the slow PC rise and decay kinetics (in order of hours) suggests that it may be related to some slow chemical effects.

Previous studies have shown that the gas environment has significant impact on the electrical conductivity of ZnO materials, which is related to the chemisorption of gas molecules on their surfaces [95, 165, 166]. Such effect can be more significant on nanostructured materials due to their large surface-to-volume ratios. In addition, as shown in Fig. 6.5(b), the decay kinetics in air follows accurately a stretched exponential function, which is a typical behavior for the reduction of the conductivity induced by surface adsorption of gas molecules [167, 168]. Thus, the influence of gas environment on the photoconductivity of the NW/QD hybrid structure has to be examined.

6.2.2 Photoconductivity in vacuum

Figure 6.8(a) shows the photoresponse of the current of the NW/QD hybrid sample in vacuum compared with the result measured in air. The current rise and decay behaviors in these two environments are completely different. In vacuum, when laser irradiation starts, the current shows a rapid increase for a short period (less than 1 minute, see the inset). Then its increasing rate suddenly reduces to a much lower level, from more than 20 μA min^{-1} to 0.8 μA min^{-1}. This rate reduces further during measurement. It takes about 8 hours for the current to reach the steady value recorded in air.

However, further irradiation can bring the current to a higher value. After 12 hours of irradiation, the current gets to 310 μA without hints for approaching a steady state. When the laser is blocked at this point, the current decays slightly to 285 μA after 2 hours in darkness. The slow decay maintains until air is filled into the vacuum chamber, which induces a sharp decrease of the current.

In order to reach the saturation of the current in vacuum, another measurement is performed

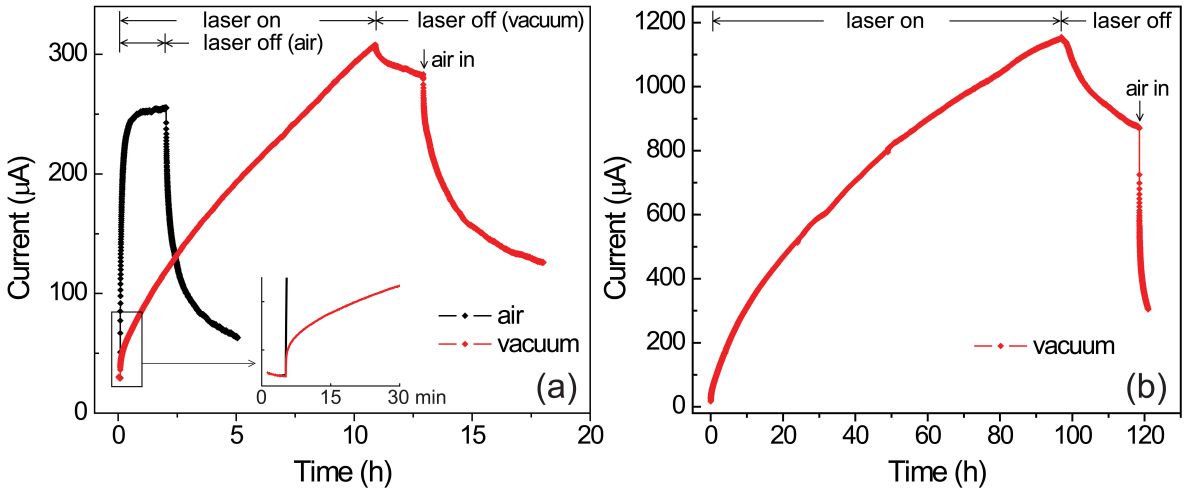

Figure 6.8: (a) Photoresponse of the current of the ZnO-NW/CdSe-QD hybrid sample measured in air and vacuum (~ 10^{-6} mbar), respectively. The inset is a magnification of the initial period of the photoconductivity enhancement. (b) Current evolution of the hybrid sample in vacuum under prolonged irradiation.

with prolonged laser irradiation, shown in Fig. 6.8(b). The overall behavior of the current is similar to that in Fig. 6.8(a). After 96 hours of irradiation, the current has increased from 28 to 1130 μA (a more than 40-fold enhancement). However, the current is still not saturated despite a further reduction of the increasing rate. These observations clearly indicate that the photoconductivity kinetics of the hybrid sample strongly depends on the gas environment, suggesting that this process is controlled by some surface effects. To examine the effects of different components of air on the photoconductivity kinetics, measurements are further performed in oxygen, nitrogen, and argon, respectively.

6.2.3 Photoconductivity in diverse gas environments

The evolution of the current under laser irradiation measured in dry oxygen is compared with that obtained in air in Fig. 6.9(a). For the measurements, the sample chamber is first evacuated and then filled with highly pure oxygen (purity of 99.9995%). The gas pressure inside the chamber is ~ 1.1 bar. The kinetics of the current increase and decay in oxygen is very similar compared to those in air. The current reaches a steady state after 30 minutes but with a smaller value of ~ 100 μA compared to 260 μA reached in air. After blocking the laser irradiation, the current reduces gradually to the original dark value. This behavior forms strong contrast with that observed in vacuum.

Figure 6.9(b) presents the photoconductivity evolutions measured in nitrogen and argon atmospheres compared with the results obtained in air and vacuum. For these measurements, a constant flow of highly pure nitrogen (99.999% with O_2 < 2.0 ppm) or argon (99.9999% with O_2 < 0.1 ppm) is applied to pass through the sample chamber. The detailed information about the experiments is described in section 4.3. It can be seen that the PC behavior in nitrogen and argon atmospheres resembles that in vacuum: the increase is rapid at first with comparable rate to that in air. After a short period (less than 1 min), the increasing rates reduces to much smaller values (2.0 μA min^{-1} in nitrogen, 1.4 μA min^{-1} in argon and 0.8 μA min^{-1} in vacuum).

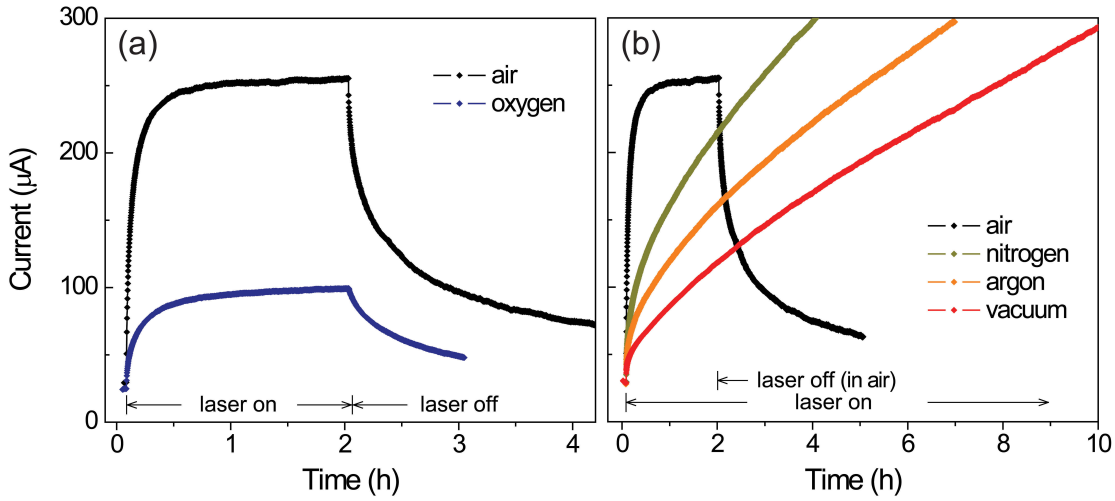

Figure 6.9: (a) Photoresponse of the current of the NW/QD hybrid sample measured in air and pure oxygen under the same laser irradiation. (b) Photoresponse of the current of the hybrid sample in air, nitrogen flow, argon flow, and vacuum. The results for air and vacuum are reproduced from the data shown in Fig. 6.8(a).

However, prolonged irradiation can result in higher currents than the maximum steady value reached in air.

Combining the above results obtained in different environments, the photoconductivity kinetics of the NW/QD hybrid structure strongly depends on the surrounding gas environment. The CdSe QDs are demonstrated to play an important role in the enhancement of the photoconductivity under laser irradiation. The evolution of the photoconductivity shows significantly different behaviors in oxygen-rich (air and pure oxygen) and oxygen-free (vacuum, nitrogen and argon) environments. This strongly indicates that oxygen in this case is the component of air that controls the PC kinetics.

6.3 Oxygen adsorption on ZnO nanostructures and CdSe quantum dots

In this section, the influence of gas molecule adsorption, with emphasis on the adsorption of oxygen molecules, on the optical and electrical properties of ZnO nanostructures and CdSe QDs is discussed.

6.3.1 Oxygen adsorption on ZnO nanostructures

Oxygen molecules are efficient electron acceptors due to their high electron affinity. They are known to be one kind of the most commonly adsorbed gas molecules on the metal oxide surface in ambient atmosphere [9,11,95]. Figure 6.10 shows a schematic of oxygen adsorption on ZnO nanowire surface. Oxygen molecules can capture electrons from the conduction bands of the oxides to form negatively charged ion species, which reduces the concentration of the conduction electrons. The oxygen ions further enhance the upward band bending and induce a

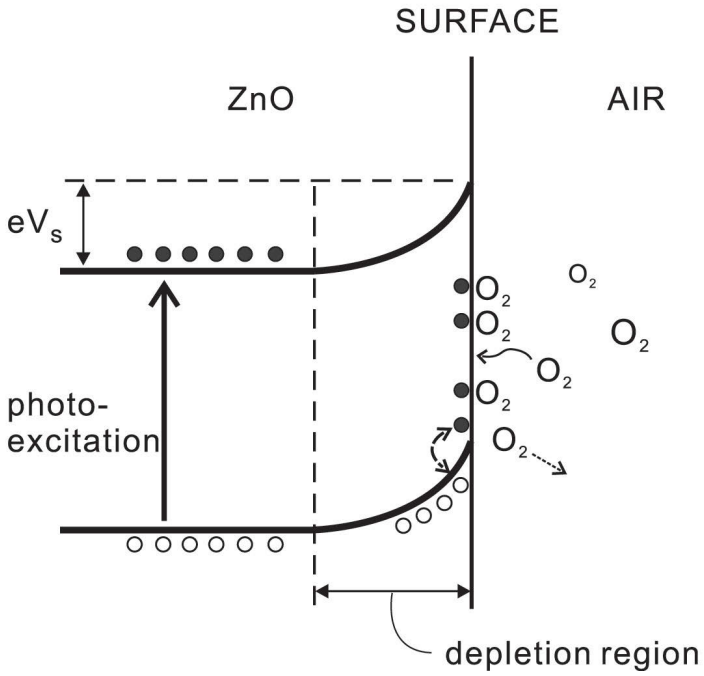

Figure 6.10: Schematic of oxygen adsorption on ZnO surface. The oxygen molecules capture electrons to form oxygen ions, inducing surface band bending and depletion layer. Under photo-excitation, the generated holes can drift to the surface and react with the oxygen ions, which converts them to be physisorbed. Afterward, they can be easily detached. In addition, ambient oxygen molecules can also be adsorbed onto the ZnO surface and capture electrons to form oxygen ions.

depletion layer in the near-surface region. As a result, the electrons are pushed to the center of the nanowire to form a narrow conduction channel. The combination of these effects reduces the conductivity of the nanowire. The width of the depletion region is given by [169, 170]

$$W = \sqrt{\frac{2\varepsilon_0\varepsilon_r V_s}{en_e}} \tag{6.3}$$

where ε_0 is the vacuum permittivity and ε_r is the relative permittivity of ZnO ($\varepsilon_r \approx 9$ [171]). n_e is the free carrier density. ZnO normally shows a n-type conductivity due to the abundance intrinsic defects like zinc interstitials and oxygen vacancies acting as donors. For pure unintentionally doped ZnO, n_e is typically in the order of 10^{17}–10^{19} cm^{-3} [172]. V_s is the surface potential corresponding to the surface band bending, as depicted in Fig. 6.10. For nanowires grown along the c-axis, their side surfaces are composed of ZnO($10\bar{1}0$) plane, for which, V_s was reported to be ~ 0.25 V [173]. Then, the depletion width is calculated using Equ. 6.3 to be in the order of 10-100 nm. The ZnO nanowires used for building the NW/QD hybrid samples have diameters in the range of 50-300 nm. Therefore, a part of them could be totally depleted in atmosphere.

The presence of surface depletion layer in nanowires decreases the conductivity G, which is described by [174]

$$G = en_e\mu\frac{\pi(R-W)^2}{L} \tag{6.4}$$

where μ is the charge mobility. R and L are the radius and the length of the nanowire, respectively. Oxygen adsorption can bring in reduced n_e and increased depletion width W, which can significantly reduces the conductivity of the nanowires.

The photoconductivity of ZnO nanomaterials has been widely studied [95, 165, 175]. Under ultraviolet light irradiation,the conductivity of ZnO significantly increases due to excitation of electron-hole pairs. However, after termination of the irradiation, the conductivity will not immediately return back to the original values but stay at a high level for quite a long time, typically in the range from several minutes to hours depending on the operating gas environment. This phenomenon was believed to be related to the photodesorption and re-adsorption of oxygen molecules on the ZnO surface.

As schematically shown in Fig. 6.10, when ZnO is photo-excited, the holes generated in the valence band can drift to the surface along the upward band bending and react with the adsorbed oxygen ions. These oxygen ions are converted to be physisorbed, which are easy to be detached from the ZnO surface. Through this process, the concentration of the free electrons is increased. Thus the conductivity of the nanowire enhances. This adsorption and photodesorption processes of oxygen molecules can be described by the equation

$$O_2 \underset{h^+\ (photodesorption)}{\overset{e^-\ (adsorption)}{\rightleftharpoons}} O_2^- \tag{6.5}$$

6.3.2 Oxygen adsorption on CdSe quantum dots

As presented in section 5.5, oxygen molecules are also commonly adsorbed on the surfaces of the MPA-capped CdSe QDs, which significantly influences their optical properties. Oxygen molecules can effectively passivate the surface defects of the QDs, which otherwise act as trap centers during photoexcitation process. These trap centers can induce charged QD core and fast non-radiative Auger-type recombinations. Therefore, the photoluminescence of the QDs exhibits severe quenching in oxygen-deficient environments. Considering the crucial role of the QDs in the photoconductivity enhancement of the NW/QD hybrid sample, the oxygen-controlled recombination process in the QDs may have essential impact on the photoconductivity kinetics.

The photoluminescence (PL) of the ZnO-NW/CdSe-QD hybrid sample is measured in air, vacuum, and nitrogen flow, respectively. The experimental setup and the gas environment conditions are the same as used in section 5.5 for the measurements of the CdSe QD powder. A 325 nm HeCd laser is used as excitation source with a laser intensity of ~ 10 mW/cm^2.

Figure 6.11(a) shows the temporal evolutions of the excitonic PL intensity of the CdSe QDs in the hybrid sample under continuous excitation. The time zero is set at the start of laser irradiation. The results are normalized to the initial values for comparison. The overall trends of the luminescence evolution for every environment are very similar to the results of the CdSe QD powder obtained in section 5.5. Those results are reproduced in Fig. 6.11(b). When measured in air, the PL of the QDs in the hybrid sample shows little decay over time (1 to 0.85 of the original value after 10 minutes), probably due to a slight degradation of the QDs. In contrast, the PL intensities in vacuum and nitrogen flow decrease significantly upon exposure to the laser light. In the first 3 minutes, the luminescence intensities reduce to 0.1 in vacuum and 0.25 in nitrogen of their initial values, respectively. As discussed above, such decrease in

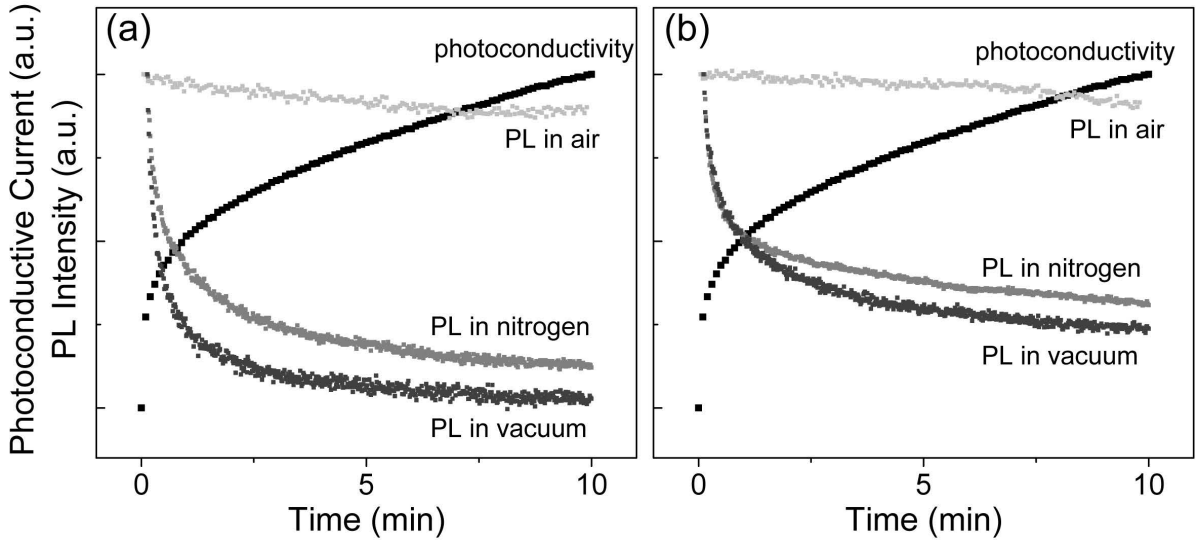

Figure 6.11: The temporal evolution of the excitonic photoluminescence (PL) intensity of the CdSe QDs in the NW/QD hybrid sample (a) and pure CdSe QD powder (b), compared with the evolution of photoconductivity of the NW/QD sample measured in vacuum. The time zero for the PL measurements is set at the start of photoexcitation. The initial PL intensities at time 0 and the maximum of the current for the photoconductivity measurments are normalized to the same magnitude while the initial value of the current normalized to zero for easy comparison.

the PL intensities is due to the activation of the surface defects of the QDs and the resulting non-radiative Auger recombination processes. In addition, it is interesting to notice that the rapid drop of the PL intensities coincides well with the sudden reduction of the increasing rate observed in the photoconductivity measured on the NW/QD sample in vacuum. This suggests that the oxygen-controlled recombination processes in the QDs may account for the unusual photonconductivity kinetics of the hybrid sample in vacuum and the inert gas environments.

6.4 Mechanism of the photoconductivity enhancement

Based on the above analysis, a model for the charge transfer in the photoconductivity process of the ZnO-NW/CdSe-QD hybrid structure is proposed and discussed in this section to explain the experimental results.

6.4.1 Operation model

Figure 6.12 shows a model of the ZnO-NW/CdSe-QD hybrid structure to illustrate the charge transfer and surface oxygen desorption processes in the photoconductivity measurements. Part (a) illustrates the oxygen adsorption on the nanowire and QD surfaces in the ambient atmosphere. The conductivity of the nanowire lies at a low level due to the decrease in the concentration of the conduction electrons and the presence of a surface depletion layer induced by oxygen adsorption. The surface defects of the QDs are passivated by oxygen molecules.

Photoconductivity in oxygen-rich environments

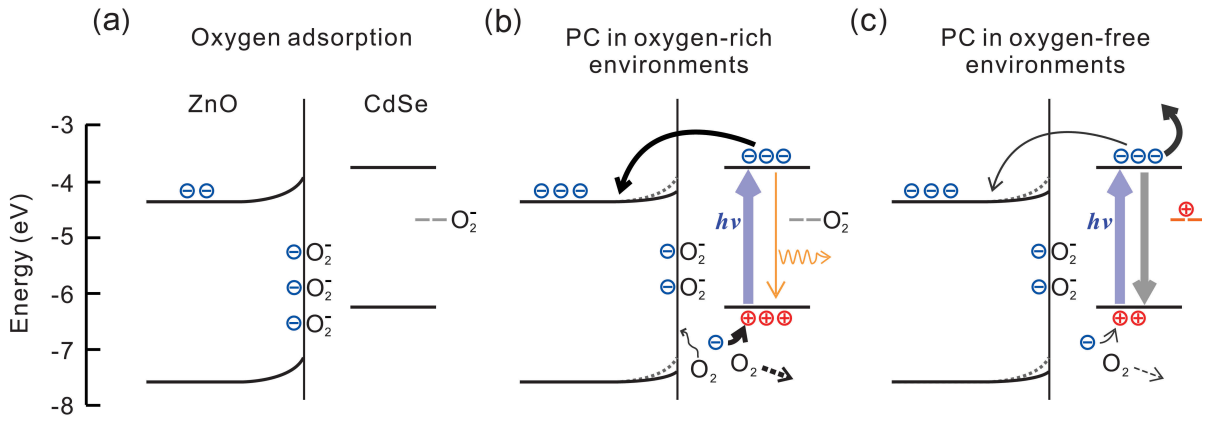

Figure 6.12: (a) Oxygen adsorption on the NW/QD hybrid structure in air. Oxygen ions on the nanowire surface induce upward band bending and depletion layer. Oxygen adsorbed on the QD surface passivates their surface defects. (b) Charge transfer and oxygen desorption in the photoconductivity (PC) process in oxygen-rich environments. Surface defects of CdSe QDs are kept passivated by the quick compensation of ambient oxygen. Oxygen adsorbates on the nanowire surface are gradually desorbed by the photogenerated holes in the CdSe QDs. The free electron concentration in the ZnO nanowire increases while the band bending is relaxed due to the removal of oxygen ions. (c) Charge transfer and oxygen desorption in the PC process in oxygen-free environments. Detachment of oxygen from the QD surface results in active surface defects and quick Auger recombination processes, which competes with the charge transfer between the QD and the NW, inducing slow oxygen desorption from the NW surface.

In an oxygen-rich environment (air or pure oxygen in the present work), when the hybrid structure is irradiated with an argon laser, electron-hole pairs are created in the CdSe QDs (Fig. 6.12(b)). The electrons can transfer into the conduction band of the ZnO nanowire. On the other hand, the photogenerated holes can react with the oxygen ions adsorbed on the nanowire and QD surfaces, which can desorb them freely. However, the QDs can remain passivated due to the quick re-adsorption of the ambient oxygen molecules, which is reflected by the stable PL of the QDs in air shown in Fig. 6.11(a). With respect to the ZnO nanowires, the oxygen re-adsorption seems relatively slow compared to that occurring on the QD surface. The total effect is that the electrons trapped by oxygen ions on the nanowire surface tunnel into the valence band of the QD. They can be excited with the argon laser and then transfer back to the conduction band of ZnO. In this process, the QD stays electrically neutral. It acts as photocatalyst for oxygen desorption from the nanowire surface by providing holes. As a result, the free electron concentration in the nanowire increases and the removal of oxygen ions further reduces the width of the depletion layer, inducing the enhancement of the conductivity. This can explain the rapid current rise observed in air and oxygen shown in Fig. 6.9(a).

As this process proceeds, more and more oxygen adsorbates are removed from the nanowire surface while more free surface sites are created. Therefore, the rate of oxygen desorption-gradually decreases and that of the oxygen re-adsorption increases. Ultimately, an equilibrium between these two effects is reached and the density of the surface oxygen on the nanowire remains steady afterwards. This corresponds to the observed saturation of the current in Fig. 6.9(a). When measured in pure oxygen, due to the larger oxygen partial pressure rela-

tive to air, oxygen is more probable to be re-adsorbed, inducing a lower extent of the surface oxygen desorption under equilibrium. Thus the steady current observed in pure oxygen is lower than that reached in air. When the laser irradiation is blocked, the ambient oxygen molecules are gradually adsorbed onto the nanowire surface. The system slowly returns back to the original state accompanied with the drop of the conductivity of ZnO nanowires.

Photoconductivity in oxygen-free environments

When the photoconductivity measurements are performed in oxygen-free environments (vacuum, argon and nitrogen flows), the situation is different. After desorption from the nanowire or the QD surface, oxygen molecules will be carried away immediately by either vacuum pumping or the inert gas flow. Thus, ideally, no oxygen re-adsorption occurs during irradiation. This can induce profound change in the charge relaxation dynamics of the QDs. According to the observed PL quenching of the CdSe QDs in Fig. 6.11, the oxygen molecules on the QD surface can be removed in less than 1 minute under laser irradiation. Within this minute, most of the QD surface defects are still passivated by oxygen molecules. Photogenerated holes can quickly react with the surface oxygen ions of the nanowire and detach them. After nearly all the oxygen adsorbates are removed from the QD surface, the active defects act as trap centers and induce fast Auger-type recombinations in the QDs in which the excited electrons quickly relax to the valence band by transferring their energies to the additional charge carriers (Fig. 6.12(c)). Therefore, the rate of the electron transfer from the QD to the nanowire and the oxygen desorption from the nanowire surface are significantly reduced, resulting in the abrupt decrease in the increasing rate of the current (Fig. 6.9(b)). However, as there is no re-adsorption of oxygen occurring, ideally, all oxygen adsorbates on the nanowire surface can be removed ultimately under sufficient long laser irradiation. Therefore, higher currents can be expected for prolonged irradiation.

The deviation in the increasing rates of the current in vacuum, nitrogen, and argon can be explained as follows: first, in the photoconductivity measurements the sample was covered with another piece of FTO glass, which was unfavorable for the inert gas flow to reach the sample surface and drive the desorbed oxygen away. As a result, they were probably readsorbed by the QDs. Besides, there are still small oxygen components contained in the inert gases ($O_2 < 2.0$ ppm for nitrogen and $O_2 < 0.1$ ppm for argon). The argon gas has higher purity. Thus the current behavior observed in argon flow is more approximate to that in vacuum.

6.4.2 Charge transfer rates

The operation rates of the above charge transfer and oxygen desorption model are further discussed in this subsection.

Figure 6.13 comprehensively shows the possible charge transfer and relaxation processes, and the oxygen desorption and adsorption events occurring in the photoconductivity measurements of the NW/QD hybrid structure. The energy levels of the CdSe QDs are discrete with a large spacing due to the strong quantum confinement effect on the motion of the charge carriers, as described in section 2.4. The level spacing is generally on the order of tens to hundreds of meV. Under the irradiation of the argon ion laser, electron-hole pairs are quickly generated in the CdSe QDs. After the carriers are excited to higher levels, their thermalization to the band edges could be very slow due to the much larger level spacing relative to the energy of

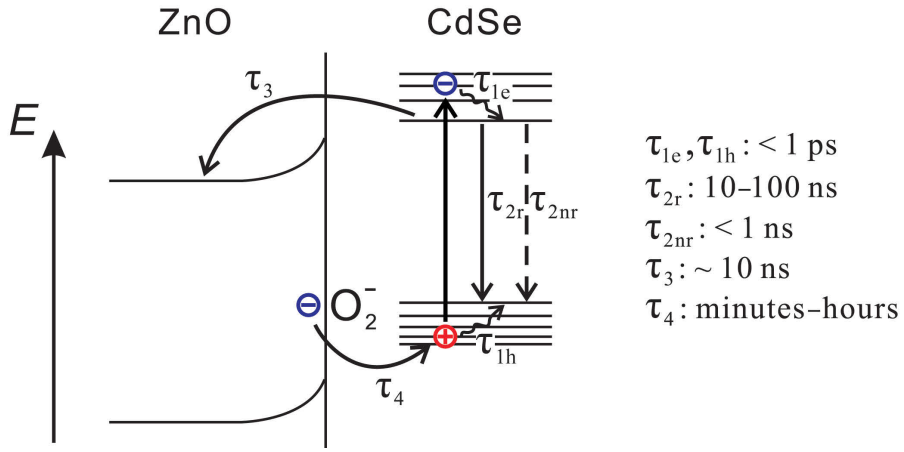

Figure 6.13: Schematic for illustrating the operation rates of charge transfer and reaction in the photoconductivity processes of ZnO-NW/CdSe-QD hybrid structures.

longitudinal optical (LO) phonon in CdSe (25 meV [60]), referred to as a phonon bottleneck phenomenon (see section 2.4.4). However, fast subpicosecond thermalization processes of the hot carriers (τ_{1e} and τ_{1h}) are commonly observed in QDs [176], which can be helped by the defect states located between the electron and hole levels [59]. In addition, hot carriers could also transfer their energies to the high frequency vibrations of the capping ligand molecules of the QDs [59].

As discussed above, the band-edge recombination of the electron-hole pairs in the CdSe QDs has two types. One is the radiative neutral exciton recombination with a lifetime τ_{2r}. The other is the non-radiative Auger recombination with significantly shortened lifetime τ_{2nr}, induced by charge trapping of the surface defects of the QDs. This has been already discussed in section 5.5. τ_{2r} is typically in the order of several tens of nanoseconds for colloidal CdSe QDs while the τ_{2nr} is generally one order of magnitude smaller than it or even less [155].

The excited electrons could transfer into the conduction band of the nanowire. The driving force for this process is the energy difference between the conduction band positions of the QD and the nanowire. For CdSe QDs functionalized ZnO nanostructures, the time constant τ_3 for electron injection from the QDs into ZnO was reported to be on the order of 10 ns, which further depends on the size of the QDs and their capping ligands [177, 178]. This is comparable to the neutral exciton lifetime in the QDs and slower than the nonradiative Auger-type recombination processes. Therefore, when performing the photoconductivity measurements in oxygen-free environments, the triggered Auger recombinations in the CdSe QDs can efficiently compete with the charge transfer between the QDs and the nanowires, inducing the observed slow photoconductivity enhancement.

In addition, according to the observed slow PC rise and decay dynamics, the time constant τ_4 for oxygen desorption and adsorption onto the ZnO surface could be on a time scale of minutes or even hours. Using the fitting parameters obtained in Fig. 6.5(b), the mean time constant for the stretched exponential decay of the current of the NW/QD hybrid sample is given by

$$\langle \tau \rangle = \frac{\tau}{\alpha} \Gamma \left(\frac{1}{\alpha} \right) \tag{6.6}$$

$\langle \tau \rangle$ is calculated to be 82 minutes for the PC decay in air. This slow chemical surface process

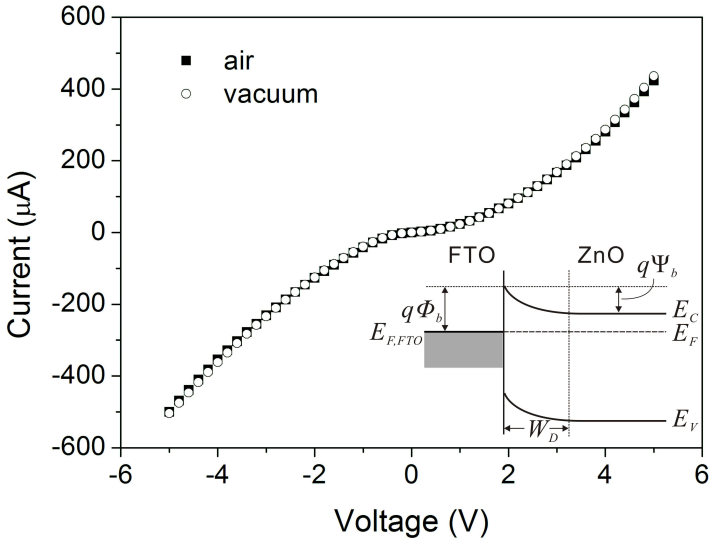

Figure 6.14: I-V curves of the ZnO-NW/CdSe-QD hybrid sample in air and vacuum measured in darkness. Inset: schematic of Schottky contact between FTO glass and ZnO nanowires.

should be the main limiting factor for the rates of the PC enhancement and decay dynamics in the NW/QD hybrid sample.

6.4.3 The effect of Schottky contacts

In this subsection, the effect of Schottky contacts between the FTO glass and the ZnO nanowires on the photoconductivity properties of the hybrid sample is analyzed. Considering a larger work function of the FTO (ϕ_{FTO} = 4.4 – 5.0 eV [179, 180]) relative to the electron affinity of ZnO (χ_{ZnO} = 4.2 eV [163]), Schottky-type contacts are actually formed between the tips of the ZnO nanowires and the FTO glass sheets (both the nanowire substrate and the top contacting glass sheet). In this case, the conduction electrons in ZnO will flow into the FTO layer. As a result, a build-in electric field is formed pointing from ZnO to the FTO, which lowers the Fermi level in ZnO relative to that in FTO by an amount equal to the difference between their work functions. At thermal equilibrium, the Fermi levels on both sides will line up and a potential barrier is formed at the interface with a depletion area formed on the semiconductor side due to its limited availability of free electrons. The inset of Fig. 6.14 shows a schematic of the Schottky contact at the FTO and ZnO interface. Ideally, the barrier height is the difference between the FTO work function ϕ_{FTO} and the electron affinity of ZnO χ_{ZnO}, as $\phi_b = \phi_{FTO} - \chi_{ZnO}$. The width of the depletion area formed in ZnO is given by [169]

$$W_D = \sqrt{\frac{2\varepsilon\varepsilon_0\Psi_b}{en_e}} \tag{6.7}$$

where $\Psi_b = \phi_{FTO} - \phi_{ZnO}$ is the barrier height on the semiconductor side. ϕ_{ZnO} is the work function of ZnO.

The contact barrier can introduce an extra resistance in the circuit. When a bias voltage is applied between the two FTO glass sheets, the Schottky contacts on one side of the nanowires will be in a forward bias mode while those on the other side are in a reverse bias mode. As

a result, the current-voltage (I-V) dependence of the hybrid sample is characterized with non-linear symmetrical curves. Figure 6.14 shows the current-voltage dependence measured in darkness in air and vacuum, respectively, indicating the formation of Schottky contacts. In some previous works about metal-ZnO-metal configured devices, ultraviolet light illumination was fount to significantly affect the Schottky contacts at the metal/ZnO interface [181–183]. The photoexcited electrons increase the concentration of the free electrons, which can reduce the width of the depletion area near the contact according to Equ. 6.7. Additionally, the holes in the valence band of ZnO can follow the upward band bending and accumulate at the metal/ZnO interface, which further lowers the barrier height [182]. As a result, the charge carriers become more likely to transit over the lowered contact barrier or directly tunnel through the depletion region, which decreases the contact resistance.

However, this effect seems to be very limited in the present work. First, the use of 458 nm laser light excites electron-hole pairs not directly in the ZnO nanowires, but in the CdSe QDs. The photogenerated holes will therefore be located inside the QDs, and no hole accumulation occurs at the FTO/ZnO interface. Secondly, the increase of the free electron density in the nanowires is mostly due to oxygen desorption and electron transfer from the QDs to the nanowires. It is not so efficient like that using direct UV excitation. Furthermore, in the photoconductivity measurements, even after a long time of irradiation, the I-V relation curves still show clear Schottky behaviors, illustrating that the contact resistance is not eliminated effectively. Therefore, the observed photoconductivity enhancement in the NW/QD hybrid sample is mostly attributed to the increase of the conductivity in the ZnO nanowires.

Ohmic contacts on single ZnO nanowire

As described in Equ. 6.7, the increase of the free charge carrier density can narrow the depletion width and hence reduce the contact resistance. Gallium (Ga) doping was found to act as electron donors in ZnO and was demonstrated to be a proper impurity for fabrication of ohmic contact for ZnO [184, 185]. Using preceding Ga^+ implantation, a high quality ohmic contact between platinum (Pt) electrode and unintentionally doped ZnO nanowire is obtained.

ZnO nanowires are grown by thermal chemical vapor deposition (CVD) method in the group of Prof. C. Ronning at the Institute of Solid State Physics, Universität Jena. The growth method is introduced in section 4.1.2. The nanowires are dispersed onto an oxidized silicon wafer with pre-patterned Ti/Au electrodes. For Ga doping, Ga^+ ions are implanted into the ends of the nanowire. The Ga^+ implantation and the deposition of Pt stripes are performed using a FEI Dual-Beam NOVA 600 FIB/SEM instrument equipped with a trimethylcycloentadienyl-platinum injector. The accelerating voltage for Ga^+ implantation is 30 keV with a flow current of 1 pA. The implanted dose is 10^{16} cm^{-2}. Afterwards, Pt stripes are deposited to connect the ends of the nanowire to the Ti/Au electrodes. The inset of Fig. 6.15 shows a SEM image of the contacted ZnO nanowire. The nanowire has a diameter of 94 nm with the connecting length between those two Pt stripes of 12.5 μm. Figure 6.15 shows the I-V relation measured using a Keitheley 2400 Souremeter. The I-V curve shows an excellent linear dependence, demonstrating the fabricated Pt-ZnO ohmic contacts. The resistance of the nanowire is given by

$$R = \frac{V}{I} = \frac{l}{\sigma A} \tag{6.8}$$

$$\sigma = ne\mu \tag{6.9}$$

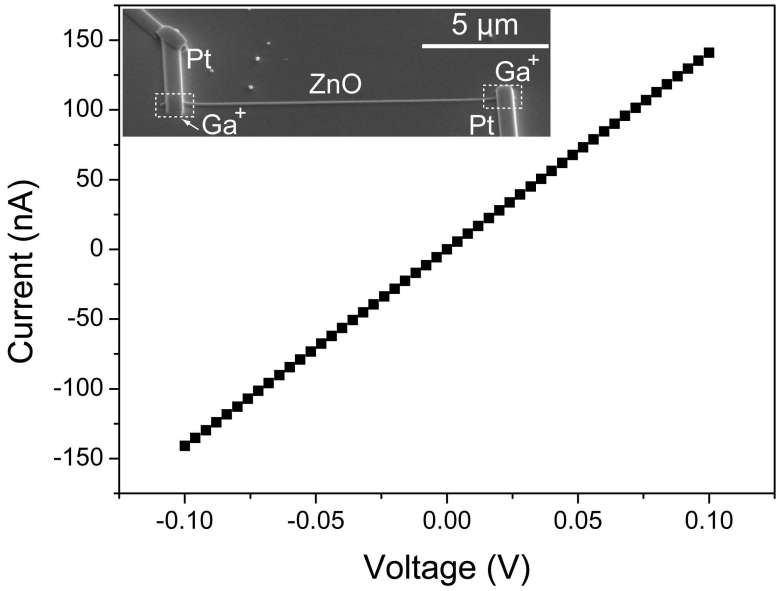

Figure 6.15: The current-voltage (I-V) relation of a Pt-ZnO-Pt contacted single ZnO nanowire measured in darkness. The inset is a scanning electron microscope (SEM) image of the nanowire. The areas marked with dashed rectangles are treated with gallium ions implantation before deposition of the Pt stripes.

where l and A is the connecting length and the cross section area of the nanowire, respectively. σ is the conductivity of the nanowire, n is the electron density, and μ is the electron mobility. Using previously reported electron mobility of $\mu \approx 20$ cm^{2}V^{-1}s^{-1} [9, 11], the electron density n of the ZnO nanowire is calculated to be 8×10^{18} cm^{-3}, which agrees well in order with the literature values [186].

6.5 Summary

In this chapter, hybrid nanostructures are fabricated by the surface functionalization of ZnO nanowires with colloidal CdSe QDs. The QDs are synthesized by a wet chemical method. They are stabilized with a layer of bifunctional 3-mercaptopropionic acid molecules. These stabilizer ligands can act as molecular linkers to bind the QDs on the ZnO nanowire surface. Optical and electron microscopy measurements demonstrate the dense attachment of the CdSe QDs.

The photoconductivity (PC) of the nanowire/quantum-dot (NW/QD) hybrid samples is investigated in air, dry oxygen, vacuum, nitrogen, and argon, respectively. An argon ion laser operating at 458 nm is chosen as excitation source, which exclusively excite the CdSe QDs. The photoresponse of the electrical conductivity of the NW/QD hybrid structure is measured, which allows a convenient investigation of the internal charge transfer mechanism. Under laser irradiation, the photoconductivity of the hybrid sample is observed to increase dramatically ($\sim$ 10 times increase observed in air), which can restore to the initial value after termination of irradiation. However, the rise and decay kinetics of the photoconductivity strongly depend on the gas environments. It exhibits two kinds of essentially different PC kinetics observed in oxygen-rich (air and dry oxygen) and oxygen-free (vacuum, nitrogen and argon) environments,

respectively. These observations point to an oxygen-controlled surface effect dominating the photoconductivity behaviors.

A model is proposed to explain the experimental results. In darkness, oxygen molecules are densely adsorbed on ZnO surface. They capture electrons to form oxygen ions, resulting in reduced conduction electron concentration, upward surface band bending, and surface depletion layers. The combination of these effects reduces the conductivity of the nanowires. With photoexcitation of the CdSe QDs, electron-hole pairs are generated. The electrons can transfer into the ZnO nanowires while the holes can react with oxygen ions on the nanowire surface and detach them. This results in the observed photoconductivity enhancement. However, as demonstrated by photoluminescence measurements, the charge relaxation dynamics in CdSe QDs is very sensitive to gas environment due to the important role of oxygen in their surface passivation. The adsorption of oxygen molecules on the QD surface can effectively passivate their surface defects. In oxygen-free environments, the unpassivated surface defects act as trap centers which would induce fast Auger recombination of the electron-hole pairs. This process can strongly compete with the charge transfer between the QDs and the nanowires, thus inducing the much slower photoconductivity enhancement. This model can well explain the experimental observations. In addition, the conductivity decay process in air is found to follow a stretched exponential behavior, which is consistent with previous studies on surface-oxygen-controlled conductivity in ZnO nanomaterials, providing further support for the present model.

The effect of the Schottky contacts formed between the ZnO nanowires and the FTO coated glass sheets on the experimental results is further analyzed, which is believed to be very limited due to the selective excitation of the CdSe QDs during the PC measurements. In addition, by means of preceding gallium ions implantation, ohmic contacts between ZnO nanowires and platinum are obtained, demonstrated by I-V dependence measurements.

This work presents a simple method for surface functionalization of ZnO nanowires with colloidal semiconductor QDs, which can be easily extended to other materials. The photoconductivity measurement can be used as a convenient method for investigating the charge transfer in QD-sensitized nanomaterials. The experimental results can help the understanding of the charge transfer and interaction processes in the ZnO-NW/CdSe-QD hybrid system which has potential applications as photodetecting and photovoltaic devices. The strong influence of oxygen on the photoconductivity kinetics of the hybrid sample further illustrates the importance of a carefully controlled surface termination of nanostructured devices for optimized performance.

Chapter 7

Excitation Intensity Dependence of the Photoluminescence Properties of ZnO

Photoluminescence spectroscopy is a commonly used characterization technique for semiconductor materials. The spectra generally consist of a near-band-edge emission band due to interband recombinations and one or multiple deep-level related emission bands originating from recombination processes involving defect centers. The photoluminescence properties of semiconductors have been found to be excitation-intensity-dependent [90, 91, 187]. When the excitation intensity becomes stronger, not only the overall emission intensity increases but also the relative strength between different emission bands will change.

In this chapter, the excitation intensity dependence of the photoluminescence properties of ZnO is studied. The investigated samples include ZnO nanowires grown by chemical vapor deposition (CVD) as well as commercial ZnO wafers grown by a hydrothermal method. Their photoluminescence properties are studied with a wide range of excitation intensities at room and low temperatures.

In the first section, the basic photoluminescence properties of CVD-grown ZnO nanowires are presented. The origins of their near-band-edge emission and deep-level emission are analyzed in the second section with low temperature measurements. In the third part, the excitation intensity dependence of the photoluminescence properties of ZnO nanowire and wafer samples is investigated. After that, a theoretical model is proposed and discussed in the linear optical regime to explain the experimental results. Then, the excitation intensity dependence of the photoluminescence is further investigated at low temperature. The last section summarizes the results obtained in this chapter.

7.1 Basic photoluminescence properties of ZnO nanowires grown by chemical vapor deposition

The basic photoluminescence properties of ZnO nanowires grown by chemical vapor deposition (CVD) are presented in this section. The growth is based on a Au-catalyzed vapor-liquid-solid (VLS) process. The growth method is described in section 4.1.2. The prepared nanowires have an average diameter around 100 nm and lengths ranging from 10 to 100 μm.

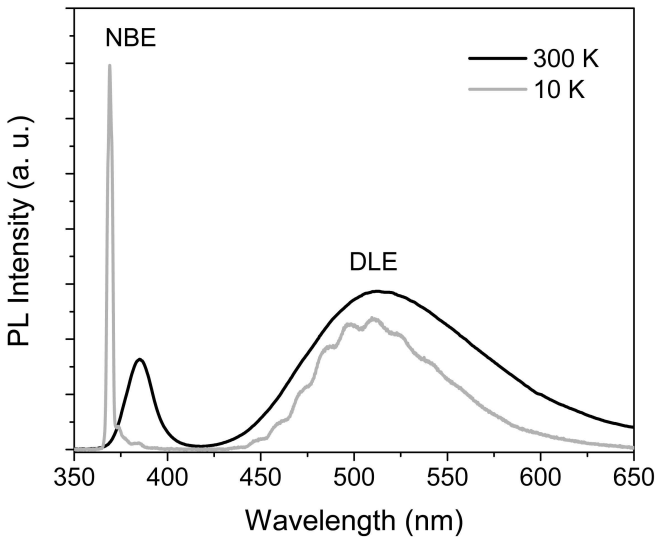

Figure 7.1: Photoluminescence spectra of VLS-grown ZnO nanowires at room temperature and 10 K. A 325 nm HeCd laser is used as excitation source. The spectra have two main emission bands: a near-band-edge emission band (NBE) in the ultraviolet region and a deep-level emission band (DLE) in the visible spectral region.

Figure 7.1 shows the typical photoluminescence spectra for VLS-grown ZnO nanowires at room temperature and low temperature (T = 10 K), respectively. The spectra have two main emission bands: a narrow ultraviolet (UV) emission band and a broad visible emission band. The UV band is mainly arising from band-edge recombination processes of excitons and their phonon replicas, thus referred to as near-band-edge emission (NBE). ZnO has a high exciton binding energy (~ 60 meV), which is about 2.4 times larger than the thermal energy at room temperature (25 meV). This results in efficient excitonic luminescence of ZnO at room temperature. The NBE band peaks around 385 nm at room temperature with a band width of ~ 18 nm (142 meV). When going to low temperature (gray line in Fig. 7.1), the emission shifts to shorter wavelength (~ 370 nm) due to the temperature dependence of the band gap.

The broad visible emission bands in Fig. 7.1 are, in general, related to recombinations via deep levels in the band gap of ZnO induced by defects or impurities, and are referred to as deep-level emission (DLE). The band maximum is around 510 nm at room temperature and shifts to 506 nm (2.45 eV) at 10 K. The low temperature spectrum further shows multiple peaks. Such a so-called green band is commonly observed in ZnO prepared by different methods. The origins of the NBE and DLE are further discussed in the following section.

7.2 Origins of the band-edge and deep-level emissions of ZnO nanowires

In this section, the microscopic origin of the photoluminescence of the ZnO nanowires is discussed. The NBE is first investigated with high resolution photoluminescence spectroscopy. The experimental setup is illustrated in section 4.4.1. Temperature-series measurements of the NBE are performed to ascertain its luminescence origin at room temperature. The DLE is discussed in the second part.

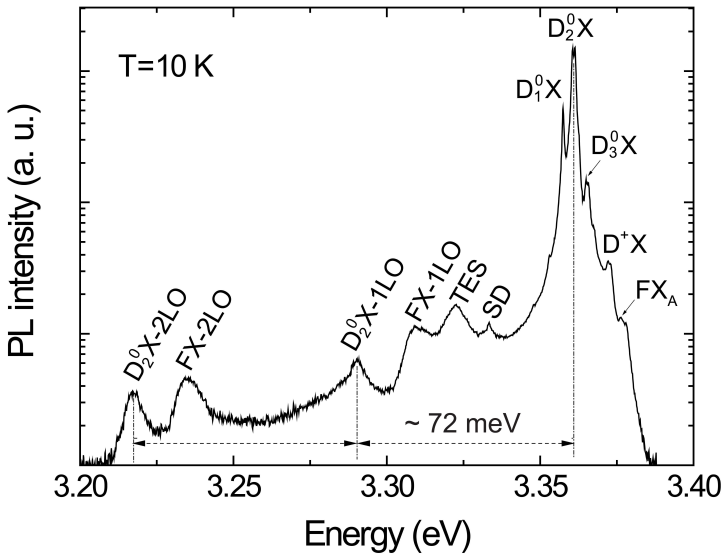

Figure 7.2: High resolution spectrum of the NBE band of VLS-grown ZnO nanowires at 10 K.

7.2.1 Band-edge emission

As stated above, the NBE band of ZnO mostly consists of exciton emission and its phonon replicas. Excitons are formed due to the strong Coulomb attraction between electrons and holes. These excitons can move through the material and encounter a trap center. It may give rise to either deep-level luminescence or generate a bound exciton complex. The recombination of the free and bound excitons and their coupling with phonons constitute the main part of the NBE of ZnO.

Figure 7.2 shows a high resolution NBE spectrum of VLS-grown ZnO nanowires measured at 10 K. The spectrum has rich features. The assignment of the emission peaks to different optical transitions is achieved by comparing their energy positions with previously reported values [38]. The peak labeled as FX_A at 3.3763 eV is attributed to recombination of free A-excitons. The energy position agrees well with the literature values measured on high quality ZnO single crystals [19, 38]. The emission from free B-excitons and C-excitons that should appear at higher energy positions (around 3.3834 eV and 3.4223 eV, respectively, according to the literature [188, 189]) cannot be recognized in the present spectrum.

ZnO is an intrinsically n-type doped semiconductor due to the presence of abundant intrinsic defects, like Zn interstitials or O vacancies formed during growth which act as electron donors. At low temperature, excitons can be efficiently bound to these defect centers with binding energies from several to several tens of meV. Thus, the donor bound exciton recombination processes normally dominate the low temperature NBE of ZnO. The spectrum in Fig. 7.2 has three prominent peaks at 3.3575 eV, 3.3606 eV and 3.3649 eV, labeled as D_1^0X, D_2^0X and D_3^0X, respectively. They are attributed to excitons bound to three kinds of neutral donors. However, the assignment of these peaks to specific chemical species of donors is difficult due to the sensitivity of the donor concentration and their capture cross section to the growth method and conditions. The peak located at a slightly higher energy position of 3.3722 eV is assigned to ionized donor bound exciton (D^+X) [190]. The emission peak at 3.3334 eV, labeled as SD, is attributed to the recombination of excitons trapped by structural defects in ZnO nanowires [38].

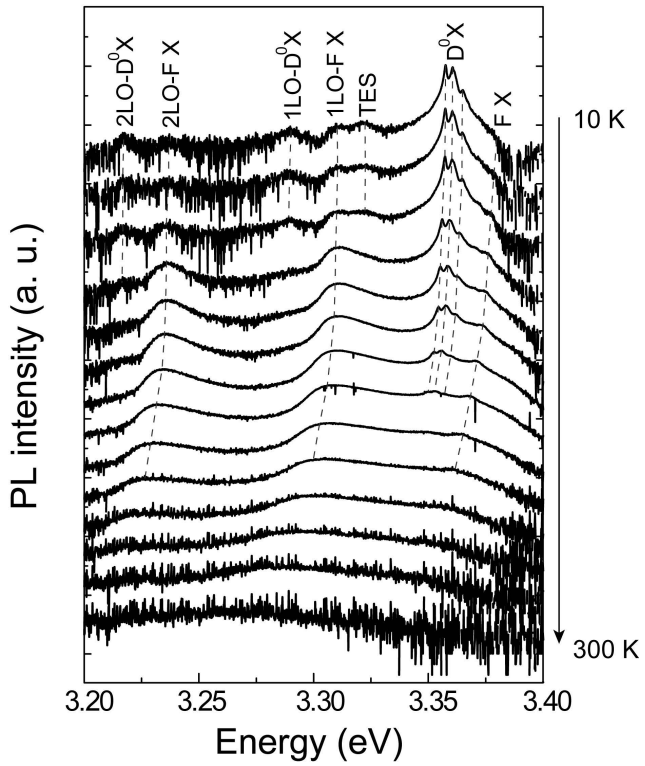

Figure 7.3: Evolution of the high resolution near-band-edge emission of VLS-grown ZnO nanowires with temperature increasing from 10 K to 300 K. The dashed lines are visual guides for the shifts of the emission bands.

During the recombination of a neutral donor bound exciton, the final state of the donor can be its ground state or an excited state, corresponding to the normal D^0X emission and its two electron satellite (TES) emission with lower energy, respectively. The energetic distance between the D^0X and its TES is consequently the difference between the energies of the ground state and the final excited state of the donor. The emission peak observed at 3.323 eV in Fig. 7.2 is attributed to a TES emission of the prominent D^0X line.

Due to its high ionicity of 0.62, ZnO has strong exciton-phonon interaction [19, 191]. In Fig. 7.2, the first order and second order longitudinal optical (LO) phonon replicas of the free exciton are observed at 3.309 eV (FX-1LO) and 3.235 eV (FX-2LO), respectively. This assignment is also confirmed by the temperature-series measurements discussed later. The first and second LO phonon replicas of the dominant D^0_2X states are located at 3.290 eV (D^0_2X-1LO) and 3.218 eV (D^0_2X-2LO), respectively, with their energy distance close to the LO phonon energy of 72 meV in ZnO.

To determine the NBE origin of the ZnO nanowires at room temperature, photoluminescence measurements were performed with increasing temperature from 10 K to 300 K to track the evolution of the luminescence spectra. The results are shown in Fig. 7.3. As the temperature increases, all resolved emission lines in the NBE band shift gradually to lower energies, due to the narrowing of the band gap. The dependence of the band gap energy of a semiconductor

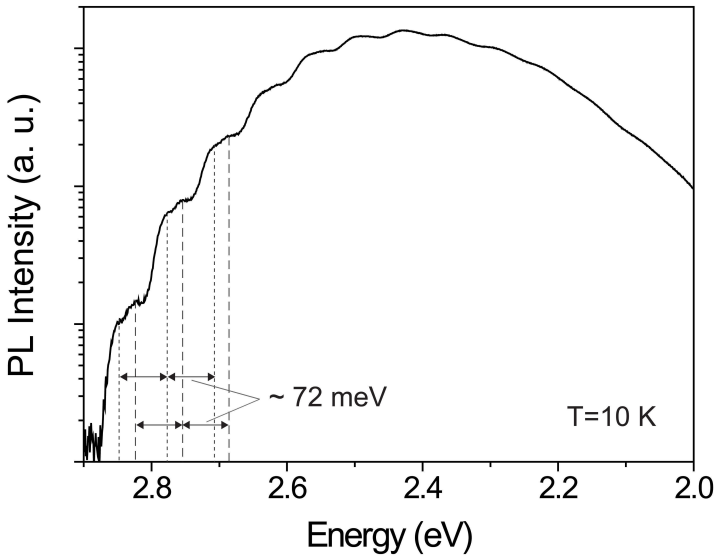

Figure 7.4: DLE spectrum of VLS-grown ZnO nanowires at low temperature (10 K). The energy spacing between the emission peaks is around 72 meV. These peaks are attributed to various-order longitudinal optical (nLO) phonon replicas of two emission lines resolved at 2.8470 eV and 2.8222 eV.

on temperature can be described by the phenomenological Varshni formula [192]

$$E_g(T) = E_g(0) - \frac{\alpha T^2}{\beta + T} \tag{7.1}$$

where $E_g(0)$ is the band gap at 0 K, T is the temperature, and α and β are material specific fitting parameters.

When the temperature increases, the luminescence intensities of the donor bound exciton and their TES and phonon replicas gradually weaken and finally become undetectable, as a result of the dissociation of the donor bound exciton complexes. On the other hand, the free exciton emission and its phonon replicas become stronger with increasing temperature due to the increase in the density of the free excitons. In addition, these changes are accompanied by a broadening of the emission lines. Ultimately, the free exciton and its phonon replicas merge together, comprising the NBE band at room temperature.

7.2.2 Deep-level emission

The broad luminescence bands of ZnO observed in the visible and infrared spectral regions are generally related to recombination via deep levels inside the band gap. These levels could be induced by impurity atoms such as Cu, Fe, and Li, and intrinsic defects such as zinc interstitials and oxygen vacancies [19]. Different deep centers will give rise to emission bands with different characteristics, like the band position and the features at low temperatures. However, there is still a wide controversy in literature about the assignment of DLE bands in ZnO. In this subsection, the possible origin of the DLE in the VLS-grown ZnO nanowires used in this work is discussed.

Figure 7.4 shows a DLE spectrum of the ZnO nanowires recorded at 10 K. The spectrum

exhibits multiple emission peaks with its band maximum at 2.45 eV, corresponding to a so-called green band that is commonly observed in many types of ZnO materials. The energy spacing between these peaks roughly equals to the LO phonon energy of ZnO (72 meV), indicating that these peaks originate from different phonon replicas of specific defect related transitions. The two emission lines at the highest energy position resolved in the spectrum are located at 2.8470 eV and 2.8222 eV, respectively.

The origin of such a green emission band in ZnO is still controversially discussed in literature. Oxygen vacancies (V_O) have be assumed for many years as one of the origins since the work of Vanheusden in 1996 [170]. The DLE was attributed to transitions from the deep donor level of V_O to the valence band. However, recent studies provide more support to the assignment to copper impurities that may be introduced during ZnO growth, which was ever proposed in early studies [193–195]. Copper impurities have been found to induce two types of acceptor states, the high lying ground Cu^{2+} state (190 meV below conduction band) and the excited Cu^{+} states. The green emission band was attributed to the internal transition between these two ground and excited Cu acceptor states [193]. At low temperatures, the emission was fount to show a multiple-peak featured spectrum, which was thought to be a characteristic of the copper related emission band [193]. However, the reported energy of the zero phonon line is 2.8590 eV, which has around 12 meV difference with our observation. Moreover, the introduction of copper impurities during the CVD growth of the nanowires seems also very unlikely considering the high purity (99.9%) of the used ZnO source powder. In addition, the DLE band at low temperature undergoes a blueshift relative to the room temperature emission. This suggests that the DLE may be related to a transition process from the band edge. Therefore, the assignment of the present green band is still an open question.

7.3 Excitation-intensity-dependent photoluminescence of ZnO

In this section, the excitation intensity dependence of the photoluminescence properties of the VLS-grown ZnO nanowires as well as commercial ZnO wafers grown by hydrothermal method are studied. The experimental setup is illustrated in section 4.4.2. The ZnO samples are non-resonantly excited with a 325 nm HeCd laser with its photon energy equal to 3.8 eV, which is well above the band gap of ZnO (3.37 eV at room temperature [27]). The laser spot on the samples has a diameter around 30 μm. The laser power intensity is adjusted with a neutral filter to vary in the range from 10^{-1} to 10^{3} W/cm^2. The photoluminescence spectra are recorded using an Avantes 2048TEC fiber spectrometer. The measurements are performed at room temperature.

7.3.1 Chemical vapor deposition grown ZnO nanowires

Figure 7.5(a) shows the photoluminescence spectra of the ZnO nanowires for different excitation intensities. The relative peak intensity between the NBE and DLE bands varies significantly with the excitation intensity. Under low excitation intensities, the DLE dominates the luminescence spectrum. With increasing laser intensity, the NBE emerges and increases quickly relative to the DLE. When the laser intensity rises from 0.3 to 936 W/cm^2, the peak intensity ratio between the NBE and DLE bands increases from 0.01 to 12, i.e. a variation of

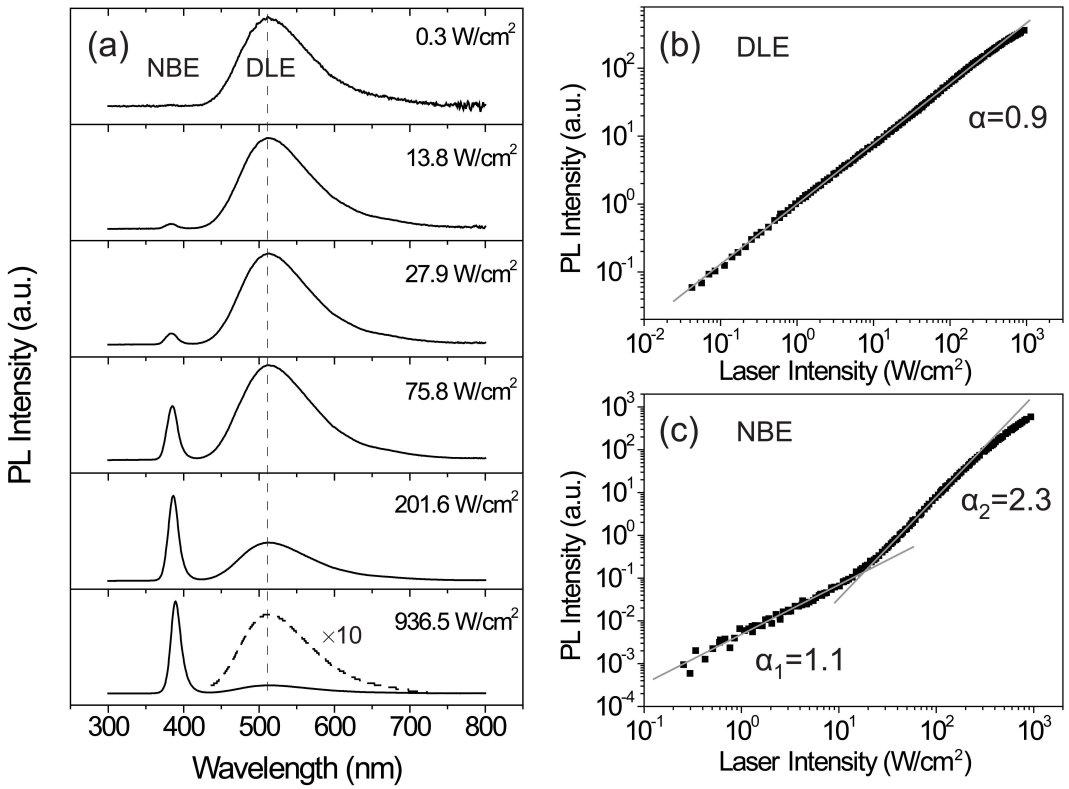

Figure 7.5: (a) Photoluminescence spectra of ZnO nanowires under different excitation intensities. (b) Integrated DLE of ZnO nanowires as a function of excitation intensity. (c) Integrated NBE of ZnO nanowires as a function of excitation intensity. The solid lines are plotted for visual guides. α is the slope of the lines.

more than three orders of magnitude. On the other hand, the band maximum positions and the band widths have no obvious change under different excitation intensities.

The evolutions of the integrated DLE and NBE intensities as a function of laser intensity are presented in Fig. 7.5 (b) and (c) on a logarithmic scale, respectively. The straight solid lines are plotted for visual guides. The dependence of the DLE intensity on the excitation intensity well follows a power law function,

$$I \propto I_{ex}^{\alpha} \tag{7.2}$$

where I is the luminescence intensity, I_{ex} is the laser intensity for excitation, and α is the exponent. The strength of the DLE shows a slightly sublinear dependence on the laser intensity with $\alpha \approx 0.9$.

The evolution of the integrated NBE can be divided into two parts (Fig. 7.5(c)). When the laser intensity is lower than 20 W/cm^2, the NBE increases approximately linearly with the laser intensity with a exponent of $\alpha_1 \approx 1.1$. When the laser intensity exceeds 20 W/cm^2, the dependence changes into a superlinear one and still roughly follows the power law form with an exponent of $\alpha_2 \approx 2.3$. Under even higher excitation intensities, the exponent tends to decrease. These results indicate that the DLE and NBE have significantly different dependencies on excitation intensity.

The relative strength of DLE in photoluminescence spectra is commonly used to characterize

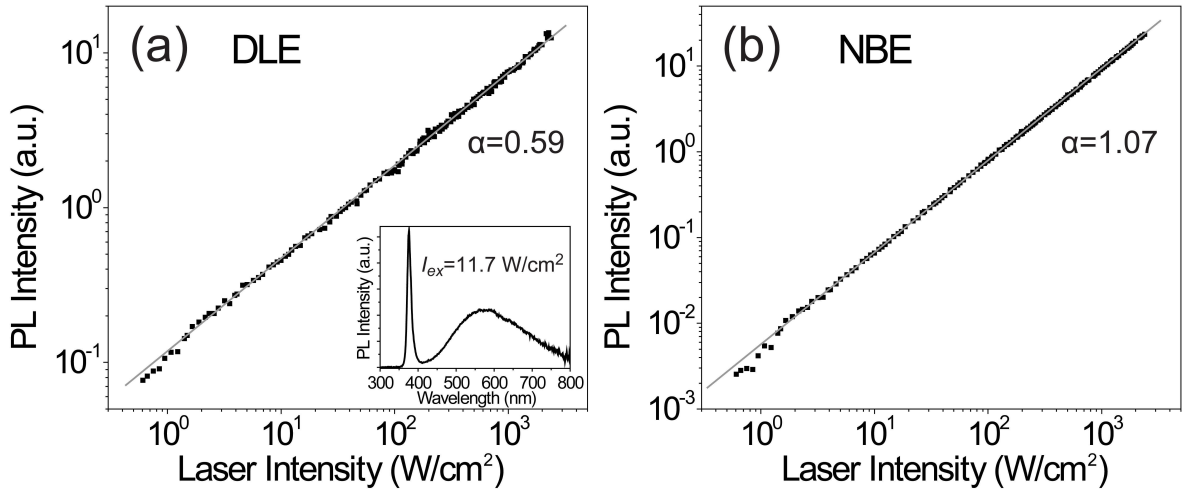

Figure 7.6: Integrated intensities of the DLE (a) and NBE (b) of an m-plane ZnO wafer as a function of excitation intensity at room temperature. The inset is a photoluminescence spectrum of the ZnO wafer recorded with a laser intensity of 11.7 W/cm^2.

the defect abundance and crystal quality of ZnO samples. The present results suggest that a safe conclusion may be arrived at only if the measurements are performed under the same excitation conditions.

7.3.2 Commercial hydrothermally grown ZnO wafers

The investigated ZnO wafers (m-plane and c-plane) are purchased from Crystec and are grown by a hydrothermal method. The wafers have a thickness of 0.5 mm. The surface is polished. The wafer surface is composed of a ZnO($10\bar{1}0$) plane or ZnO(0001) plane, commonly referred to as m-plane and c-plane, respectively. The optical measurements of the m-plane and c-plane wafers yield very similar results. The results shown below are measured on an m-plane wafer.

Figure 7.6 shows the integrated intensities of the DLE and NBE bands of an m-plane ZnO wafer versus the laser intensity at room temperature. A typical photoluminescence spectrum is shown in the inset, which is recorded with a laser intensity of 11.7 W/cm^2. Its DLE band peaks around 580 nm, compared to 510 nm in the ZnO nanowires investigated above, indicating that different deep centers are responsible for the DLE of the wafers.

The integrated DLE intensity obeys well the power law dependence on excitation intensity but with a smaller exponent (α = 0.59) than the one of the ZnO nanowires. In comparison, the NBE increases almost linearly with excitation intensity (Fig. 7.6(b)). When the laser intensity rises from 0.5 to 1000 W/cm^2, the NBE shows a increase of more than 4 orders of the integrated intensity compared to the 2-order increase observed in the DLE. The excitation intensity dependence of the luminescence of the ZnO wafer is significantly different from that observed in the ZnO nanowires, illustrating that the observed effect is not a general one for ZnO materials but sample-specific. It is sensitive to the preparation method and conditions, which may induce different kinds of defects or bring in different impurities during growth.

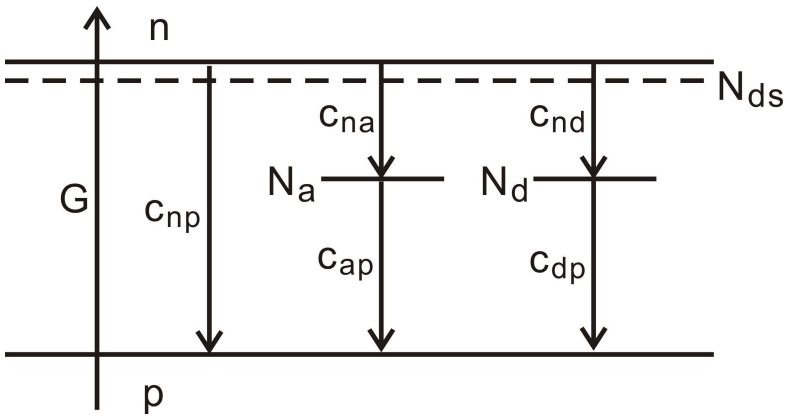

Figure 7.7: Schematic of excitation and recombination processes in ZnO. G is the electron-hole pair generation rate under photoexcitation. n and p are the electron and hole densities. N_a and N_d are the deep acceptor and donor concentrations and N_{ds} is the shallow donor concentration. c_{ij} is the corresponding bimolecular recombination coefficient.

7.4 Model

A model of the optical recombination dynamics in ZnO will be discussed in this section in order to explain the observed experimental results. It is adapted from previous studies on the photoluminescence properties of GaN [90, 196]. The model is established in the linear optics regime, which takes into account the band-to-band transitions, the deep-level radiative and non-radiative recombinations, and the commonly observed intrinsic n-type conductivity of ZnO materials. The interband transitions are treated as direct recombinations between conduction band electrons and valence band holes. The Coulomb interaction among these holes and electrons is ignored. The donor-acceptor pair (DAP) recombination is not taken into account. The deep-level-related recombination is classified into two types: donor-state and acceptor-state recombination. The operating rates for different recombination channels are represented with their bimolecular recombination coefficients. The excitation intensity dependence of these optical transitions is calculated using different electron-hole pair generation rates.

Figure 7.7 schematically illustrates the model of the photo-excitation and recombination processes in ZnO for theoretical simulation. G represents the electron-hole pair generation rate corresponding to the excitation intensity used for the photoluminescence measurements. The electrons and holes can recombine through direct inter-band transition or deep acceptor (N_a) or deep donor (N_d) assisted processes. c_{ij} denotes the bimolecular recombination coefficient for different recombination routes. N_{ds} denotes the concentration of shallow donors that are responsible for the intrinsic n-type conductivity of ZnO. In the present discussion, these shallow donors are assumed to be completely ionized. The experimentally observed DLE of ZnO and the non-radiative transitions are represented by those two deep center related recombinations.

At equilibrium, the charge generation-annihilation balances, resulting in the following equa-

tions,

$$\frac{dn}{dt} = G - c_{np}np - c_{na}nN_a^0 - c_{nd}nN_d^+ = 0 \tag{7.3}$$

$$\frac{dN_a^0}{dt} = c_{na}nN_a^0 - c_{ap}N_a^- p = 0 \tag{7.4}$$

$$\frac{dN_d^+}{dt} = c_{nd}nN_d^+ - c_{dp}N_d^0 p = 0 \tag{7.5}$$

where N_a^0 and N_a^- are the neutral and ionized deep-acceptor concentrations, and N_d^0 and N_d^+ are the neutral and ionized deep-donor concentrations. Their sums are equal to the total concentration of the corresponding deep centers, respectively,

$$N_a^0 + N_a^- = N_a \tag{7.6}$$

$$N_d^+ + N_d^0 = N_d \tag{7.7}$$

The charge conservation gives,

$$n + N_a^- = p + N_d^+ + N_{ds} \tag{7.8}$$

The photoluminescence intensities are related to the recombination rates as

$$I_{NBE} \propto c_{np}np \tag{7.9}$$

$$I_{DLE} \propto c_{na}nN_a^0 \quad or \quad c_{nd}nN_d^+ \tag{7.10}$$

The equation system 7.3–7.8 can be solved numerically. There are several constant parameters, including the concentrations of defects N_a, N_d, N_{ds} and the recombination coefficients c_{ij}, which are dependent on the specific growth method and conditions of the ZnO materials. These parameters are carefully adjusted during the simulation until good agreement with the experimental results is obtained.

Figure 7.8 shows the final fitting results of the excitation intensity dependence of the luminescence intensities as a function of electron-hole pair generation rate for ZnO nanowires (a) and wafer (b), respectively. The calculated results based on the above model are represented by solid lines. With regard to the photoluminescence experiments, some facts have to be kept in mind. Due to the refractive index dispersion of light in optical lenses, the NBE and DLE with different wavelengths cannot be accurately co-focused and equally coupled into the spectrometer. Thus, the absolute intensities of the NBE and DLE bands in the recorded spectra cannot exactly represent the real emission of the samples. Due to this consideration, the calculated and experimental results shown in Fig. 7.8 are normalized to the values at the crossing points, respectively. The laser power intensity used in experiments is converted into electron-hole generation rate assuming that every absorbed photon excites one electron-hole pair in ZnO. The effective thickness of the photo-excited layer beneath the surface is estimated to be 100 nm according to the absorption coefficient of $\sim 1.5 \times 10^5$ cm^{-1} of ZnO at 325 nm [197]. The parameters used for calculations are listed below, In order to obtain a good fitting to the experimental results of ZnO nanowires (Fig. 7.8(a)), relatively higher defect concentrations (N_d and N_{ds}) have to be used in comparison to those used for fitting to the results of the wafer. This is consistent with their lower crystal quality compared to the commercial ZnO wafers. The shallow donor concentrations (N_{ds}) used for both cases are consistent in order of the magnitude

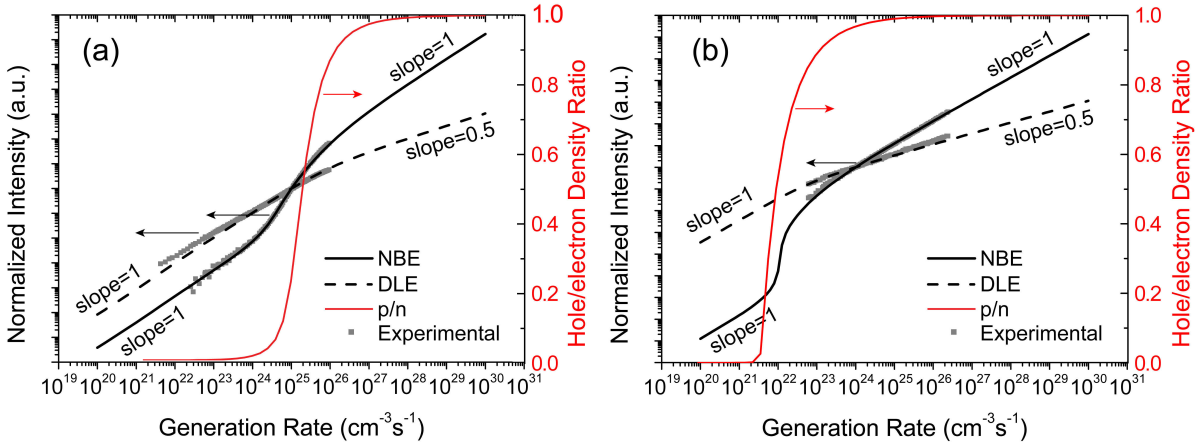

Figure 7.8: Comparison between calculated and measured luminescence intensities of ZnO nanowires (a) and ZnO wafers (b) as a function of electron-hole pair generation rate. The red lines in both figures are the simulated evolution of the ratio of the hole density to the electron density. The calculated and experimental results are normalized to the values at 10^{25} $cm^{-3}s^{-1}$ in (a) and 10^{24} $cm^{-3}s^{-1}$ in (b), respectively. The parameters used for calculation are listed in Table 7.1.

Table 7.1: Parameters used for the calculations of the excitation-intensity-dependent luminescence intensities of ZnO nanowires and wafer shown in Fig. 7.8.

Sample	N_a (cm^{-3})	N_d (cm^{-3})	N_{ds} (cm^{-3})	c_{np} (cm^3s^{-1})	c_{na} (cm^3s^{-1})	c_{ap} (cm^3s^{-1})	c_{nd} (cm^3s^{-1})	c_{dp} (cm^3s^{-1})
NW	10^{15}	3.5×10^{16}	10^{17}	10^{-11}	10^{-11}	10^{-7}	10^{-9}	10^{-8}
wafer	10^{15}	10^{15}	10^{16}	10^{-11}	10^{-9}	10^{-6}	10^{-12}	10^{-7}

with the commonly observed free electron density in ZnO [198–201]. The same bimolecular coefficient $c_{np} = 10^{-11}$ cm^3s^{-1} for band-edge recombination processes is used. The recombination coefficients for deep level transitions used for the simulations are different for the nanowire and wafer samples, which is reasonable due to the different luminescence origins of their DLE bands.

In addition, the experimental results of the DLE of the ZnO nanowires can only be well fitted by the deep donor related recombination in the model with bimolecular recombination coefficients $c_{nd} > c_{na}$, as shown in Table 7.1. For ZnO wafers, the situation is inverse. The DLE is fitted with the deep acceptor related recombination with $c_{nd} < c_{na}$. This difference illustrates again the different origins for the DLE of the nanowire and the wafer samples.

The calculated dependencies show good agreement with the experimental results. In the calculated curves, turning points can be seen for both kinds of samples where the increasing rates of the NBE and DLE with the generation rate significantly change. For the nanowires, at around 10^{25} $cm^{-3}s^{-1}$, the DLE transits from a linear to a square-root dependence on excitation intensity while the NBE curve increases superlinearly and then returns to a linear increase. The dependence of the DLE is similar to the simulated results in the GaN model in the literatures which mainly studied the defect luminescence of GaN [90, 196]. However, the dependence of the NBE (with transition from a linear dependence on the excitation intensity to a superlinear one)

and the successful fitting with the recombination model, to the best of the author's knowledge, has not been reported yet. The trends for the ZnO wafer are similar. But the turning point shifts to a lower generation rate (between 10^{22} and 10^{23} $cm^{-3}s^{-1}$). The excitation-intensity-dependent photoluminescence is further discussed in the following for low and high excitation intensities, respectively.

Simple algebraic transformation of Equ. 7.3−7.8 gives the recombination rates of the deep-level transitions as

$$R_{DLEa} = c_{na} n N_a^0 = \frac{c_{na} c_{ap} N_a np}{c_{na} n + c_{ap} p} \tag{7.11}$$

$$R_{DLEd} = c_{nd} n N_d^+ = \frac{c_{nd} c_{dp} N_d np}{c_{nd} n + c_{dp} p} \tag{7.12}$$

with

$$N_a^0 = \frac{c_{ap} p}{c_{na} n + c_{ap} p} N_a \tag{7.13}$$

$$N_d^+ = \frac{c_{dp} p}{c_{nd} n + c_{dp} p} N_d \tag{7.14}$$

Substituting the above expressions into Equ. 7.3 yields

$$G = c_{np} np + \frac{c_{na} c_{ap} N_a}{c_{na} n + c_{ap} p} np + \frac{c_{nd} c_{dp} N_d}{c_{nd} n + c_{dp} p} np \tag{7.15}$$

This equation describes the balancing between the generation rate G and the recombination processes through those three channels. The first term on the right side represents the rate of the inter-band recombination. It linearly depends on the product of the electron and hole densities np. The last two deep-level recombination terms depend on np but with variable coefficients. Increasing electron and hole densities will decrease the strength of deep-level recombinations relative to the direct inter-band recombination.

The simulated evolution of the concentration ratio of the holes to electrons p/n with increasing generation rate G is plotted in Fig. 7.8. Taking the nanowire sample for instance, under low excitation intensities ($< 10^{24}$ $cm^{-3}s^{-1}$), the photogenerated electron and hole densities are negligible compared to that of the intrinsic conduction electrons due to the ionization of the shallow donors. Thus, the total electron density n is much higher than the hole density p. The concentration ratio p/n is almost zero. According to Equ. 7.13 and 7.14, it has $N_a^0 \approx 0$ and $N_d^+ \approx 0$, indicating that the acceptor centers are almost completely ionized while the deep donor centers keep neutral. The Equ. 7.15 can be simplified to be

$$G \approx c_{np} np + c_{ap} N_a p + c_{dp} N_d p \tag{7.16}$$

Because of the large base number of n, it can be regarded as constant while p increases linearly with the generation rate G. Therefore, all the three terms in Equ. 7.16 for band-edge and deep-level recombination increase near-linearly with p and hence the generation rate G.

As the excitation intensity increases, more electron-hole pairs are generated. p increases and cannot be ignored anymore compared to the electron density n. When the generation rate for

the nanowires exceeds 10^{27} cm$^{-3}s^{-1}$ (Fig. 7.8(a)), the carrier densities n and p are much larger than the densities of the defects, and it has $p/n \approx 1$. The Equ. 7.13 and 7.14 convert to

$$N_a^0 = \frac{c_{ap}}{c_{na} + c_{ap}} N_a \tag{7.17}$$

$$N_d^+ = \frac{c_{dp}}{c_{nd} + c_{dp}} N_d \tag{7.18}$$

Both the acceptor centers and the deep donor centers become partly ionized and the percentages of the ionized centers are determined by the involved bimolecular recombination coefficients. These percentages stay constant for higher generation rates. Due to the high density of the charge carriers relative to that of the defects, the last two terms in Equ. 7.15 become negligible, leading to a linear dependence of the NBE on the generation rate with both n and p proportional to $G^{1/2}$, respectively. The last two terms are reduced to be proportional to $G^{1/2}$, resulting in a square-root dependence of the DLE on excitation intensity, as shown in Fig. 7.8.

For the generation rate in the range of $10^{24} < G < 10^{27}$ cm$^{-3}s^{-1}$ (Fig. 7.8(a)), the hole density becomes gradually comparable to the electron density. The deep-level recombination processes gradually saturate and change to be sublinearly dependent on excitation intensity. Thus, more charge carriers will recombine through direct band-edge transition processes, resulting in the superlinear increase of the band-edge emission. Those three recombination channels interact mutually, defining the sample-specific excitation intensity dependence of the photoluminescence.

Simulation further reveals that the threshold generation rate for the transition of the luminescence dependencies on the excitation intensity (where p approximates to n) is sensitive to the concentrations of the acceptor and donor centers as well as the recombination coefficients, which is also implied in Equ. 7.8. In general, smaller defect densities correspond to lower excitation thresholds for $p \approx n$ and the deep-level recombination saturation, as presented in Fig. 7.8(b) for the ZnO wafer samples. According to the simulated results, when using further lower excitation intensities for measurements, the saturation of the defect emission and the superlinear increase of the band-edge emission intensity with the excitation intensity should also be observed in the wafers.

7.5 Excitation-intensity-dependent photoluminescence of ZnO nanowires at low temperature

The excitation-intensity-dependent photoluminescence of ZnO is further studied at low temperature. The sample investigated in this section is a ZnO nanowire sample grown by thermal CVD method at relatively lower temperature than that investigated above. The growth is based on a direct vapor-solid (VS) process without the catalysis effect of Au, which is described in section 4.1.2. The average diameter of the nanowires is 95 nm and their average length is around 4.9 μm. The nanowire samples are mounted in a cryostat that can be cooled to 70 K using liquid nitrogen. The 325 nm HeCd laser is used as excitation source.

Figure 7.9 shows the integrated DLE and NBE intensities versus the laser intensity. The results in (a) and (b) are measured at room temperature, and (c) and (d) are measured at liquid nitrogen temperature (70 K). The DLE at both room temperature and low temperature follows

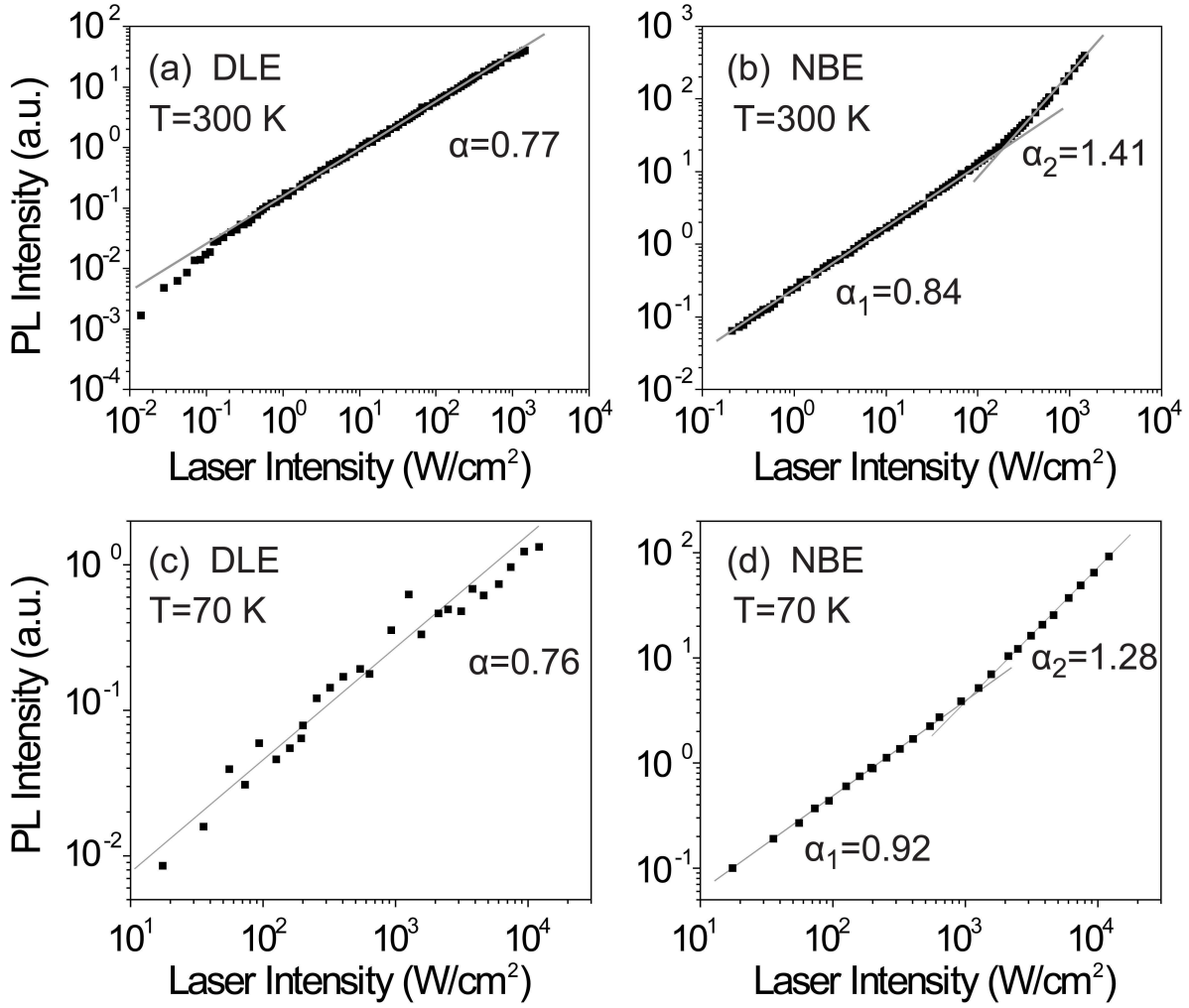

Figure 7.9: Integrated intensities of the DLE (a and c) and NBE (b and d) of VS-grown ZnO nanowires at room temperature (top) and liquid nitrogen temperature (bottom) as a function of the excitation intensity.

a power law dependence with similar exponent ($\alpha \approx 0.77$). At room temperature, the NBE first increases sublinearly with the laser intensity. Then the increase changes to be superlinear over 2×10^2 W/cm^2. The results at 70 K are similar but with sightly different exponents. In addition, the turning point in the dependence increases to $\sim 10^3$ W/cm^2 at low temperature.

The sublinear increase of the NBE at low excitation intensities cannot be explained by the recombination model discussed above. This difficulty could be raised due to the presence of extra recombination mechanisms in the nanowires that are not included in the model, such as the non-radiative Auger recombination process, which has a cubic dependence on the charge density.

The evolutions of the photoluminescence spectra and the high resolution NBE with increasing excitation intensity are shown in Fig. 7.10 (a) and (b), respectively. The NBE enhances significantly relative to the DLE with increasing excitation intensity. In addition, the DLE shows similar features as observed on the VLS-grown nanowires. Its band maximum is also comparable to the latter. This suggests that these two nanowire samples have the same kind of

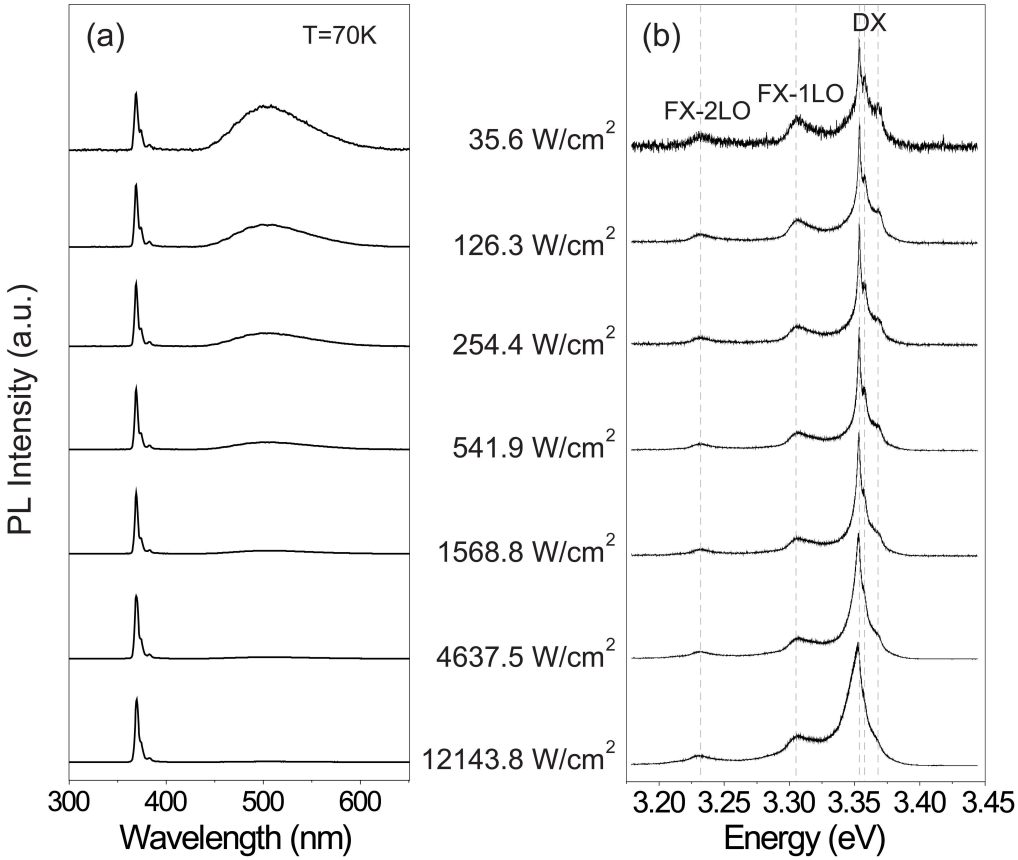

Figure 7.10: Evolution of the overall photoluminescence spectrum (a) and the high resolution NBE (b) of VS-grown ZnO nanowires at 70 K.

defects responsible for their DLE bands.

In the right figure, the high resolution NBE spectra are dominated by neutral donor bound exciton (DX) lines. The two peaks at the low energy part are assigned to longitudinal optical phonon replicas of the free excitons (FX-nLO). When the excitation intensity is increased, a broadening of the DX band can be seen while its maximum stays at the same energy position. The phonon replica bands have no obvious change.

Figure 7.11(a) shows the magnification of the donor-bound exciton emission bands under different excitation intensities. The spectra are normalized to the luminescence maxima. A significant broadening of the band on its low energy side with increasing excitation intensity can be seen. The variation of the half width at half maximum (HWHM) of the emission band is plotted in Fig. 7.11(b) versus laser intensity. When the laser intensity is below 10^3 W/cm^2, the HWHM stays at around 2 meV. Above 10^3 W/cm^2, the HWHM increases rapidly to 10 meV. It is interesting to notice that the onset of the DX band broadening coincides well with the conversion of the NBE from a sublinear dependence on excitation intensity to a superlinear one as shown in Fig. 7.9(d).

According to previous studies [94, 202], a laser intensity in the order of 10^3 W/cm^2 can generate sufficiently high exciton densities to form biexciton states due to exciton-exciton collision. These biexciton states will give rise to a new emission band, called the M band. Its lumines-

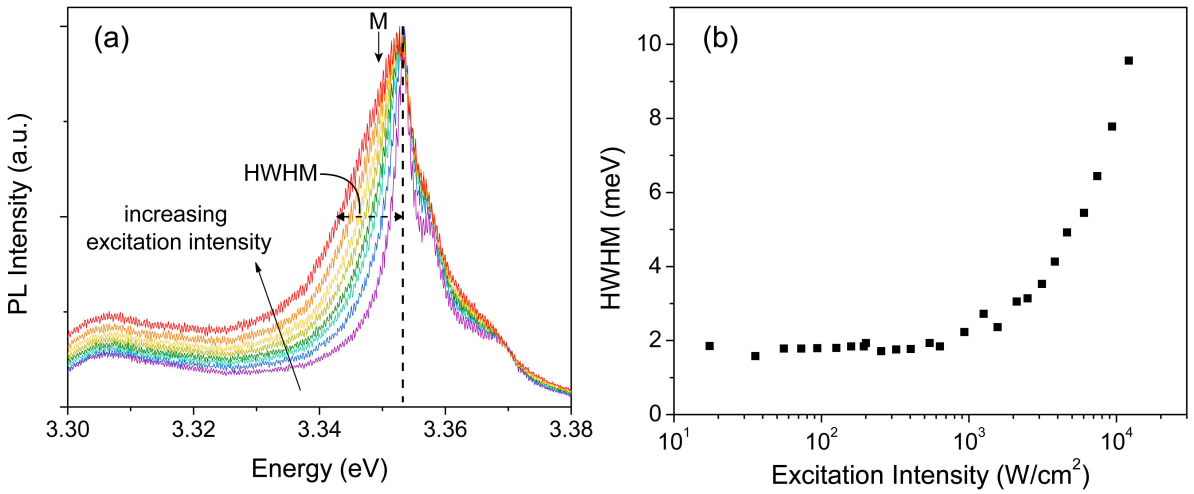

Figure 7.11: (a) High resolution exciton emission line of VS-grown ZnO nanowires under different excitation intensities. The spectra are normalized to the luminescence maxima. (b) Half width at half maximum (HWHM) of the donor bound exciton emission line (low energy side) as a function of the excitation intensity.

cence intensity is superlinearly dependent on the excitation intensity [26],

$$I_{bi} \propto G^i \qquad 1 < i \leq 2 \tag{7.19}$$

The binding energy of biexcitons has been reported to be 17.5 meV in ZnO nanorods grown by metalorganic chemical vapour deposition (MOCVD) [202], which is among the binding energies of donor bound excitons (typically in the range of 10–20 meV [19, 38]). The binding energy is higher than the thermal energy at $T = 70$ K (6 meV). Thus biexcitons can stably exist in ZnO nanowires. The M band has been observed at a slightly lower energy position (~ 2 meV lower, as marked in Fig. 7.11(a)) than the prominent donor bound exciton emission in previous studies on epitaxially grown ZnO nanorods [202] and ZnO thin films prepared by metal organic vapour phase epitaxy [94]. Therefore, the DX band broadening and the superlinear increase of the NBE at high excitation intensity in the ZnO nanowires could be partly induced by the excitation of biexciton complexes.

Another possibility might be the formation of an electron-hole plasma phase in the nanowires, corresponding to the high density regime of excitation. In this regime, the density of excitons is so high that their average distance is comparable to or smaller than the Bohr radius. As a result, the electron-hole bound states cannot be deemed as individual quasiparticles any longer and a new collective phase of the charge carriers is formed, which is know as the electron-hole plasma (EHP). The present observations are very similar to that reported in previous works about VLS-grown ZnO nanowires, in which the authors attributed the asymmetric broadening of the donor-bound exciton luminescence peak to the transition to an EHP occurring at ~ 21 kW/cm^2 [203]. This threshold could be lowered in the present case due to the relatively low growth temperature (substrate temperature: 750 °C) of the nanowires which can induce high defect concentration and hence high electron density.

7.6 Summary

In this chapter, the excitation intensity dependence of the photoluminescence properties of ZnO is studies. The investigated samples include ZnO nanowires grown by chemical vapor deposition (CVD) based on a Au-catalyzed vapor-liquid-solid (VLS) process and a catalyst-free vapor-solid (VS) process, respectively, and hydrothermally grown ZnO wafers. The photoluminescence spectra of the ZnO samples generally consist of two main bands, namely a near-band-edge emission (NBE) band and a deep-level related emission (DLE) band. At low temperature, the NBE band of the ZnO nanowire samples is dominated by the emission of donor-bound excitons. Temperature-series measurements demonstrate that the NBE band at room temperature mainly consists of the emission of free excitons and their longitudinal optical (LO) phonon replicas.

The DLE spectrum at low temperature peaks around 2.45 eV and exhibits multiple peaks with equal energy spacing, which are attributed to LO phonon replicas of specific deep-level transitions. The assignment of the involved defects cannot be achieved with the present results. Oxygen vacancies and copper impurities are two most suggested origins of this green emission band in the literature. Considering the low likelihood of introducing copper atoms during the nanowire growth and the spectral shift of the band at low temperature, the present results provide more support to the assignment of this defect emission to oxygen vacancy related transitions.

The photoluminescence properties of the ZnO nanowire and wafer samples are studies under a wide range of laser excitation intensities (10^{-1}–10^{3} W/cm^2). At room temperature, the DLE of all samples increases sublinearly with excitation intensity. The NBE of the ZnO wafers increases near-linearly with the excitation intensity. However, the ZnO nanowires exhibit a significantly different dependence. The NBE of the VLS-grown ZnO nanowires increases near-linearly under low excitation intensities and changes into superlinear increase under high excitation intensities. The increase of the VS-grown nanowire sample (prepared at relatively lower temperatures) follows a similar pattern while its NBE shows a sublinear increase under low excitation intensities.

A model for the optical recombination processes in ZnO is adapted from the literature. The model includes three basic recombination channels: the inter-band recombination and the recombinations through deep donor and acceptor centers. The recombination rates are represented by the bimolecular recombination coefficients. The recombination dynamics of this model is calculated numerically. The parameters including the defect concentrations and recombination coefficients are adjusted carefully around the literature values until good agreement with the experimental results is obtained. The simulation can explain the sublinear increase of the DLE with excitation intensity and the superlinear increase of the NBE under high excitation intensities. However, it fails to predict a sublinear increase of the NBE observed on the VS-grown ZnO nanowires, indicating the limitation of the present model.

The photoluminescence of the VS-grown ZnO nanowires is further investigated at liquid nitrogen temperature (T = 70 K). Its dependence on excitation intensity is similar to that observed at room temperature. High resolution measurements of the NBE reveal that the dominating donor bound exciton emission line shows significant broadening above a threshold laser intensity (around 10^{3} W/cm^2). Above this laser intensity, the NBE further shows a superlinear increase with excitation intensity. These observations are probably due to the formation of

biexcitons or an electron-hole plasma in the nanowires under high excitation intensities, which gives rise to new emission bands and results in the asymmetric broading of the donor bound exciton emission line.

The present work improves the understanding of the optical properties and the recombination processes in ZnO. In addition, photoluminescence spectroscopy is usually used to characterize the defect concentrations or crystal qualities of ZnO materials. The present results further suggest that identical excitation conditions should be ensured during this process to arrive at reliable conclusions.

Chapter 8

Summary and Outlook

In this work, colloidal CdSe quantum dots (QDs) are synthesized. Their growth kinetics and optical properties are studied. A hybrid structure is fabricated by surface functionalization of ZnO nanowires (NWs) with CdSe QDs. The charge transfer in the hybrid structure is studied via photoconductivity measurements. In addition, the excitation intensity dependence of the photoluminescence properties of ZnO nanowires and bulk wafers is investigated.

Colloidal CdSe QDs are synthesized using a wet chemical method. They are capped with bifunctional thiol-carboxyl molecules as stabilizers making them soluble in water. Transmission electron microscopy measurements demonstrate the spherical shape of the QDs and their crystallinity. The prepared QDs have sizes varying in the range of 1.4–2.5 nm and molar concentration of 30–100 μM in the crude solution after synthesis time up to 120 hours. Their absorption onset is accordingly tunable in the range of 400–550 nm. The growth kinetics of the QDs are analyzed.

The growth starts with an Ostwald ripening process, in which smaller particles in the solution gradually shrink while the bigger ones continue to grow, resulting in a broadening of the particle size distribution. Afterwards, the growth enters into a balance stage where the growth rate slows down and the size distribution stays constant. The photoluminescence quantum yield of the QDs reaches its maximum of 11 % in this stage. Further heating initiates a size-focusing stage, in which the size distribution of the QDs is gradually narrowed. This process lasts until the end of the synthesis.

The photoluminescence (PL) of the prepared CdSe QDs in dry powder form is studied in different gas environments. The luminescence intensity is found to dramatically decrease in vacuum and highly pure nitrogen, which is attributed to oxygen-controlled surface effects. Oxygen molecules adsorbed on the QD surface can effectively passivate the surface defects of the QDs which otherwise act as trap centers during the photoexcitation process and enable non-radiative Auger recombination processes.

The chemical stability of the CdSe QDs is examined. The combined effect of light illumination and oxygen is found to induce a gradual photo-oxidation process of the thiol ligands and detach them from the QD surface, resulting in the degradation of the QD stability. These effects should be considered during the QD storage and applications.

A ZnO-nanowire/CdSe-quantum-dot (ZnO-NW/CdSe-QD) hybrid structure is fabricated by attaching the prepared CdSe QDs onto the ZnO nanowire surface with the ligands of the QDs

acting as molecular linkers. The photoconductivity (PC) of the hybrid structure is investigated in different gas environments. An argon ion laser operating at 458 nm is chosen as excitation source to selectively excite the CdSe QDs. By measuring the photoresponse of the conductivity of the nanowires, a detailed investigation of the charge transfer processes in the hybrid structure is possible.

Under laser irradiation, the photoconductivity of the hybrid sample increases dramatically (up to $\sim$ 10 times in air), and restores to the initial value after termination of the irradiation. However, the photoconductivity exhibits essentially different rise and decay kinetics in oxygen-rich (air and dry oxygen) and oxygen-free (vacuum, nitrogen and argon) environments. A model is proposed to explain the results. Desorption of surface oxygen from both the ZnO nanowires and the CdSe quantum dots, activated by electron tunnelling between the nanowires and the quantum dots, is found to be the dominating process that determines the dynamics of the photoconductivity in the hybrid nanowire/quantum-dot structures.

Another important part of this work is devoted to the study of the excitation intensity dependence of the photoluminescence properties of ZnO under a wide range of laser intensity (10^{-1}–10^{3} W/cm^2). The investigated samples include ZnO nanowires grown by chemical vapor deposition (CVD) based on a Au-catalyzed vapor-liquid-solid (VLS) process and a catalyst-free vapor-solid (VS) process, respectively, and commercial ZnO bulk wafers grown by a hydrothermal method. The photoluminescence spectra consist of two main bands: a near-band-edge emission (NBE) band and a deep-level emission (DLE) band. The former is mainly arising from recombinations of free excitons, excitons bound to donors and acceptors as well as their phonon replicas. The latter is related to recombinations through deep levels in the band gap induced by structural defects or chemical impurities. The relative strength between the NBE band and the DLE band is found to vary significantly with the excitation intensity. The luminescence intensities of these two emission bands dependent on the laser intensity are investigated, which exhibits sample-specific results.

A theoretical model is adapted in the linear optics regime to simulate the photoexcitation and recombination processes in ZnO. It includes three recombination channels: the inter-band recombination and the recombinations through deep donor and acceptor centers. The recombination rates are represented by the bimolecular recombination coefficients. The recombination dynamics are calculated numerically with parameters adjusted around literature values until good agreements with experimental results are obtained. The calculated results are well fitted to the results of the ZnO wafers and VLS-grown nanowires. However, the model fails to predict a sublinear increase of the NBE emission with excitation observed on the VS-grown nanowire sample, probably due to the extra recombination mechanisms not included in the model such as Auger recombination.

The excitation-dependent photoluminescence is further investigated at liquid nitrogen temperature (T = 70 K), which shows similar behaviors to that observed at room temperature. High resolution spectroscopy measurements of the NBE emission reveal that the dominating donor bound exciton emission peak undergoes significant spectral broadening for laser intensities above a threshold (around 10^{3} W/cm^2), at which the NBE intensity of the sample becomes superlinearly dependent on the excitation intensity. This is probably due to the formation of biexcitons through exciton-exciton collision or even an electron-hole plasma (EHP) under high excitation intensity. The experimental results further suggest that using photoluminescence spectroscopy for characterization of defect abundance or crystal quality of ZnO

samples, one may arrive at a safe conclusion only if the same excitation conditions are used for the measurements.

Outlook

Some fundamental properties of semiconductor QDs like the photoluminescence blinking of single QDs is still not completely understood. Further measurements probably with high spatial and temporal resolutions are required to find out the mechanism of the random switching between the emission ON state of the QDs to their OFF state. Based on these understandings, the probability of the emission OFF state could be effectively reduced so that the overall luminescence intensity of large QD ensemble can be improved. This is of great interest for applications that require a high luminescence efficiency of QDs.

The charge transfer dynamics in the QD-sensitized ZnO nanowire hybrid structures needs further studies. The influence of the ligands of the QDs and their length on the charge transfer rates between the QDs and the nanowires has to be examined carefully, in order to obtain more efficient charge injection and separation effects. This is essential for applications using QDs as photosensitizers, such as photovoltaic devices and photodetectors. To obtain this goal, the nanowire/quantum-dot hybrid structures assembled using QDs with different molecular ligands could be analysed by time resolved photoluminescence and absorption measurements.

Questions are still present in the photoluminescence properties of ZnO materials. The assignments of their deep-level emissions still have wide controversy. The defects responsible for different deep-level emission bands are probably dependent on growth techniques and conditions of the materials. Careful measurements and comprehensive analysis with different characterization techniques, e.g. temperature- and excitation-dependent photoluminescence measurements, need to be done to give more insight into these issues. Furthermore, enhancing the band-edge emission of ZnO while simultaneously suppressing the defect emission is also a long-living research topic. In addition to the improvement of the growth techniques, the post-preparation treatments are also effective approaches. One possibility for ZnO nanomaterials is through surface coating with semiconductor QDs which have resonant absorption of the defect emission of ZnO and can inject the excited electrons back into the ZnO materials. Coatings with differently sized QDs can be examined to find out the optimum configuration.

In addition, due to the large surface-to-volume ratio, the surface plays a very important role in semiconductor nanomaterials and has significant influence on their physical properties. This further induces a high sensitivity of their properties to the ambient environment. Proper packaging techniques need to be developed for nanostructured devices which can reduce undesired impacts from the ambient and in the meantime maintain the intrinsic properties and functionality of the nanomaterials.

Bibliography

[1] R. Yan, D. Gargas, P. Yang, *Nature Photonics* **3**, 569 (2009)

[2] S. Rühle, M. Shalom, A. Zaban, *Chemphyschem* **11**, 2290 (2010)

[3] J. Li, J. Z. Zhang, *Coordination Chemistry Reviews* **253**, 3015 (2009)

[4] S. Liu, Z. Tang, *Journal of Materials Chemistry* **20**, 24 (2010)

[5] M. Grätzel, *Nature* **414**, 338 (2001)

[6] T. Voss, G. Svacha, E. Mazur, S. Müller, C. Ronning, D. Konjhodzic, F. Marlow, *Nano Letters* **7**, 3675 (2007)

[7] Y. Heo, D. Norton, L. Tien, Y. Kwon, B. Kang, F. Ren, S. Pearton, J. LaRoche, *Materials Science and Engineering: R: Reports* **47**, 1 (2004)

[8] Z. L. Wang, *Journal of Physics: Condensed Matter* **16**, R829 (2004)

[9] Q. H. Li, Y. X. Liang, Q. Wan, T. H. Wang, *Applied Physics Letters* **85**, 6389 (2004)

[10] M. H. Huang, S. Mao, H. Feick, H. Yan, Y. Wu, H. Kind, E. Weber, R. Russo, P. Yang, *Science* **292**, 1897 (2001)

[11] Z. Fan, D. Wang, P.-C. Chang, W.-Y. Tseng, J. G. Lu, *Applied Physics Letters* **85**, 5923 (2004)

[12] X. D. Bai, P. X. Gao, Z. L. Wang, E. G. Wang, *Applied Physics Letters* **82**, 4806 (2003)

[13] Z. Li, G. Zhu, R. Yang, A. C. Wang, Z. L. Wang, *Advanced materials* **22**, 2534 (2010)

[14] D. Look, D. Reynolds, J. Sizelove, R. Jones, C. Litton, G. Cantwell, W. Harsch, *Solid State Communications* **105**, 399 (1998)

[15] K. S. Leschkies, R. Divakar, J. Basu, E. Enache-Pommer, J. E. Boercker, C. B. Carter, U. R. Kortshagen, D. J. Norris, E. S. Aydil, *Nano Letters* **7**, 1793 (2007)

[16] T. Ando, A. B. Fowler, F. Stern, *Reviews of Modern Physics* **54**, 437 (1982)

[17] P. M. Petroff, A. Lorke, A. Imamoglu, *Physics Today* **54**, 46 (2001)

[18] T.-H. Kim, K.-S. Cho, E. K. Lee, S. J. Lee, J. Chae, J. W. Kim, D. H. Kim, J.-Y. Kwon, G. Amaratunga, S. Y. Lee, B. L. Choi, Y. Kuk, J. M. Kim, K. Kim, *Nature Photonics* **5**, 176 (2011)

[19] U. Özgür, Y. I. Alivov, C. Liu, A. Teke, M. A. Reshchikov, S. DogÌĘan, V. Avrutin, S.-J. Cho, H. MorkocÌğ, *Journal of Applied Physics* **98**, 41301 (2005)

[20] M. Seol, H. Kim, Y. Tak, K. Yong, *Chemical communications* **46**, 5521 (2010)

[21] K.-T. Kuo, D.-M. Liu, S.-Y. Chen, C.-C. Lin, *Journal of Materials Chemistry* **19**, 6780 (2009)

[22] J. Briscoe, D. E. Gallardo, S. Hatch, V. Lesnyak, N. Gaponik, S. Dunn, *Journal of Materials Chemistry* **21**, 2517 (2011)

[23] J. E. Jaffe, A. C. Hess, *Physical Review B* **48**, 7903 (1993)

[24] A. B. M. A. Ashrafi, A. Ueta, A. Avramescu, H. Kumano, I. Suemune, Y.-W. Ok, T.-Y. Seong, *Applied Physics Letters* **76**, 550 (2000)

[25] S. Desgreniers, *Physical Review B* **58**, 14102 (1998)

[26] C. F. Klingshirn, B. K. Meyer, A. Waag, A. Hoffmann, J. Geurts, *Zinc Oxide: From Fundamental Properties Towards Novel Applications*, Springer, Berlin (2010)

[27] C. Klingshirn, *ChemPhysChem* **8**, 782 (2007)

[28] D. G. Thomas, *J. Phys. Chem. Solids* **15**, 86 (1960)

[29] J. Hopfdeld, *Journal of Physics and Chemistry of Solids* **15**, 97 (1960)

[30] Y. Park, C. Litton, T. Collins, D. Reynolds, *Physical Review* **143**, 512 (1966)

[31] W. Liang, A. Yoffe, *Physical Review Letters* **20**, 59 (1968)

[32] B. Gil, *Physical Review B* **64** (2001)

[33] D. Reynolds, D. Look, B. Jogai, C. Litton, G. Cantwell, W. Harsch, *Physical Review B* **60**, 2340 (1999)

[34] R. Elliott, *Physical Review* **108**, 1384 (1957)

[35] C. Klingshirn, *Semiconductor Optics*, Springer (2006)

[36] K. Hümmer, *Physica Status Solidi (b)* **56**, 249 (1973)

[37] G. Wannier, *Physical Review* **52**, 191 (1937)

[38] B. K. Meyer, H. Alves, D. M. Hofmann, W. Kriegseis, D. Forster, F. Bertram, J. Christen, A. Hoffmann, M. Straß burg, M. Dworzak, U. Haboeck, A. V. Rodina, *Physica Status Solidi (b)* **241**, 231 (2004)

[39] A. Teke, U. Özgür, S. Dogan, X. Gu, H. Morko, B. Nemeth, J. Nause, H. O. Everitt, *Physical Review B* **70**, 195207 (2004)

[40] J. M. Hvam, G. Blattner, M. Reuscher, C. Klingshirn, *Physica Status Solidi (b)* **118**, 179 (1983)

[41] D. Magde, H. Mahr, *Physical Review Letters* **24**, 890 (1970)

[42] A. P. Alivisatos, *Science* **271**, 933 (1996)

[43] A. P. Alivisatos, *The Journal of Physical Chemistry* **100**, 13226 (1996)

[44] C. Murray, D. Norris, M. Bawendi, *Journal of the American Chemical Society* **115**, 8706 (1993)

[45] K. K. Nanda, F. E. Kruis, H. Fissan, *Nano Letters* **1**, 605 (2001)

[46] G. Pellegrini, G. Mattei, P. Mazzoldi, *Journal of Applied Physics* **97**, 073706 (2005)

[47] L. Brus, *The Journal of chemical physics* **80**, 4403 (1984)

[48] X. Peng, J. Thessing, *Controlled synthesis of high quality semiconductor nanocrystals*, Springer (2005)

[49] N. F. Borrelli, D. W. Hall, H. J. Holland, D. W. Smith, *Journal of Applied Physics* **61**, 5399 (1987)

[50] X. Chen, J. L. Hutchison, P. J. Dobson, G. Wakefield, *Journal of Materials Science* **44**, 285 (2008)

[51] M. G. Bawendi, a. R. Kortan, M. L. Steigerwald, L. E. Brus, *The Journal of Chemical Physics* **91**, 7282 (1989)

[52] U. Woggon, *Optical Properties of Semiconductor Quantum Dots*, Springer, Berlin (1997)

[53] A. I. Ekimov, F. Hache, M. C. Schanne-Klein, D. Ricard, C. Flytzanis, I. A. Kudryavtsev, T. V. Yazeva, A. V. Rodina, A. L. Efros, *Journal of the Optical Society of America B* **10**, 100 (1993)

[54] D. Norris, A. Sacra, C. Murray, M. Bawendi, *Physical Review Letters* **72**, 2612 (1994)

[55] H. H. von Grünberg, *Physical Review B* **55**, 2293 (1997)

[56] M. Bawendi, W. Wilson, L. Rothberg, P. Carroll, T. Jedju, M. Steigerwald, L. Brus, *Physical Review Letters* **65**, 1623 (1990)

[57] A. Efros, M. Rosen, M. Kuno, M. Nirmal, D. Norris, M. Bawendi, *Physical review. B* **54**, 4843 (1996)

[58] D. Norris, A. Efros, M. Rosen, M. Bawendi, *Physical review. B, Condensed matter* **53**, 16347 (1996)

[59] A. Pandey, P. Guyot-Sionnest, *Science* **322**, 929 (2008)

[60] S. V. Kilina, D. S. Kilin, O. V. Prezhdo, *ACS nano* **3**, 93 (2009)

[61] U. Bockelmann, *Physical Review B* **42**, 8947 (1990)

[62] H. Benisty, C. Sotomayor-Torrès, C. Weisbuch, *Physical Review B* **44**, 10945 (1991)

[63] Y. Yin, a. P. Alivisatos, *Nature* **437**, 664 (2005)

[64] G. Cao, *Nanostructures and nanomaterials: synthesis, properties, and applications*, World Scientific, Singapore (2004)

[65] V. K. LaMer, R. H. Dinegar, *J. Am. Chem. Soc.* **72**, 4847 (1950)

[66] X. Peng, D. M. P. Mingos (Editors), *Semiconductor Nanocrystals and Silicate Nanoparticles*, Springer-Verlag (2005)

[67] T. Sugimoto, *Advances in Colloid and Interface Science* **28**, 65 (1987)

[68] X. Peng, J. Wickham, A. P. Alivisatos, *Journal of the American Chemical Society* **120**, 5343 (1998)

[69] A. Rogach, *Semiconductor nanocrystal quantum dots: synthesis, assembly, spectroscopy and applications*, Springer (2008)

[70] C. B. Murray, C. R. Kagan, M. G. Bawendi, *Annual Review of Materials Science* **30**, 545 (2000)

[71] W. Yu, X. Peng, *Angewandte Chemie International Edition* **41**, 2368 (2002)

[72] L. Qu, Z. A. Peng, X. Peng, *Nano Letters* **1**, 333 (2001)

[73] Z. a. Peng, X. Peng, *Journal of the American Chemical Society* **123**, 183 (2001)

[74] S. B. Brichkin, E. V. Chernykh, *High Energy Chemistry* **45**, 1 (2011)

[75] A. L. Rogach, L. Katsikas, A. Kornowski, D. Su, A. Eychmüller, H. Weller, *Berichte der Bunsengesellschaft für physikalische Chemie* **100**, 1772 (1996)

[76] A. L. Rogach, A. Kornowski, M. Gao, A. Eychmüller, H. Weller, *The Journal of Physical Chemistry B* **103**, 3065 (1999)

[77] C. W. Bunn, *Proceedings of the Physical Society* **47**, 835 (1935)

[78] T. Damen, S. Porto, B. Tell, *Physical Review* **142**, 570 (1966)

[79] G. Galli, *Applied Physics Letters* **16**, 439 (1970)

[80] C. Mead, *Physics Letters* **18**, 218 (1965)

[81] I. T. Drapak, *Soviet Physics: Semiconductors* **2**, 624 (1968)

[82] T. Minami, M. Tanigawa, M. Yamanishi, T. Kawamura, *Japanese Journal of Applied Physics* **13**, 1475 (1974)

[83] A. Tsurkan, N. Fedotova, L. Kicherman, P. PasÂŠko, *Soviet Physics: Semiconductors* **6**, 1183 (1975)

[84] L. J. Brillson, *Journal of Vacuum Science and Technology* **15**, 1378 (1978)

[85] E. Tomzig, R. Helbig, *Journal of Luminescence* **14**, 403 (1976)

[86] D. Reynolds, C. Litton, T. Collins, *Physical Review* **140**, A1726 (1965)

[87] P. Loose, M. Rosenzweig, M. Wöhlecke, *physica status solidi (b)* **75**, 137 (1976)

[88] J. Gutowski, N. Presser, I. Broser, *Physical Review B* **38**, 9746 (1988)

[89] K. Thonke, T. Gruber, N. Teofilov, R. Schönfelder, A. Waag, R. Sauer, *Physica B: Condensed Matter* **308-310**, 945 (2001)

[90] M. A. Reshchikov, R. Y. Korotkov, *PHYSICAL REVIEW B* **64**, 115205 (2001)

[91] J. B. Cui, M. a. Thomas, *Journal of Applied Physics* **106**, 033518 (2009)

[92] J. M. Hvam, *Physica Status Solidi (B)* **63**, 511 (1974)

[93] J. Hvam, *Solid State Communications* **12**, 95 (1973)

[94] F.-Y. Jen, Y.-C. Lu, C.-Y. Chen, H.-C. Wang, C. C. Yang, B.-p. Zhang, Y. Segawa, *Applied Physics Letters* **87**, 072103 (2005)

[95] D. A. Melnick, *The Journal of Chemical Physics* **26**, 1136 (1957)

[96] W. An, X. Wu, X. Zeng, *Journal of Physical Chemistry C* **112**, 5747 (2008)

[97] P. Collins, K. Bradley, M. Ishigami, A. Zettl, *Science* **287**, 1801 (2000)

[98] R. S. Wagner, W. C. Ellis, *Transactions of the Metallurgical Society of AIME* **233**, 1053 (1965)

[99] M. Yazawa, M. Koguchi, A. Muto, M. Ozawa, K. Hiruma, *Applied Physics Letters* **61**, 2051 (1992)

[100] M. Yazawa, M. Koguchi, A. Muto, K. Hiruma, *Advanced Materials* **5**, 577 (1993)

[101] Y. Wu, P. Yang, *Journal of the American Chemical Society* **123**, 3165 (2001)

[102] M. H. Huang, Y. Wu, H. Feick, N. Tran, E. Weber, P. Yang, *Advanced Materials* **13**, 113 (2001)

[103] P. Yang, H. Yan, S. Mao, R. Russo, J. Johnson, R. Saykally, N. Morris, J. Pham, R. He, H.-J. Choi, *Advanced Functional Materials* **12**, 323 (2002)

[104] L. Vayssieres, *Advanced Materials* **15**, 464 (2003)

[105] S.-C. Liu, J.-J. Wu, *Materials Research Society Symposium Proceedings* **703**, 241 (2002)

[106] J. H. Choi, H. Tabata, T. Kawai, *Journal of Crystal Growth* **226**, 493 (2001)

[107] R. Liu, A. A. Vertegel, E. W. Bohannan, T. A. Sorenson, J. A. Switzer, *Chemistry of Materials* **13**, 508 (2001)

[108] G. Zhu, R. Yang, S. Wang, Z. L. Wang, *Nano letters* **10**, 3151 (2010)

[109] Y. Hu, C. Xu, Y. Zhang, L. Lin, R. L. Snyder, Z. L. Wang, *Advanced materials* **23**, 4068 (2011)

[110] Y. Hu, Y. Zhang, C. Xu, G. Zhu, Z. L. Wang, *Nano letters* 0–6 (2010)

[111] R. Rossetti, L. Brus, *The Journal of Physical Chemistry* **86**, 4470 (1982)

[112] A. J. Bard, *Science* **207**, 139 (1980)

[113] Y. M. Tricot, J. H. Fendler, *Journal of the American Chemical Society* **106**, 2475 (1984)

[114] A. Henglein, *Chemical Reviews* **89**, 1861 (1989)

[115] M. L. Steigerwald, L. E. Brus, *Accounts of Chemical Research* **23**, 183 (1990)

[116] X. Peng, L. Manna, W. Yang, J. Wickham, E. Scher, a. Kadavanich, A. Alivisatos, *Nature* **404**, 59 (2000)

[117] Z. A. Peng, X. Peng, *Journal of the American Chemical Society* **123**, 1389 (2001)

[118] D. Battaglia, X. Peng, *Nano Letters* **2**, 1027 (2002)

[119] W. W. Yu, Y. A. Wang, X. Peng, *Chemistry of Materials* **15**, 4300 (2003)

[120] K. J. Nordell, E. M. Boatman, G. C. Lisensky, *Journal of Chemical Education* **82**, 1697 (2005)

[121] J. J. Li, Y. A. Wang, W. Guo, J. C. Keay, T. D. Mishima, M. B. Johnson, X. Peng, *Journal of the American Chemical Society* **125**, 12567 (2003)

[122] J.-Y. Zhang, W. W. Yu, *Applied Physics Letters* **89**, 123108 (2006)

[123] L. S. Li, N. Pradhan, Y. Wang, X. Peng, *Nano Letters* **4**, 2261 (2004)

[124] W. W. Yu, J. C. Falkner, B. S. Shih, V. L. Colvin, *ChemInform* **35**, 3318 (2004)

[125] R. Gill, M. Zayats, I. Willner, *Angewandte Chemie (International ed. in English)* **47**, 7602 (2008)

[126] W. W. Yu, *Expert Opinion on biological therapy* **8**, 1571 (2008)

[127] I. L. Medintz, H. T. Uyeda, E. R. Goldman, H. Mattoussi, *Nature materials* **4**, 435 (2005)

[128] W. C. Chan, *Science* **281**, 2016 (1998)

[129] D. M. Willard, L. L. Carillo, J. Jung, A. Van Orden, *Nano Letters* **1**, 469 (2001)

[130] W. C. Chan, D. J. Maxwell, X. Gao, R. E. Bailey, M. Han, S. Nie, *Current Opinion in Biotechnology* **13**, 40 (2002)

[131] J. A. Kloepfer, S. E. Bradforth, J. L. Nadeau, *The journal of physical chemistry. B* **109**, 9996 (2005)

[132] R. Gill, I. Willner, I. Shweky, U. Banin, *The journal of physical chemistry. B* **109**, 23715 (2005)

[133] V. Stsiapura, A. Sukhanova, A. Baranov, M. Artemyev, O. Kulakovich, V. Oleinikov, M. Pluot, J. H. M. Cohen, I. Nabiev, *Nanotechnology* **17**, 581 (2006)

[134] W. R. Algar, U. J. Krull, *Chemphyschem : a European journal of chemical physics and physical chemistry* **8**, 561 (2007)

[135] D. V. Talapin, A. L. Rogach, I. Mekis, S. Haubold, A. Kornowski, M. Haase, H. Weller, *Colloids and Surfaces A* **202**, 145 (2002)

[136] T. Rajh, O. I. Micic, A. J. Nozik, *The Journal of Physical Chemistry* **97**, 11999 (1993)

[137] T. Vossmeyer, L. Katsikas, M. Giersig, I. Popovic, K. Diesner, A. Chemseddine, A. Eychmüller, H. Weller, *The Journal of Physical Chemistry* **98**, 7665 (1994)

[138] N. Gaponik, D. V. Talapin, A. L. Rogach, K. Hoppe, E. V. Shevchenko, A. Kornowski, A. Eychmüller, H. Weller, *The Journal of Physical Chemistry B* **106**, 7177 (2002)

[139] A. Rogach, T. Franzl, T. Klar, J. Feldmann, N. Gaponik, V. Lesnyak, A. Shavel, A. Eychmuller, Y. Rakovich, J. Donegan, *Journal of Physical Chemistry C* **111**, 14628 (2007)

[140] A. Rogach, S. V. Kershaw, M. Burt, M. T. Harrison, A. Kornowski, A. Eychmüller, H. Weller, *Advanced Materials* **11**, 552 (1999)

[141] A. Shavel, N. Gaponik, A. Eychmüller, *The Journal of Physical Chemistry B* **108**, 5905 (2004)

[142] V. Colvin, M. Schlamp, A. Alivisatos, *Nature* **370**, 354 (1994)

[143] C. Borchers, S. Müller, D. Stichtenoth, D. Schwen, C. Ronning, *The Journal of Physical Chemistry. B* **110**, 1656 (2006)

[144] C. Wongchoosuk, K. Subannajui, A. Menzel, I. A. Burshtein, S. Tamir, Y. Lifshitz, M. Zacharias, *The Journal of Physical Chemistry C* **115**, 757 (2011)

[145] W. W. Yu, L. Qu, W. Guo, X. Peng, *Chemistry of Materials* **15**, 2854 (2003)

[146] L. Qu, X. Peng, *Journal of the American Chemical Society* **124**, 2049 (2002)

[147] A. Rogach, *Semiconductor Nanocrystal Quantum Dots*, Springer, Wien (2008)

[148] L. Qu, X. Peng, *Journal of the American Chemical Society* **124**, 2049 (2002)

[149] V. LaBella, H. Yang, D. Bullock, P. Thibado, P. Kratzer, M. Scheffler, *Physical Review Letters* **83**, 2989 (1999)

[150] M. Nirmal, D. Norris, M. Kuno, M. Bawendi, A. Efros, M. Rosen, *Physical Review Letters* **75**, 3728 (1995)

[151] A. Efros, *Physical Review B* **46**, 7448 (1992)

[152] M. Nirmal, B. O. Dabbousi, M. G. Bawendi, J. J. Macklin, J. K. Trautman, T. D. Harris, L. E. Brus, *Nature* **383**, 802 (1996)

[153] J. MuÌĹller, J. M. Lupton, a. L. Rogach, J. Feldmann, D. V. Talapin, H. Weller, *Applied Physics Letters* **85**, 381 (2004)

[154] D. E. Gómez, J. van Embden, J. Jasieniak, T. a. Smith, P. Mulvaney, *Small* **2**, 204 (2006)

[155] C. Galland, Y. Ghosh, A. Steinbrück, M. Sykora, J. a. Hollingsworth, V. I. Klimov, H. Htoon, *Nature* **479**, 203 (2011)

[156] J. P. Hoogenboom, J. Hernando, E. M. H. P. van Dijk, N. F. van Hulst, M. F. García-Parajó, *Chemphyschem : a European journal of chemical physics and physical chemistry* **8**, 823 (2007)

[157] D. A. Bout, *Science* **277**, 1074 (1997)

[158] P. Frantsuzov, M. Kuno, B. Jankó, R. A. Marcus, *Nature Physics* **4**, 519 (2008)

[159] T. Krauss, L. Brus, *Physical Review Letters* **83**, 4840 (1999)

[160] J. Aldana, Y. a. Wang, X. Peng, *Journal of the American Chemical Society* **123**, 8844 (2001)

[161] B. J. Coppa, C. C. Fulton., P. J. Hartlieb, R. F. Davis, B. J. Rodriguez, R. J. Nemanich, B. J. Shields, *Journal of Applied Physics* **95**, 5856 (2004)

[162] J. Jasieniak, J. Pacifico, R. Signorini, a. Chiasera, M. Ferrari, a. Martucci, P. Mulvaney, *Advanced Functional Materials* **17**, 1654 (2007)

[163] Y. Xu, M. Schoonen, *American Mineralogist* **85**, 543 (2000)

[164] D. C. Reynolds, D. C. Look, B. Jogai, C. W. Litton, G. Cantwell, W. C. Harsch, *PHYSICAL REVIEW B* **60**, 2340 (1999)

[165] K. Keem, H. Kim, G.-T. Kim, J. S. Lee, B. Min, K. Cho, M.-Y. Sung, S. Kim, *Applied Physics Letters* **84**, 4376 (2004)

[166] J. Bao, I. Shalish, Z. Su, R. Gurwitz, F. Capasso, X. Wang, Z. Ren, *Nanoscale research letters* **6**, 404 (2011)

[167] J. Nayak, J. Kasuya, a. Watanabe, S. Nozaki, *Journal of Physics: Condensed Matter* **20**, 195222 (2008)

[168] Y. J. Zeng, M. Menghini, D. Y. Li, S. S. Lin, Z. Z. Ye, J. Hadermann, T. Moorkens, J. W. Seo, J.-P. Locquet, C. Van Haesendonck, *Physical Chemistry Chemical Physics* **13**, 6931 (2011)

[169] A. Chandra, C. E. Wood, D. W. Woodard, L. F. Eastman, *Solid-State Electronics* **22**, 645 (1979)

[170] K. Vanheusden, W. L. Warren, C. H. Seager, D. R. Tallant, J. a. Voigt, B. E. Gnade, *Journal of Applied Physics* **79**, 7983 (1996)

[171] D. Crisler, J. Cupal, A. Moore, *Proceedings of the IEEE* **56**, 225 (1968)

[172] S. Lany, A. Zunger, *Physical Review Letters* **98**, 045501 (2007)

[173] K. Jacobi, G. Zwicker, A. Gutmann, *Surface Science* **141**, 109 (1984)

[174] J. D. Prades, F. Hernandez-Ramirez, R. Jimenez-Diaz, M. Manzanares, T. Andreu, a. Cirera, a. Romano-Rodriguez, J. R. Morante, *Nanotechnology* **19**, 465501 (2008)

[175] Q. H. Li, T. Gao, Y. G. Wang, T. H. Wang, *Applied Physics Letters* **86**, 123117 (2005)

[176] V. Klimov, D. McBranch, *Physical Review Letters* **80**, 4028 (1998)

[177] T.-W. Zeng, I.-S. Liu, K.-T. Huang, H.-C. Liao, C.-T. Chien, D. K.-P. Wong, C.-W. Chen, J.-J. Wu, Y.-F. Chen, W.-F. Su, *Journal of colloid and interface science* **358**, 323 (2011)

[178] H.-M. Cheng, K.-Y. Huang, K.-M. Lee, P. Yu, S.-C. Lin, J.-H. Huang, C.-G. Wu, J. Tang, *Physical Chemistry Chemical Physics* (2012)

[179] A. Andersson, N. Johansson, P. Bröms, N. Yu, D. Lupo, W. R. Salaneck, *Advanced Materials* **10**, 859 (1998)

[180] M. G. Helander, M. T. Greiner, Z. B. Wang, W. M. Tang, Z. H. Lu, *Journal of Vacuum Science & Technology A* **29**, 011019 (2011)

[181] J. Zhou, Y. Gu, Y. Hu, W. Mai, P.-H. Yeh, G. Bao, A. K. Sood, D. L. Polla, Z. L. Wang, *Applied physics letters* **94**, 191103 (2009)

[182] C. Soci, A. Zhang, B. Xiang, S. a. Dayeh, D. P. R. Aplin, J. Park, X. Y. Bao, Y. H. Lo, D. Wang, *Nano Letters* **7**, 1003 (2007)

[183] Y. W. Heo, L. C. Tien, D. P. Norton, S. J. Pearton, B. S. Kang, F. Ren, J. R. LaRoche, *Applied Physics Letters* **85**, 3107 (2004)

[184] A. Inumpudi, A. Iliadis, S. Krishnamoorthy, S. Choopun, R. Vispute, T. Venkatesan, *Solid-State Electronics* **46**, 1665 (2002)

[185] a.a Iliadis, R. Vispute, T. Venkatesan, K. Jones, *Thin Solid Films* **420-421**, 478 (2002)

[186] L. E. Halliburton, N. C. Giles, N. Y. Garces, M. Luo, C. Xu, L. Bai, L. a. Boatner, *Applied Physics Letters* **87**, 172108 (2005)

[187] S. Kurbanov, K. Igamberdiev, S. Yuldashev, T. W. Kang, *Japanese Journal of Applied Physics* **48**, 115004 (2009)

[188] K. Hümmer, *Physica Status Solidi (b)* **56**, 249 (1973)

[189] D. Reynolds, C. Litton, T. Collins, *Physical Review* **140**, A1726 (1965)

[190] B. Meyer, J. Sann, S. Lautenschläger, M. Wagner, A. Hoffmann, *Physical Review B* **76**, 184120 (2007)

[191] H. Fröhlich, *Advances in Physics* **3**, 325 (1954)

[192] Y. Varshni, *Physica* **34**, 149 (1967)

[193] R. Dingle, *Physical Review Letters* **23**, 579 (1969)

[194] B. Kimpel, H.-J. Schulz, *Physical Review B* **43**, 9938 (1991)

[195] P. Dahan, V. Fleurov, P. Thurian, R. Heitz, A. Hoffmann, I. Broser, *Journal of Physics: Condensed Matter* **10**, 2007 (1998)

[196] W. Grieshaber, E. F. Schubert, I. D. Goepfert, R. F. Karlicek, M. J. Schurman, C. Tran, *Journal of Applied Physics* **80**, 4615 (1996)

[197] J. F. Muth, R. M. Kolbas, a. K. Sharma, S. Oktyabrsky, J. Narayan, *Journal of Applied Physics* **85**, 7884 (1999)

[198] P.-c. Chang, Z. Fan, D. Wang, W.-y. Tseng, W.-a. Chiou, J. Hong, J. G. Lu 5133–5137 (2004)

[199] Q. H. Li, Y. X. Liang, Q. Wan, T. H. Wang, *Applied Physics Letters* **85**, 6389 (2004)

[200] I. Mora-SeroÌĄ, F. Fabregat-Santiago, B. Denier, J. Bisquert, R. Tena-Zaera, J. Elias, C. LeÌĄvy-CleÌĄment, *Applied Physics Letters* **89**, 203117 (2006)

[201] S. Lettieri, L. Santamaria Amato, P. Maddalena, E. Comini, C. Baratto, S. Todros, *Nanotechnology* **20**, 175706 (2009)

[202] B. P. Zhang, N. T. Binh, K. Wakatsuki, Y. Segawa, Y. Kashiwaba, K. Haga, *Nanotechnology* **15**, S382 (2004)

[203] H. Priller, J. Brückner, T. Gruber, C. Klingshirn, H. Kalt, a. Waag, H. J. Ko, T. Yao, *Physica Status Solidi (b)* **241**, 587 (2004)

Publications and Conference Contributions

Journal Publications

1. Oxygen-Controlled Photoconductivity in ZnO Nanowires Functionalized with Colloidal CdSe Quantum Dots
   D. Hou, A. Dev,K. Frank, A. Rosenauer, and T. Voss
   The Journal of Physical Chemistry C (in press)

Contributions to Conferences and Workshops

(with publications)

1. Photoconductivity of ZnO Nanowires Decorated with CdSe Quantum Dots
   D. Hou, A. Dev,K. Frank, A. Rosenauer, and T. Voss
   MRS Proceedings, 1408, mrsf11-1408-bb10-20, doi: 10.1557/opl.2012.35
   2011 MRS Fall Meeting, Boston (USA)

(without publications)

1. Deep-level emission in ZnO bulk crystals and nanowires: intensity-dependent recombination dynamics versus indicator for crystalline quality
   T. Voss, D. Hou, A. Menzel, C. Ronning, and M. Zacharias
   MRS fall meeting 2012, Boston (USA)

2. Oxygen-controlled electron-transfer dynamics under optical excitation in hybrid ZnO-nanowire/CdSe-quantum dot structures
   D. Hou, A. Dev, J. Gutowski, and T. Voss
   31st International Conference on the Physics of Semiconductors ICPS 2012, Zurich (Switzerland)

3. Oxygen-controlled electron-transfer dynamics under optical excitation in hybrid ZnO-nanowire/CdSe-quantum dot structures
   D. Hou, A. Dev, J. Gutowski, and T. Voss
   InternationalWorkshop on ZnO and Related Materials 2012, Nice (France)

4. Deep-level emission in ZnO nanowires: intensity-dependent recombination dynamics versus indicator for crystalline quality
   T. Voss, D. Hou, A. Menzel, C. Ronning, and M. Zacharias
   InternationalWorkshop on ZnO and Related Materials 2012, Nice (France)

5. Oxygen-controlled photoconductivity in hybrid ZnO-nanowire/CdSe-quantum-dot devices
   D. Hou, A. Dev, and T. Voss
   4th International Conference on One-dimensional Nanomaterials (ICON 2011), Beijing (China)

6. Oxygen-controlled photoconductivity in hybrid ZnO-nanowire/CdSe-quantum-dot devices
   D. Hou, A. Dev, J. Gutowski, and T. Voss
   1st EOS Topical Meeting on Micro- and Nano-Optoelectronic Systems 2011,
   Bremen (Germany)

7. Oxygen-controlled photoconductivity in hybrid ZnO-nanowire/CdSe-quantum-dot devices
   D. Hou, A . Dev, and T. Voss
   Spring Meeting of the German Physical Society, Berlin (2012)

8. Optical properties of ZnO-nanowire/CdSe-colloidal-quantum-dot hybrid structures
   D. Hou, J.-P. Richters, A. Dev, and T. Voss
   Spring Meeting of the German Physical Society, Dresden (2011)

9. Dynamics of the deep-level emission in ZnO nanowires
   D. Hou, I. Rückmann, and T. Voss
   Spring Meeting of the German Physical Society, Regensburg (2010)

10. Experimental and numerical analysis of the waveguiding properties of ZnO nanowires
    D. Hou, J.-P. Richters, and T. Voss
    Spring Meeting of the German Physical Society, Dresden (2009)

Acknowledgments

My deepest thanks go to Prof. Dr. Jürgen Gutowski for giving me the opportunity to work in his research group. I sincerely thank his guidance in my study, and his precious discussions and suggestions for this work.

My grateful and sincere thanks also go to PD Dr. Tobias Voss for his supervision and patient guidance throughout years. I especially appreciate his encouragement and continuous support. Every details of this work includes his effort and energy.

I am also very grateful to Prof. Dr. Andreas Rosenauer for agreeing to co-evacuate this dissertation. The valuable cooperation with his research group constitutes an important part of this work.

I would also like to thank Prof. Dr. Ilja Rückmann for his fruitful discussions and valuable suggestions on the work of ZnO.

This work would not have been possible without the assistance from our co-operation partners. I am thankful to Kristian Frank in the group of Prof. Dr. Andreas Rosenauer for his assistance in TEM characterization of the samples. Thank Stephanie Bley for her help in the plasma cleaning. I express my gratitude to Prof. Dr. Marcus Bäumer and Prof. Dr. Dieter Wöhrle from the Faculty of Chemistry, Universität Bremen for their valuable discussion and kind assistance in the surface treatment of ZnO and the synthesis of semiconductor quantum dots. Thank Dr. Volkmar Zielasek, Darius Arndt, and Lena Altmann in the group of Prof. Marcus Bäumer for their assistance in plasma treatment of ZnO and quantum dot purification. I am also very grateful to Prof. Dr. Monika Fritz from the Institute for Biophysics for the help in quantum dot centrifugation. I equally thank Prof. Dr. Carsten Ronning from Universität Jena and Prof. Dr. Margit Zacharias from Universität Freiburg for providing the ZnO samples. Thank Sebastian Geburt in the group of Prof. Dr. Carsten Ronning for the valuable discussions about the defects in ZnO and providing chemicals for quantum dot synthesis. I am also thankful to Andreas Menzel in the group of Prof. Dr. Margit Zacharias for the growth of nanowires and explaining the growth mechanisms.

I acknowledge my colleague Dr. Apurba Dev, Dr. Jan-Peter Richters, Dr. Abdelhamid Elshaer, Moritz Seyfried and Dr. Kathrin Sebald for their assistance in my experiments and their valuable discussions. I learnt a lot from them. Further thanks go to Dr. Kathrin Sebald and Moritz Seyfried for their careful reviewing of this dissertation. I thank Mr. Gerd Ankele for his assistance to solve various technical problems in my experiments. I am also very grateful to Ms. Annegret Ebert for her patient help in dealing with numerous documents and picking me up at my first arrival in Bremen. I give my gratitude to all the present and former group members for the friendly and lovely working atmosphere they make.

I am grateful to China Scholarship Council (CSC) for providing a financial support for my studying in Bremen.

With my deep love I thank my wife for her unwavering love and support in these years. Her love is the source of my strength and power. Thank the city Bremen where we met, knew each other, and fell in love.

My love to my parents and big sisters for accompaniment with me with their love throughout my life. Their love and support is the bedrock of my spirit. Thank my friends for their encouragement and sharing with me the happiness and sadness. At last I express my very sincere thanks to all those who have helped me and contributed to this work. Thank all of you.

Curriculum Vitae

Date of Birth:	08.03.1984
Place of Birth:	Heze, China

Education:

09/1990–07/1995	Primary School: Houzai, Heze, China
09/1995–07/1998	Junior Middle School: Sunmiao Middle School, Heze, China
09/1998–07/2001	Senior Middle School: Chengwu Central Middle School, Heze, China
09/2001–07/2005	Shandong University, Jinan, China Degree: B.Sc. in Physics Thesis: Simulation of Au atom attachment on semiconductor surface and its effect on the electronic properties
09/2005–07/2008	Shandong University, Jinan, China Degree: M.Sc. in Physics Thesis: Investigation of Electro-Optic Properties and Lattice Damage Distribution of Ion Implanted Waveguides in Lithium Niobate Supervisor: Prof. Keming Wang
09/2008–present	University of Bremen, Bremen, Germany PhD student in the group of Prof. Dr. Jürgen Gutowski Supervised by PD Dr. Tobias Voss